A study of industrial steel making dusts: melting behaviour and interactions with refractory bricks

Diederik van Roemburg

School of Chemical Engineering

Thesis submitted for examination for the degree of Master of Science in Technology.

Espoo 31.7.2020

Supervisor

Prof. Ari Jokilaakso

Advisors

D.Sc. (Tech.) Marko Kekkonen

D.Sc. (Tech.) Mari Lindgren

Aalto University
School of Chemical Engineering

Aalto University
School of Chemical
Engineering

Aalto University, P.O. BOX 11000, 00076 AALTO
www.aalto.fi
Abstract of the master's thesis

Author Diederik van Roemburg

Title A study of industrial steel making dusts:
melting behaviour and interactions with refractory bricks

Degree programme Chemical Biochemical and Materials Engineering

Major Sustainable Metals Processing **Code of major** CHEM3026

Supervisor Prof. Ari Jokilaakso

Advisors D.Sc. (Tech.) Marko Kekkonen, D.Sc. (Tech.) Mari Lindgren

Date 31.7.2020 **Number of pages** 129 **Language** English

Abstract

Understanding the behaviour of alkali metals and halogens at high temperatures combined with their effect on refractories is important for efficient and safe operating of Electric Arc Furnaces (EAF). In this work the behaviour of alkali metals and halogens in industrial EAF dusts was investigated at temperatures between 800 °C and 1400 °C. The dusts were first heated for 1, 2, 4 and 8 hours at 800 °C and 1200 °C under a reducing atmosphere of 90% CO/10% CO_2 to determine the effect of the heating time. The dusts were then heated for 2 hours at 1200 °C, 1250 °C and 1300 °C under the same reducing atmosphere.

Analyses of the industrial dusts were performed using a combination of SEM-EDS and image analyses software on BSE pictures. The analyses were performed to better understand the melting behaviour of the dusts and the behaviour of fluorine, chlorine, sodium and potassium. It was found that melting in the EAF dusts starts in the temperature region of 1250-1300 °C. Depending on the composition of the dust, then a molten fraction of 25-50 % forms. The AOD dust had a molten fraction at 1200 °C of about 30 %. Due to the industrial nature, the concentrations of the investigated elements were low in the raw material and thus also in the samples. Fluorine was found in high levels in the melted phase of the AOD dust. In the EAF dusts fluorine was found in a solid spinel phase. Sodium was mostly found in the slag phase in low concentrations. Potassium was only found in the slag phase of one EAF dust and some spots of the other EAF dusts slag phase. Chlorine was not present in the samples after heating.

The interaction between the dusts and refractories was investigated by conducting a study where the effects of a synthetic dust on four types of refractories at 1300 °C under the same reducing atmosphere were analysed. The synthetic dust contained high concentrations of potassium, fluorine and chlorine. The refractory samples were Radex OX6 (Cr-MgO), Radex S (MgO), Resistal RK30 (Al-Cr) and Durital E90 (Al-Si). The refractory samples were analysed using a combination of visual analyses and SEM-EDS.

From the four refractories tested with the highly concentrated synthetic dust, it was found that the two refractories containing no chrome were severely penetrated by potassium. The two chrome containing refractories were only affected to a depth of 5 mm. The Durital E90 refractory was the most affected in its shape where the others suffered less from expansion.

Keywords Corrosion, Alkali metal, Halogen, Image analysis software, BSE, AOD, zinc, refractory wear

Acknowledgements

This thesis was carried out as part of the SYMMET project and conducted in cooperation with the Outotec Research Center (ORC). The work was conducted at the Department of Chemical and Metallurgical Engineering between 7.1-19.7.2020.

I would like to start by thanking ORC for financing this thesis and providing me with the industrial raw materials necessary to conduct my experiments. I want to express my sincerest appreciation to Professor Ari Jokilaakso for letting me do this thesis and for his guidance and support while working on it. Then I would also like to express my gratitude to my advisor D.Sc.(Tech.) Marko Kekkonen for the countless hours of helping me with practical work and giving feedback on my monthly presentations and my thesis report. Further, I would like to thank D.Sc. Pekka Taskinen for using his experience and knowledge to help shape my thesis and his suggestions for how to continue when I was stuck. Then I would like to thank D.Sc. (Tech) Mari Lindgren, D.Sc. (Tech) Jouni Pihlasalo and D.Sc. (Tech) Tuija Suorti for their input and feedback during the monthly meetings. I would like to recognize the invaluable assistance that M.Sc. Lassi Klemettinen provided during my thesis with amongst others; taking care of the furnace so that I had a working furnace whenever possible, teaching me how to safely conduct my experiments and the countless hours that you spend at the SEM-EDS for me to analyze my samples.

Lastly, I want to express my gratitude to my friends and family, especially Anna Levering and Stephen Nicholas Swatman, for their support and input during my thesis.

Otaniemi, 31.7.2020

van Roemburg D. S. BSc

Contents

Abstract 3

Acknowledgements 5

Contents 6

Abbreviations 8

1 Introduction 9

2 Literature review 11
2.1 Types of refractories . . . 11
2.2 Refractory wear . . . 12
2.2.1 Chemical attack . . . 13
2.2.2 Mechanical attack . . . 13
2.3 Refractory corrosion by solid and liquid phase compounds . . . 14
2.3.1 Sodium and potassium . . . 14
2.3.2 Fluorine . . . 14
2.3.3 Zinc . . . 21
2.3.4 Corrosion by other solid or liquid means . . . 24
2.4 Refractory corrosion by gas phase compounds . . . 29
2.4.1 Sodium and potassium . . . 29
2.4.2 Fluorine and chlorine . . . 34
2.4.3 Zinc . . . 35
2.4.4 Other gases . . . 35

3 Materials and experimental methods 40
3.1 Material and sample preparation . . . 40
3.2 Equipment . . . 40
3.3 Experimental procedure . . . 43
3.4 Sample characterization . . . 43
3.4.1 Sample preparation . . . 43
3.4.2 SEM-EDS analysis and image analysis . . . 45

4 Results and discussion 47
4.1 Melting behaviour . . . 47
4.1.1 800 °C to 1200 °C region . . . 47
4.1.2 1200 °C to 1400 °C region . . . 47
4.1.3 Image analysis . . . 55
4.2 Alkali and halogen behaviour . . . 58
4.2.1 Fluorine . . . 58
4.2.2 Sodium . . . 59
4.2.3 Potassium . . . 59
4.2.4 Chlorine . . . 59

4.3 Refractory - Dust interaction 59
4.3.1 Dust fractions 59
4.4 Effects on the refractory composition and structure 61
4.4.1 Visual analyses 61
4.4.2 BSE and EDS analyses 61

5 Summary and Conclusions **77**

6 For future work **78**

A Selected analysis points from Radex OX6 **84**

B Selected analysis points from Resistal RK30 **95**

C Selected analysis points from Radex S **108**

D Selected analysis points from Durital E90 **120**

Abbreviations

EAF	Electric Arc Furnace
AOD	Argon Oxygen Decarburization
EAFD	Electric Arc Furnace Dust
EWC	European Waste Catalogue
ORC	Outotec Research Centre
BSE	Back Scattered Electron
XRD	X-Ray Diffraction
AIA	Automatic Image Analysis
SEM	Scanning Electron Microscope
SEM-EDX/SEM-EDS	Scanning Electron Microscope - Energy Dispersive X-ray

1 Introduction

The use of electric arc furnaces (EAF) and argon oxygen decarburization (AOD) converters is common practice in stainless steelmaking. Approximately 1-2% of the charge fed to an EAF is lost as electric arc furnace dust (EAFD), which is often dumped in a landfill. (Kekki, Aromaa, and Forsen 2012) It was estimated in 2006 that EAFs produced 3.7 million tonnes of EAFD annually, and plants in Europe generated between 500,000 and 900,000 tonnes of dust per year. (Machado et al. 2006) The world EAFD production had increased to 7.1 million tonnes per year in 2010 and is expected to further increase with increasing EAF-based steel production and recycling. (Suetens et al. 2014) EAFD is categorized as hazardous waste according to the European Waste Catalogue (EWC 2002), and disposal of it is therefore a costly endeavour. (Oustadakis et al. 2010) From an economic and environmental point of view, recycling of the dust is desirable. In Europe in 1996, approximately 45% of the EAFD was recycled, though the amount widely differs between European countries. (Domínguez et al. 2010) It was estimated by a survey that the European recycling rate of EAFD had increased to 66% in 2006. (Remus et al. 2013) In 2011, 45% of the global amount of EAFD was being recycled. North America and Europe account for approximately 75% of global dust recycling. (Wegscheider et al. 2015)

The increasing demand for EAFD recycling stems from the presence of various valuable and harmful elements found in the dust. It is important from a circular economy point of view to recycle the valuable components. Some examples of valuable components are (15-30 wt%) iron and (2-30 wt%) zinc. The zinc content depends strongly on the amount of recycled galvanised steel. (Simonyan, Alpatova, and Demidova 2019; Oustadakis et al. 2010) Further valuable components are alloying elements used in stainless steelmaking. These elements are (2-3 wt%) manganese, (2-8 wt%) chrome and (1-2 wt%) nickel. Further, harmful elements should not be released into the environment. Some of the harmful components found in the EAFD are sodium (1 wt%), potassium (1 wt%), chlorine (0,5-2 wt%) and fluorine (0,5 wt%). (Kashiwaya et al. 2004; Buzin, Heck, and Vilela 2017)

Direct recycling of EAFD to steel production for the recovery of the valuable content is hindered when the dust has high zinc content. This is because zinc causes operational difficulties in the steel making process. (Omran and Fabritius 2017) Direct recycling is further hampered by the alkali metals and halogens contained in the dust. Those elements have a deteriorating effect on the refractory materials.

Refractories are used in many high temperature applications such as kilns, furnaces, incinerators and reactors. Kilns and furnaces are used in metal production, incinerators in (hazardous) waste incineration and refractory lined reactors in petrochemical industrial processes. In waste incineration the main corrosive component depends on the type of waste, common investigated components are chlorine and fluorine.

In pyrometallurgical processes, the performance of refractory materials is critical in regards to production costs, product quality and safety. Halting production operations for maintenance is a costly endeavour and causes the operator to lose production value. Corrosion of refractory materials can also cause defects in the

product or lower the product quality by contaminating the product with unwanted materials. Finally, refractory bricks keep the hot toxic and corrosive atmosphere and liquid metal inside. Unknown degradation mechanisms may compromise the structural integrity of the equipment and endanger the operators.

The remainder of this thesis is structured as follows. In chapter 2, existing knowledge and previous work regarding refractory degradation and corrosion will be reviewed. In chapter 3 the methods and materials used in this work will be described. In chapter 4 current knowledge is supplemented by experimental research, in which the melting behaviour of EAF- and AOD-dust and the behaviour of alkali metals and halogens within the dust is studied. This can help with understanding how these materials will react when handled in the recycling process for these dusts. Further studies were performed to study the interaction between dusts and refractories. This will help with understanding how the refractories get affected by these dusts.

2 Literature review

2.1 Types of refractories

Chemical attack on refractories can be divided in a broad sense into acidic and basic attack (see Chapter 2.2.1 on chemical attack). Hence there are also two general types or refractories, basic refractories and acidic refractories. These refractories are then compatible, or more compatible, with the type of attack being carried out on them, thus acidic refractories are compatible with acidic slags. Compatible means that the refractory and slag coexist next to each other on a microscopic scale at the operating temperature; with less compatible refractories the two phases do not coexist, but the reaction is usually slow. (Brosnan 2004)

Refractories can also be classified based on their chemical composition into the following categories:

- Silica refractories, produced from quartz or fused silica, are extensively used in iron and steel industry. Important properties of silica refractories are the high fusion point, refractoriness and resistance to thermal shock. (Bhatia 2012; Satyendra 2020)
- Fireclay refractories consist of 18-44% alumina and 50-80% silica, creating different classes for different duties. Fireclay refractories are the least expensive refractory and, therefore, commonly used refractories. Fireclay refractories are commonly used in the iron and steel industry. The softening point of fireclay brick is far below its fusion temperature, therefore these refractories tend to deform under load. (Bhatia 2012; Satyendra 2020)
- Alumina refractories, consisting of at least 50% alumina, are also divided into different classes based on the alumina content like in fireclay refractories. Common uses for alumina refractories are in crucibles, the heart and shaft of blast furnaces and kilns. Alumina is chemically stable making it resistant to corrosion, and it has high hardness and spalling resistance. (Bhatia 2012; Satyendra 2020)
- Magnesia refractories, of which the main constituent is magnesia, are produced from brines and magnesite. Magnesia refractories are highly resistant to basic slags and therefore commonly used in basic steelmaking. (Bhatia 2012; Satyendra 2020)
- Doloma refractories, produced from dolomite which is a carbonate consisting of magnesia and calcia. Commonly used in cement kilns for its coating stability and resistance to thermal shock and alkali attack. (Bhatia 2012; Satyendra 2020)
- Magnesia-chrome or chrome-magnesia refractories, consisting of magnesia and chromia. Chrome-magnesia refractories contain 15-35% chromia with 42-50% magnesia and magnesia-chrome refractories contain at least 60% magnesia and

8-18% chromia. Chrome-magnesia refractories are used in critical high temperature parts of furances and have high corrosion resistance and refractoriness. Magnesia-chrome refractories have high basic resistance and thermal stability. (Bhatia 2012; Satyendra 2020)

- Silicon carbide refractories are produced from the reaction between silica and carbon. Silicon carbide refractories are used in the protective muffle of certain ceramic kilns, where the goal is to protect the ceramics from the combustion gases. Silicon carbide is used for its high heat conductivity. (Bhatia 2012; Satyendra 2020)

- Zirconia refractories mainly consist of zirconia. Zirconia refractories are used in casting nozzles and gates and crucibles. Low thermal conductivity makes zirconia an insulating refractory. (Bhatia 2012; Satyendra 2020)

- Carbon refractories are produced from different types of manufactored carbon. Carbon refractories can be used under strong reducing environments, these refractories have high refractoriness, high thermal stability and resistance to slag action. (Bhatia 2012; Satyendra 2020)

Refractories can also be classified based on the type of bonding. There are three ways of bonding a refractory, chemically bonded, fused cast and direct bonded. Chemically bonded refractories are comprised of two or more different components: The main constituent of the refractory and a second component that chemically reacts with the main constituent. The reaction of these two components then usually produces an amorphous phase, which leads to hardening and loss of workability of the refractory. (Luz et al. 2018)

In the case of fused cast refractories, the main constituent of the refractory is melted, for example in an electric arc furnace, and then poured into a cast. Upon cooling of the molten refractory material ceramic bonds are formed within the material, hardening it to the shape of the cast. (Selkregg 2018)

In direct bonded refractories highly pure grains of the components are mixed into a binder and mixed to obtain a homogeneous mixture. This mixture is then heated to high temperatures, causing spinels to form from the constituents of the grains and the binder. The spinels keep the raw materials together. (Sarkar 2019)

2.2 Refractory wear

Refractory materials are ceramic materials. General properties of which are a high melting point, low thermal and electrical conductivity, low thermal expansion and high hardness. The structure of refractory materials contrasts with the structure of other ceramic materials in that it is not a homogeneous system, but rather a heterogeneous multi-component system of coarse particles bonded by a glassy phase or interlocking crystalline phase. (Callister and Rethwisch 2013; DeLucia and Wolfe 2000) The function of the refractory material is to serve as a thermal insulator and retain its shape and chemical integrity. Refractory materials satisfy these requirements due to their low thermal conduction and high melting point. (Callister and Rethwisch 2013)

During their service life refractories are exposed to a multitude of wear mechanisms. Different types of chemical and mechanical wear mechanisms will be discussed below.

2.2.1 Chemical attack

The first wear mechanism is wear by chemical attack, this is defined by C. Schacht in the Refractories Handbook as: "Corrosion of refractories is refractory wear by loss of thickness and mass from the exposed face of the refractory as a consequence of chemical attack by a corroding fluid in a process in which the refractory and the corroding fluid react, approaching chemical equilibrium in the zone of contact between the refractory and the fluid." (Brosnan 2004)

During operation the refractory material can be in contact with molten metal, molten slag and fumes. These liquid and gas phase substances can react with the refractory materials. These reactions can occur on the surface of the refractory bricks, and also inside of the pores of the refractory brick when they are penetrated by the liquid or gas phase. The reactions with refractories mainly consist of acidic or basic attack and formation of new minerals. (Scudeller, Longo, and Varela 1990; DeLucia and Wolfe 2000; Ko 1991)

In acidic or basic attack the acidic or basic components in the slag react with the refractory. Basic components are magnesia, calcia, ferrous oxide and alkalis. The main acidic component is silica. The slag reacts mostly with the bonding phase and on grain boundaries, dissolving the bonding phase or components thereof. Dissolution of the bonding phase can result in the refractory aggregates being carried into the slag or the weakening of the brick for mechanical interactions. (Ko 1991; Benson, Sondreal, and Hurley 1995) Formation of new minerals happens mostly by gas phase interactions with alkalis and halides. This can have two distinct effects; the formation of minerals larger than the original mineral and the formation of substances with a lower melting point. The volumetric expansion caused by formation of larger minerals can result in crack formation in the refractory brick. (Scudeller, Longo, and Varela 1990) Formation of lower melting point phases can cause the refractory to become machanically unstable at its normal operating temperature. An example of the formation of a lower melting point phase is magnesium fluoride with a melting point of 1263 °C from magnesia and fluorine, where magnesia has a melting point of 2852 °C. (DeLucia and Wolfe 2000)

2.2.2 Mechanical attack

The refractory bricks suffer from different mechanical interactions due to chemical interactions and temperature variations. Differing thermal expansion coefficients for the different parts of the refractory brick can cause crack formation if there is a large temperature change within the brick. Further mechanical stress on the refractory brick is caused by the hard material entering the furnace scraping past the refractory brick (erosion). In rotating furnaces the bending moment between the support beams can also cause stress on the refractory. (Kazanbaev et al. 2004) Finally, there is spalling, which can be caused by previously mentioned thermal expansion, mechanical stress and chemical expansion or densification (loss of porosity). Here

parts of the refractory spall of from the rest of the brick. (Ko 1991; Yazhenskikh, Hack, and Müller 2006) An example of spalling can been found in rotary kilns for hazardous waste incineration. Here, partially molten inorganic ash infiltrates the refractories on the hot face creating a densified layer with a different thermal expansion coefficient than the non infiltrated refractory. Together with thermal cycles this thermal expansion coefficient difference is responsible for crack formation and eventually spalling. (Owens 1991)

2.3 Refractory corrosion by solid and liquid phase compounds

2.3.1 Sodium and potassium

The degradation of bauxite-based and chamotte-based refractory materials were tested in a laboratory scale study by J. Stjernberg et al. (2013). In this study the refractories were brought into contact with sodium and potassium by placing sodium and potassium doped deposits in mounts on the refractory material. The result of these experiments can be seen in the Figures below.

Figure 1 shows the result of the chamotte based refractory with a mound of sodium doped deposit and a mound of potassium doped deposit after the reaction test. Here it can be seen that the sodium doped deposit had a higher concentration of liquid phase. In Figure 2, the diffractogram from the bauxite-based brick can be seen. It was determined that sodium reacts with the refractory material to form a liquid phase, which is not the case with potassium deposits. In this study it was found that bauxite- and chamotte- based refractory bricks are more sensitive to corrosion by sodium than by potassium. (J. Stjernberg et al. 2013)

Chrome bearing refractories are sensitive to the oxidation of Cr(III) to Cr(VI) by alkali and alkaline earth metals at high temperatures. (Hu, Z. Xu, et al. 2015; Hu, Luo, et al. 2013; J. Chen, Jiao, et al. 2013; Mao, Gao, et al. 2016; Verbinnen et al. 2013) However, silica and alumina can inhibit the formation of Cr(VI) because of their acidity. Furthermore, chrome oxidation is less prevalent in reducing conditions than in oxidising conditions. (Y. Xu et al. 2019; Mao, Deng, et al. 2016; Wu et al. 2018)

2.3.2 Fluorine

Park et al. (2010) conducted experiments to reveal details on the interaction between fluoride containing metallurgical slags and zirconia, doloma or magnesia refractories. The effect of fluorspar (CaF_2) on the dissolution of zirconia was studied by varying the fluorspar content from 7 to 19 wt%. The slag phase consisted of a CaO-SiO_2-MgO liquid system with a wt% CaO / wt% SiO_2 ratio of 1.4. The interface resulting from these experiments with a fluorspar concentration of 7, 13 and 19 wt% can be seen in Figure 3. $CaZrO_3$ (CZ) formed as a stable compound at the interface between the slag and refractory, this is depicted as region 1 in the Figure. In region 2 Ca_2SiO_4, (C2S)-ZrO_2 and (Z)-CZ can be found. Region 3 consists of the liquid slag phase mixed with dissolved zirconium and C2S-Z.

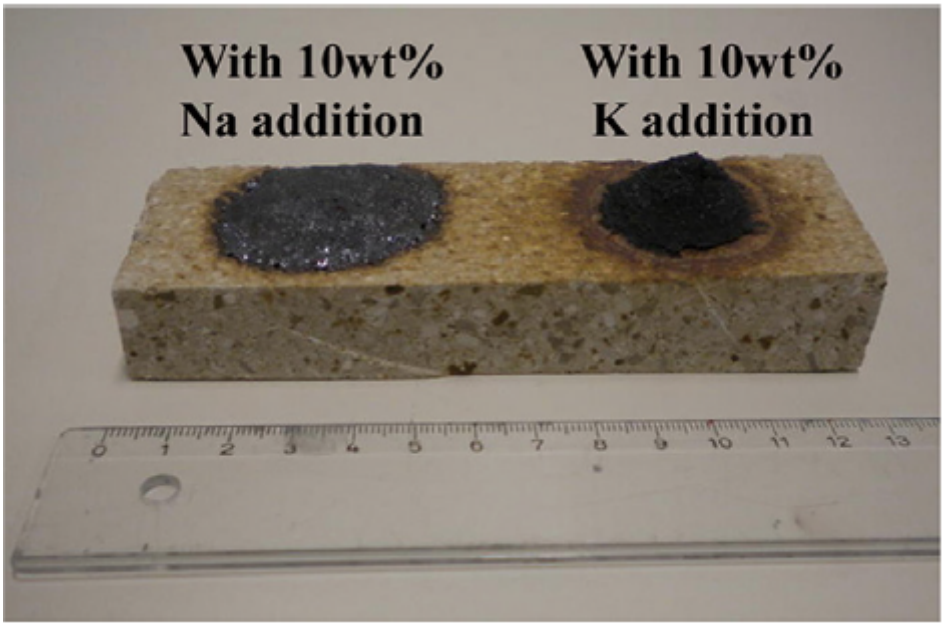

Figure 1: Chamotte-based refractory brick after reaction test. (J. Stjernberg et al. 2013)

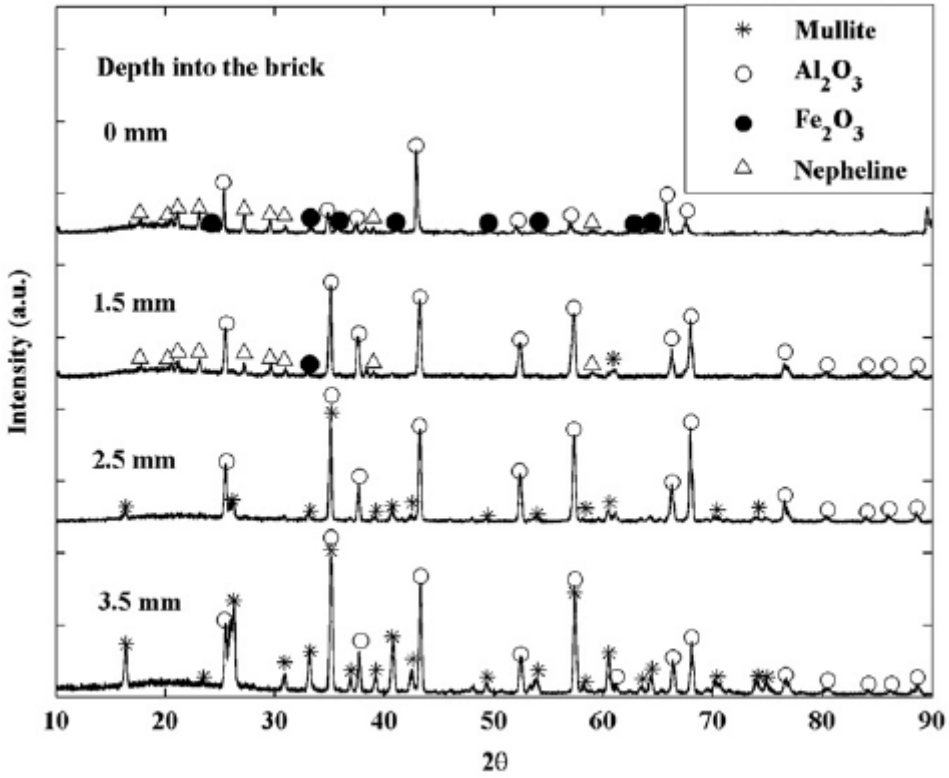

Figure 2: Diffractogram obtained from surfaces ground and polished to various depths in the bauxite-based refractory brick with sodium doped deposit. (J. Stjernberg et al. 2013)

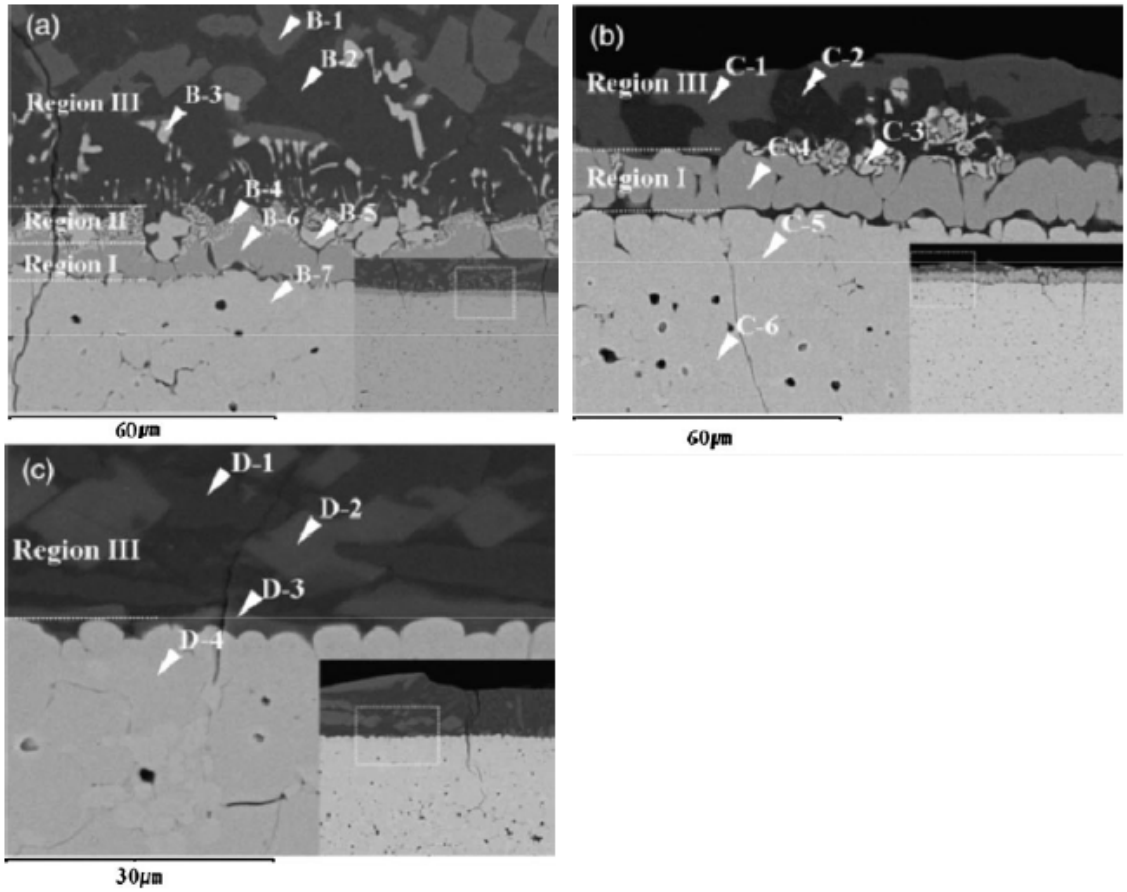

Figure 3: Microstructure of the Zirconia-Slag interface after corrosion by slag containing CaO-SiO_2-MgO with added 7 wt% (a), 13 wt% (b) and 19 wt% (c) CaF_2. (Park et al. 2010)

From these experiments, it can be concluded that the corrosion of zirconia refractories was found to be accelerated with an increased concentration of fluorspar which facilitated the dissolution of intermediate compounds. (Park et al. 2010)

Experiments were conducted by Park et al. (2010) with the same slag and doloma refractories using the finger test method. Here the additional fluorspar concentrations were 5, 10 and 20 wt% in the slag. It was found that 5 wt% fluorspar addition did not significantly affect the penetration depth whereas the 10 and 20 wt% additions completely infiltrated the finger. The penetration is attributed to the decrease in viscosity of the slag by the 10 wt% fluorspar addition since this decreases the viscosity of the slag from 1.35 to 0.07 $Pa \cdot s$, further additions of fluorspar don't have a significant effect on the further reduction of the viscosity. The addition of fluorspar to the slag also increases the solubility of periclase and doloma, thereby increasing the driving force of their dissolution from the brick. (Park et al. 2010)

The experiments conducted with magnesia refractories were conducted in an induction furnace. The amount of fluorspar added was between 2-22 wt%. Fluorine was only found in the C2S phase with a 2 wt% fluorspar addition (Figure 4 B). With additions of 6 wt% or more, fluorine was also located in the slag phase that penetrated the refractory (Figures 4 D, E & F). The deeper penetration is contributed to the lower viscosity due to higher fluorspar additions. The slag penetration caused the MgO grain to dissolve and detach from the hot face. It can, however, be noted that the reaction products of the desulphurisation reaction ((Ca, Mg)S) found in Figures 4 D through F indicate that fluorspar enhanced the desulphurisation reaction. (Park et al. 2010)

Han et al. (2018) investigated the effect of fluorspar on the degradation of a magnesia based refractory used in the production of high-clean steel. First the effect of fluorspar on the slag penetration into the magnesia refractories was determined using Back Scattered Electron (BSE) images, the result of these experiments can be seen in Figure 5.

From Figure 5 it can be observed that the penetration depth was affected by the CaF_2 content in the slag. In equilibrium experiments it was found that fluorspar had no significant influence on the magnesia equilibrium in the slag. It was found that in refractory corrosion experiments the refractory wall was smooth without fluorspar and grains could be observed in the experiments with fluorspar. Magnesia concentration peaks were also detected in the X-Ray Diffraction (XRD) analyses. This was interpreted as the fluorspar lowers the melting point of the binder which was a $CaO{-}SiO_2$-10%Al_2O_3 (C/S = 1.4) system. The corrosion process can then be visualised in Figure 6 as: the slag penetrates the refractory, the penetrated slag dissolves the binder and magnesia grains with sufficiently weakened support are detached. (Han et al. 2018)

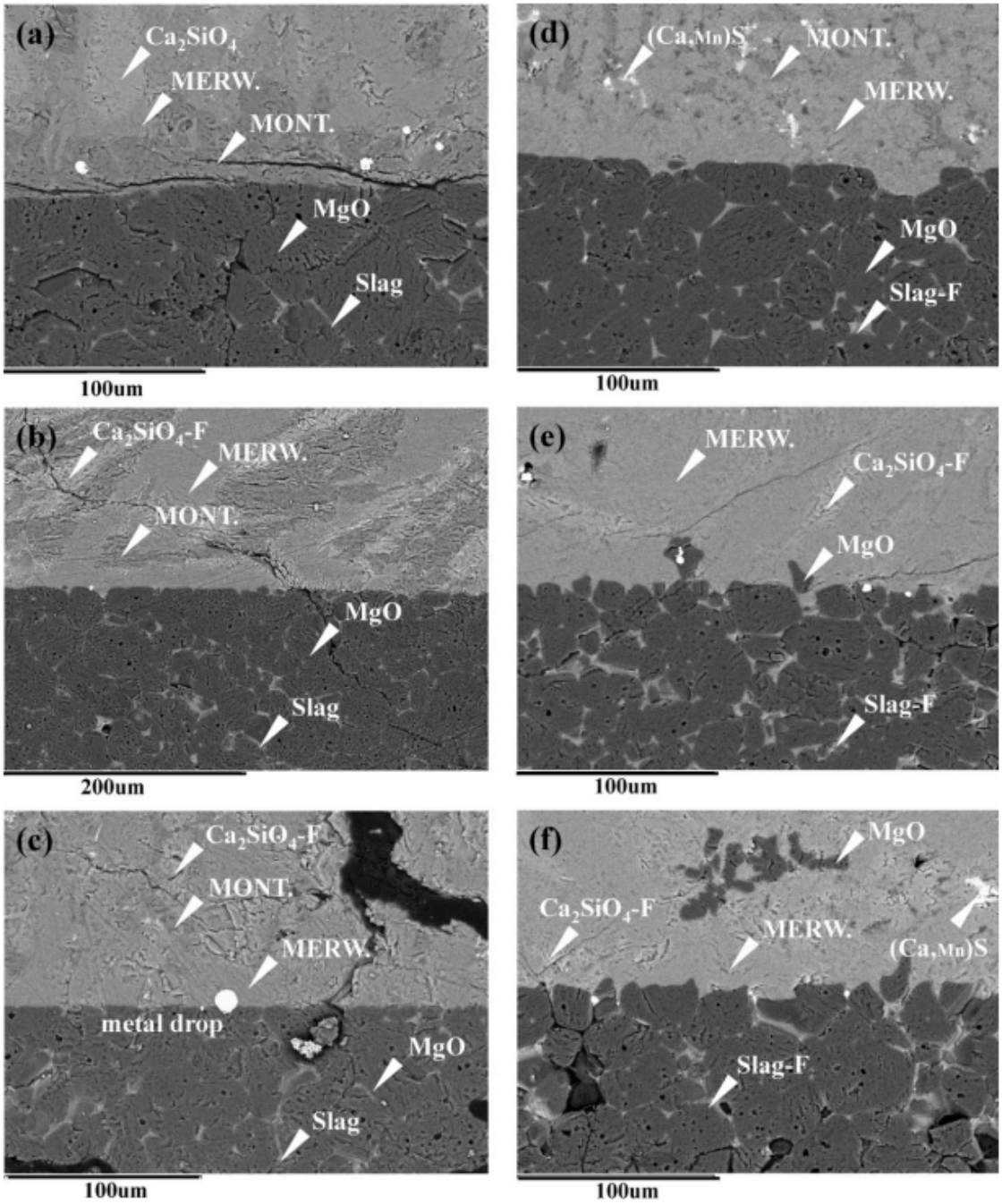

Figure 4: Magnesia slag corroded by slag containing CaO-SiO_2-MgO with added 0 wt% (a), 2 wt% (b), 4 wt% (c), 6.2 wt% (D), 14.4 wt% (E) and 21.7 wt% (F) CaF2. (Park et al. 2010)

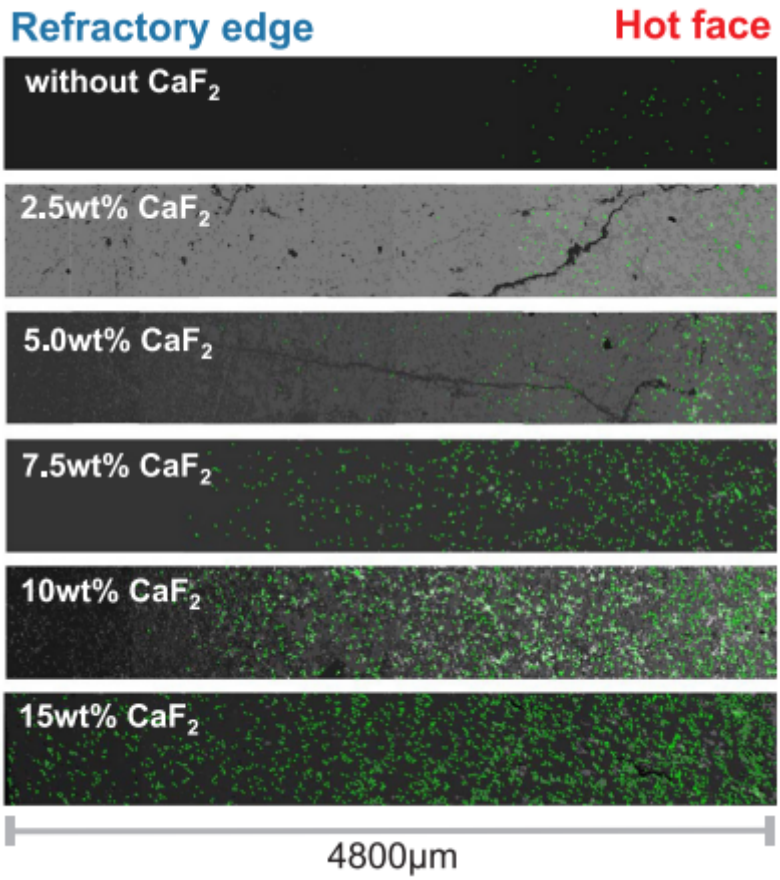

Figure 5: BSE image transormed from the Automatic Image analysis (AIA) program as a change of CaF_2 content. (Han et al. 2018)

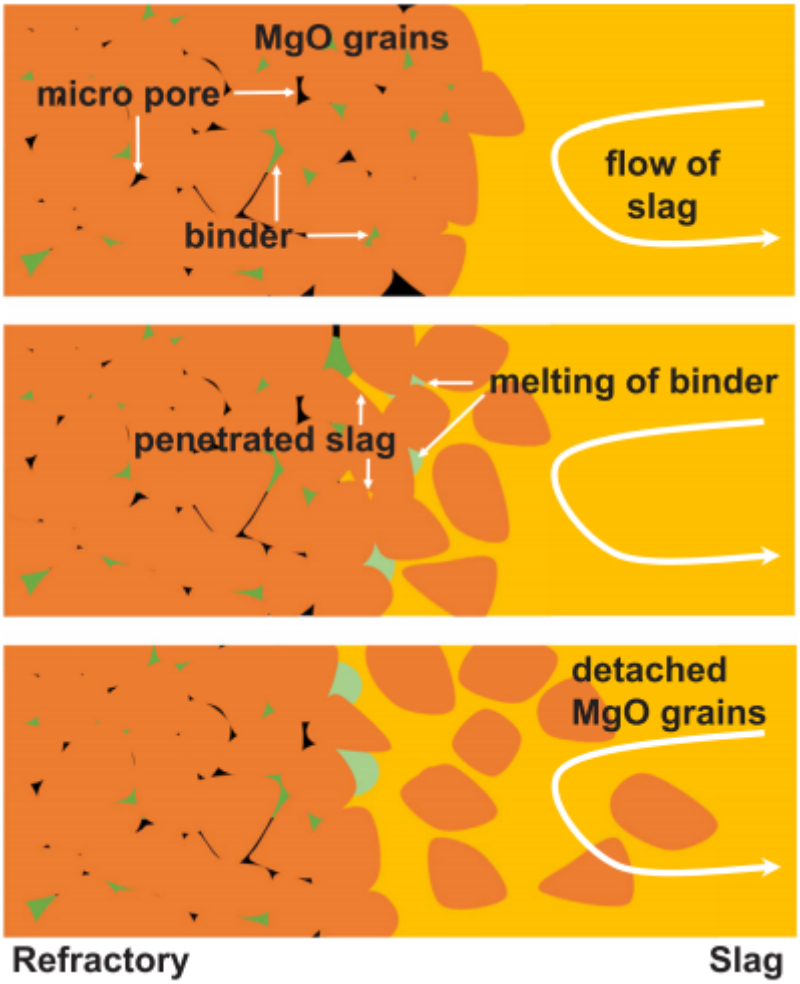

Figure 6: Schematic diagram of the slag penetration behaviour and the resulting detachment of MgO grains. (Han et al. 2018)

2.3.3 Zinc

The interaction of molten zinc with chamotte and MgO refractories was investigated by Luptáková, Anisimov, and Pešlová (2014). Static corrosion tests were used to evaluate the corrosion. For these, holes were drilled into the refractory. The zinc slag was then inserted into holes. The result of this study at 1000 °C can be seen in Figure 7.

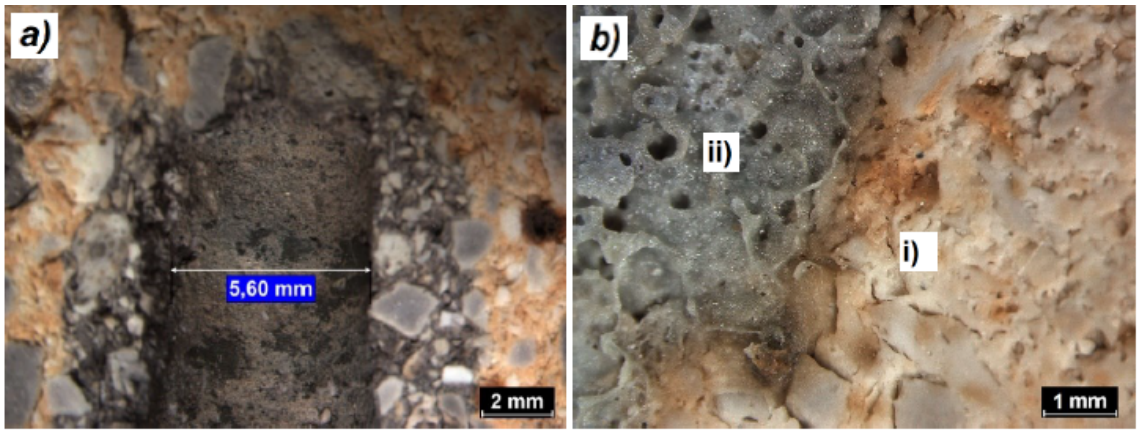

Figure 7: Interaction between chamotte refractory and molten zinc slag: a) cross section of the hole for the zinc, b) the interface between, i) the original material, and ii) the infiltrated area. (Luptáková, Anisimov, and Pešlová 2014)

It was found that zinc, zinc oxide and iron could penetrate the chamotte refractory. The infiltrated elements formed a silica-based glassy phase with a different structure than the original refractory. There is no evidence that the penetration generated new phases based on zinc, and zinc diffusion was only observed on the surface and in grains. The molten zinc did not penetrate the MgO refractory and there was no adhesive action on microscopic level. Minor amounts of zinc dendrite formation was detected. (Luptáková, Anisimov, and Pešlová 2014)

L. Chen et al. (2016) conducted experiments to determine the effect of the zinc oxide level on magnesia-chromite refractories. Rotating refractory finger tests were conducted using industrial fayalite slag which was provided by a copper-smelting company. In addition, magnesia crucible tests were conducted using synthetic fayalite slags to investigate in particular the effect of ZnO on the slag/MgO interaction. The experiments were conducted with an additional 0, 10 and 20 wt% zinc oxide added to the slag.

In the refractory finger tests, the finger was preheated and then immersed into the molten slag phase at 1200 °C for 4 hours with a rotational speed of 36 rpm. It was found that all slags predominantly corroded the periclase whereas the chromite showed limited reaction with the slag. The difference between the tests was that with higher zinc concentration in the slag the thickness of the newly formed (Fe, Mg, Zn)O solid solution layer also increased. The slag-refractory interface reactions can be seen in Figure 8. Figure 8 A and B show the interface in the finger tests and Figure 8 C and D show the crucible tests. It can be seen in Figure 8 A and B

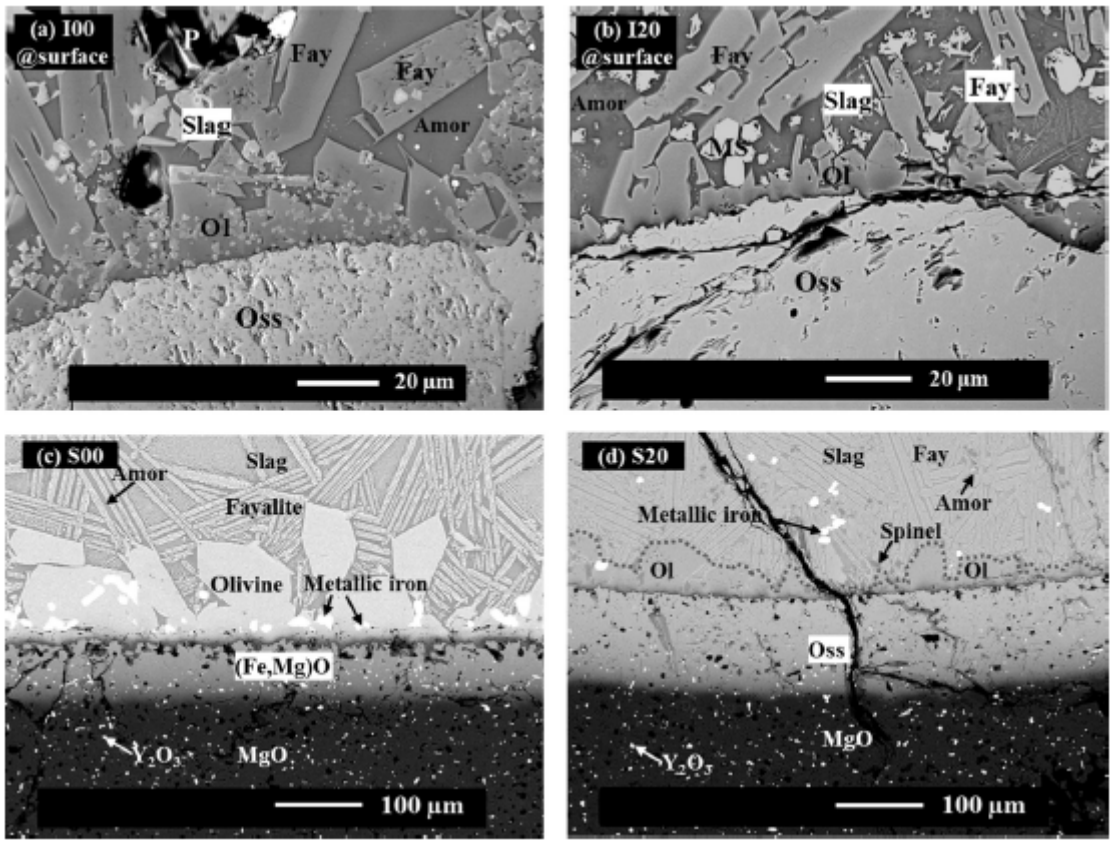

Figure 8: Backscattered electron (BSE) images of the MgO/slag interface after refractory finger tests (a & b), and MgO crucible tests (c & d). (L. Chen et al. 2016)

that the $(Fe,Mg,Zn)_2SiO_4$ solid solution (indicated by Ol) forms a continuous surface layer with a thickness of less than 20 micron on the (Fe, Mg, Zn)O layer (indicated by Oss) in the refractory fingers. The thickness of the Ol layer decreased with the increase in zinc oxide concentration. In the crucible tests it was found that the 0% zinc addition sample formed olivine with a grain size of over 100 micron whereas the 20% zinc addition sample formed smaller grain sizes (Figure 8). It is assumed that the lower silica concentration at higher zinc content hinders the formation of olivine. The main corrosive mechanism of chromite was found to be the diffusion from zinc oxide from the slag into the chromite grains thereby removing the magnesia from the chromite grains towards the slag. (L. Chen et al. 2016)

Snegirev, Perepelitsyn, and Kudryavtseva (1984) conducted experiments on the interactions between molten zinc with aluminosilicate refractories to clear discrepancies in the literature. Literature concluding that zinc does cause failure of the refractories and literature that concludes that it does not, both exist. Samples of the lining after service in a furnace for melting cathodic zinc were investigated. It was found that the impregnated zone was characterized by intensive penetration of metallic zinc filling the voids in the binder as well as the voids around the coarser chamotte fragments. The zinc that is in contact with the least affected refractory was in the form of zinc oxide. Petrographic and XRD analyses established that

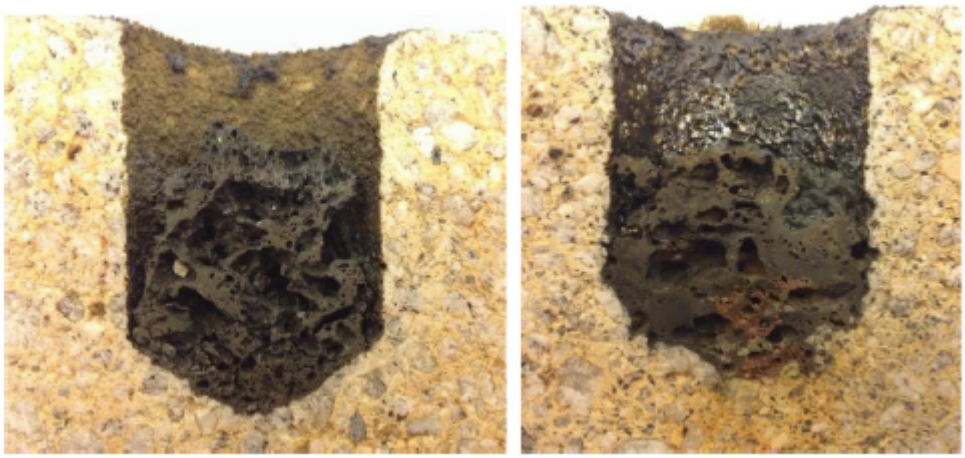

Figure 9: Cross-section view of the pure andalusite and 5 wt% SiC addition cups after 5 hours at 1250 °C in contact with the EAFD slag. (Aslanoglu, Baglan, and Soykan 2017)

the reaction products of the zinc oxide with the refractory resulted in willemite ($2\,ZnO \cdot SiO_2$), gahnite ($ZnO \cdot Al_2O_3$) and secondary corundum. These compounds replaced the original binder and part of the original chamotte grains. Therefore, it can be concluded that the interaction with the refractories and molten zinc does cause refractory failure. (Snegirev, Perepelitsyn, and Kudryavtseva 1984)

Aslanoglu, Baglan, and Soykan (2017) investigated the influence of SiC additions on the properties of andalusite refractory materials. The bricks that were investigated contained SiC concentrations of 0, 5, 10, 15 and 30 wt% substituted in the andalusite matrix. Three cycles of five-hour long slag penetration experiments were conducted at 1250 °C in an EAF. The 5 and 10 wt% SiC addition samples had a decreased apparent porosity compared to pure andalusite and the 15 and 30 wt% SiC addition samples had an increased apparent porosity. In Figure 9 a half-cup-visual is presented of the andalusite refractory and the 5 wt% SiC refractory after one slag penetration cycle. Here it can be seen that the slag penetration is similar for the cups. On the silicon carbide containing cup a shiny glassy phase can be seen which formed on the wall of the cup.

The shiny glassy phase layer can be caused by the oxidation of silicon carbide. The product of this oxidation is a dense layer that behaves as a barrier. Scanning Electron Microscope (SEM) analysis revealed a low amount of iron nodules and dispersed zinc particles within the refractory. For the 5 wt% SiC addition it was revealed that the glassy layer mainly consists of FeO-SiO_2-CaO. The surface where the refractory and the slag were in contact was heavily penetrated by lead and iron. Lead and iron were mainly present in oxide form in the refractory which suggests that they were carried as a vapour phase into the brick. Zinc has a tendency to penetrate deep into the brick. This was not the case in the experiments with SiC additions; consequently, SiC might behave as a barrier for zinc penetration. Finally, the analysis from just beneath the slag-refractory interface reveals that the samples with SiC

addition have much more impurities compared to the sample of pure andalusite. This might cause a denser slag near the interface, due to the removal of impurities from the slag. Increased slag density reduces the slag penetration. (Aslanoglu, Baglan, and Soykan 2017)

2.3.4 Corrosion by other solid or liquid means

In primary copper smelting the most industrially used refractory is a magnesia-chrome refractory and, as previously discussed, these refractories have excellent resistance to basic slags. Although, the possible formation of Cr^{6+} has more recently caused interest in magnesia and alumina alternatives, magnesia-chrome refractories are still widely used. The slag used in primary copper smelting is a ferrous silicate slag which is considered as an acidic slag due to the high silica activity in the slag. The process of chemical corrosion then occurs via the dissolution of magnesia. The chromite grains do not dissolve, although the grains can be washed away if enough of the supporting magnesia is dissolved. Increased chromite concentrations can increase the resistance to corrosion. The advantage of using a higher magnesia content refractory is that the reaction product of the dissolved magnesia and the slag form a phase near the hot face that can be solidified. The solidified phase then forms a freeze lining. A freeze lining can be defined as a protective layer of solid material created by solidifying part of the bath material by cooling down the refractory shell. (Crivits 2016) The formed freeze lining then acts as a barrier for further interactions between the slag and the refractory. A freeze lining works better, in this case, than increasing chromite concentrations for increasing the refractory lifetime. (Malfliet et al. 2014)

The utilization of biomass is being investigated as a second fuel to be burned next to coal. This is a more carbon neutral method since the carbon emitted when burning biomass is used to produce the biomass. The challenge is that the, in this research, investigated second fuel, straw, has a high potassium and chlorine content. These elements together with amongst others minor amounts of sodium and sulphur are released into the gas phase during combustion. Deposits of potassium sulphate and chloride together with ash can then corrode the boiler tubes and reduce heat transfer. It must be noted that in contrast to metallurgical furnaces where the atmosphere is typically reducing, in coal and biomass combustion the atmosphere is oxidising. (Wei et al. 2002) The interaction between chlorine and alkali metals has been investigated related to the co-combustion of coal and biomass. Dayton conducted combustion experiments of pure coal and straw and compared those with the combustion of a blend of coal and straw. The amounts of NaCl, HCl and KCl released when burning these pure fuels and blends can be seen in Figure 10. (Dayton, Belle-Oudry, and Nordin 1999)

It was found that the chlorine released from a coal and straw blend was affected by blending the two fuels. The HCl(g) concentrations were higher than expected and KCl(g) and NaCl(g) concentrations were lower than expected. Chemical equilibrium analysis showed that increased silicon and aluminium affected the alkali retention as a condensed species. When co-combusting straw with different coals around 70% of the potassium was predicted to form Sandine. For sodium the distribution

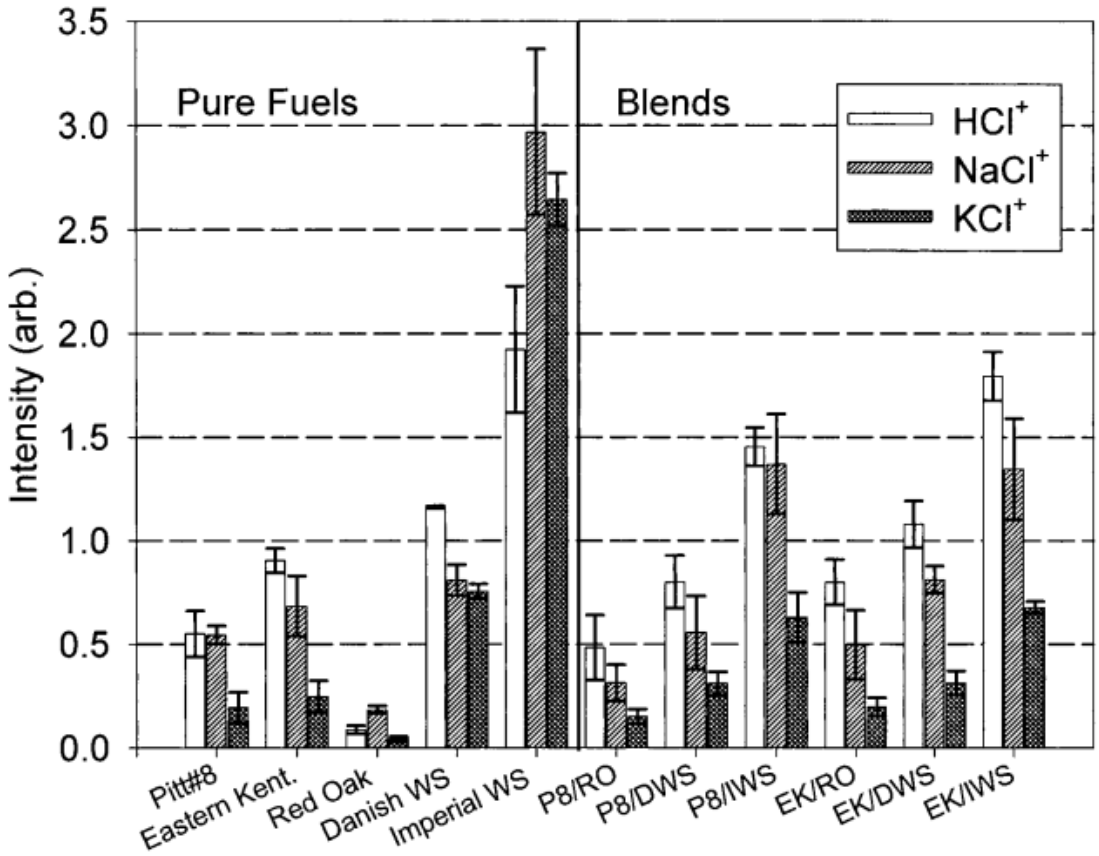

Figure 10: Relative amounts of HCl, NaCl and KCl released during the combustion of pure fuels and fuel blends consisting of 15% biomass/coal. Burned at 1100 °C with 20% oxygen in helium. (Dayton, Belle-Oudry, and Nordin 1999)

uncertainty was much higher, for different blends 18-100%, 10-80% and 40-75% of the sodium was predicted to form albite. The formation of these minerals, and accompanied consumption of the alkalis, can explain the lower than expected alkali chloride concentration. The higher than expected HCl concentration can then be explained by the decreased amount of alkalis for the formation of alkali chlorides. (Dayton, Belle-Oudry, and Nordin 1999) It was shown that alkalis can be bound by silicon and aluminium. This was further tested by Coda et al. (2001), here Kaolin and bauxite additives were used to bind alkalis. Wei did experiments on coal and straw blends but investigated the interactions of a wider range of elements. Alkali interactions with aluminium and silica were investigated together with the influence of calcium and magnesium. Thermodynamics show a more stable bond from potassium with aluminium silicate over bonds with calcium and magnesium. Higher concentrations of calcium and magnesium can still cause the formation of calcium- or magnesium aluminium silicates leaving a reduced amount of aluminium silicate to bind with potassium. (Wei et al. 2002) Also for coal gasification research efforts have been done to investigate the effects of co-gasification of coal and straw blends. The ash from coal and straw gasification blends has a higher alkali content. This higher alkali content reduces the ash fusion temperature, which is associated with a decreased slag viscosity. The advantage of a lower ash fusion temperature are lower thermal stress on the refractory lining and lower consumption of flux additives and oxygen. The disadvantage is the corrosion potential of higher alkali content ashes towards metallic and ceramic materials. (Zhang et al. 2015) Experiments conducted by Zhang et al. (2015) investigated the effect of coal, straw and two coal and straw blends on an alumina refractory. The results of these experiments can be seen in Figure 11.

First the difference between the higher melting point coal over the lower melting point wheat straw can be seen. The coal sample infiltrated the refractory 1.2 mm, wheat straw 2.2 mm, 10% straw blend 2.9 mm and 50% straw blend 5.8 mm. The refractory infiltration has been studied by SEM-EDX measurements, the resulting pictures can be seen in Figure 12 Aluminium has been used to depict the refractory while silicon, calcium and potassium have been used to illustrate the infiltration. Calcium was also used as part of the binder matrix which increased the amounts throughout the sample. (Zhang et al. 2015)

The pre-existing porosity can explain the slight infiltration of the coal sample. The 10% straw blend has infiltrated deeper than the pure coal, the weak infiltration of both the 10% straw blend and pure coal can be a consequence of unmelted minerals leading to less liquid phase to penetrate. The pure straw has wetted the refractory surface significantly. It remained, however, on the surface of the refractory with very weak infiltration. The corrosion mechanism here is also different in that it infiltrated only the binder while not affecting the larger grains. The 50% has infiltrated the refractory the deepest, this slag has also infiltrated the binder matrix of the refractory and a reaction rim formed at the alumina grains. (Zhang et al. 2015)

J. Chen, L. Chen, et al. (2018) investigated the effects of Ti_3AlC_2 additions to alumina carborundum refractories Al_2O_3-SiC. These refractories are used in steelmaking but suffer from two main drawbacks. The carbon in the refractory

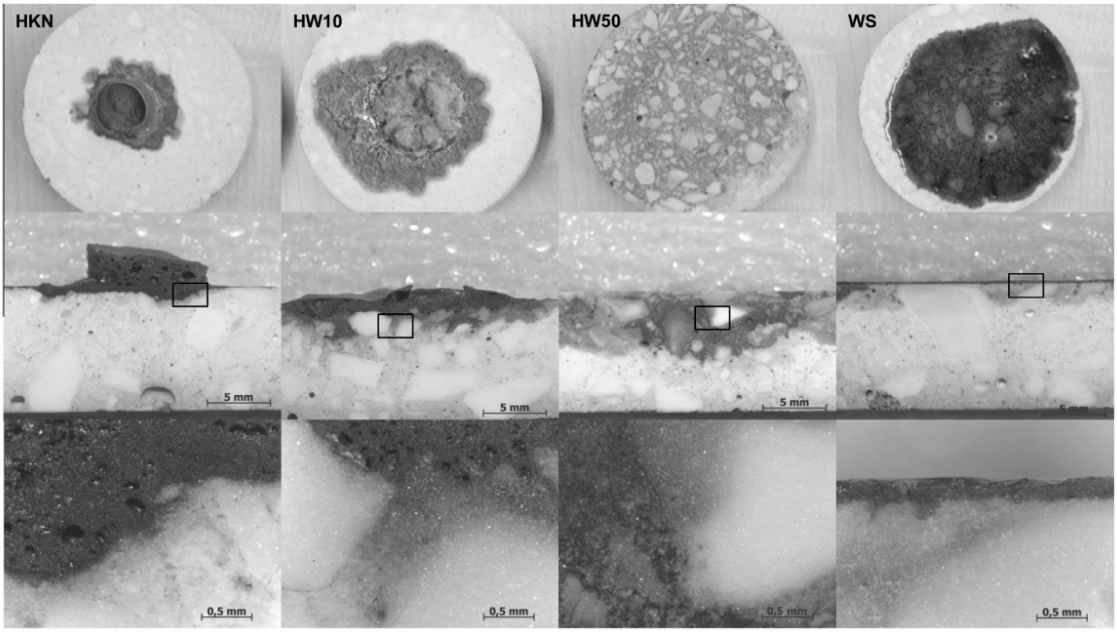

Figure 11: Macroscopic and microscopic images of the surfaces and cross sections of the refractory samples. The area of the picture with the highest magnification has been indicated by a square in the picture above. (Zhang et al. 2015)

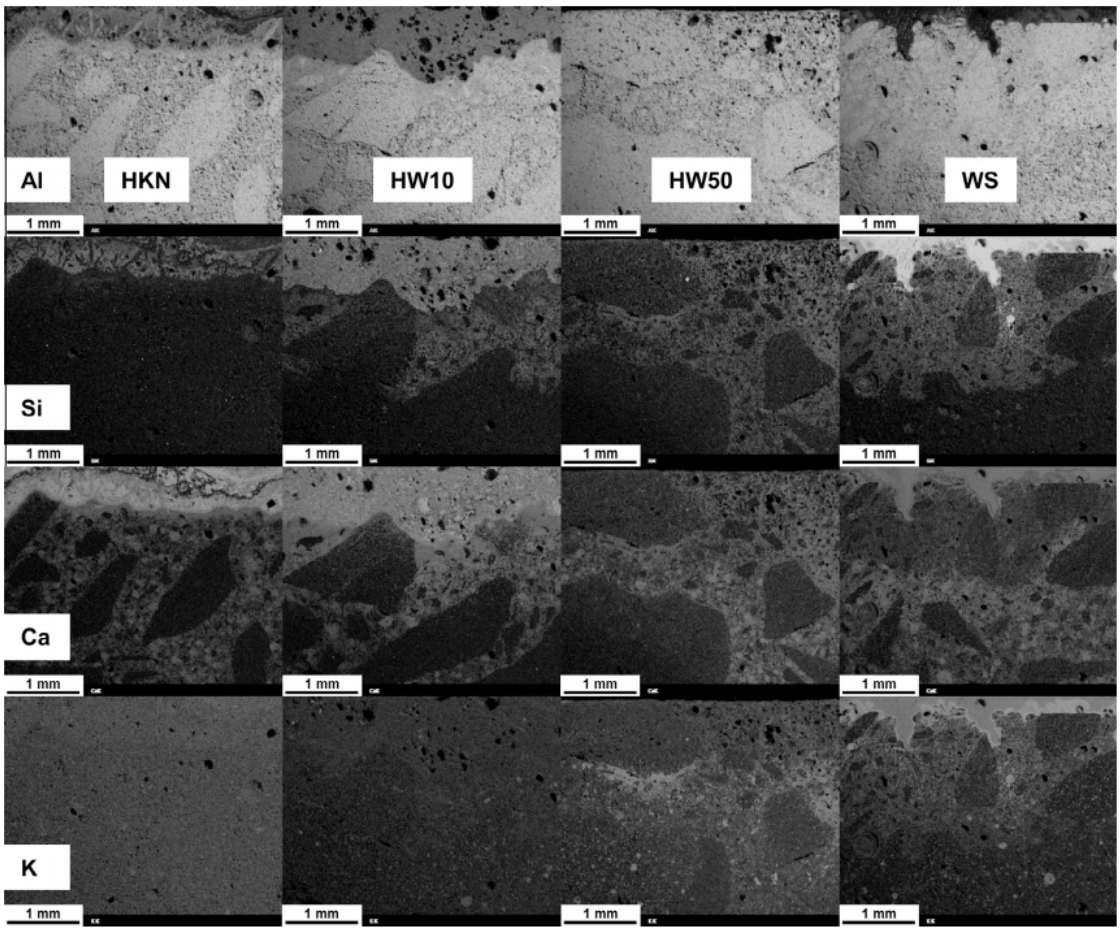

Figure 12: Distribution of the elements Al, Si, Ca, and K for the four ceramic discs after heating experiments at 100-fold magnification. Brighter regions indicate a higher concentration for the respective element. (Zhang et al. 2015)

can be a source of carbon for the molten steel and the high thermal conductivity impacts the metallurgical operation negatively. Reducing carbon concentrations in the refractory by addition of Ti_3AlC_2 positively affects the two drawbacks mentioned above. Further, it was found that the Ti_3AlC_2 addition lead to an increase in the corrosion resistance of the refractory. The doping reacted with calcium from the slag forming calcium hexaaluminate, which both trapped calcium and suppressed further penetration into the refractory brick. (J. Chen, L. Chen, et al. 2018)

2.4 Refractory corrosion by gas phase compounds

Vapours can penetrate the pores of the refractory material in a furnace, inside of the refractory material the vapours can react with the refractory materials and form new compounds. The formation of new compounds coming from the addition of gaseous substances in the refractory matrix may cause expansion or the formation of substances with lower melting or boiling points. Expansion commonly leads to cracking corrosion in the refractory material. (Oprea 2004) The formation of compounds with lower melting or boiling points causes the refractory material to lose material and thus strength. (DeLucia and Wolfe 2000) Reducing the porosity and thus the amount of gas penetrating the refractory improves the resistance to gaseous corrosion. (Prigent, Bouchetou, and Poirier 2011)

2.4.1 Sodium and potassium

Stjernberg (2008) conducted experiments on three different mullite based refractories. It was found that when both sodium and potassium oxides are present in the slag that the potassium reacts more with the refractory at the slag-refractory interface and most of the sodium evaporates. This causes more of the sodium to interact on the gas refractory interface. (Stjernberg 2008)

Scudeller, Longo, and Varela (1990) used two different refractory bricks, one with 45% silica and one with 55% silica, to determine the vapour attack on alumina-silica refractories by potassium vapour. The bricks were covered in metallurgical coke and potassium carbonate, the sample was then heated at 1000 °C under nitrogen atmosphere. Using XRD it was determined that the potassium vapour that penetrates the refractory pores attacks the silica and alumina. This attack produces a glassy phase, from which, subsequently, kaliophilite ($K \cdot AlSiO_4$) can crystallize. After the concentration of kaliophilite increases to sufficiently high levels, it can react with silica in the refractories to form leucite ($K \cdot AlSi_2O_6$). The expansion caused by these minerals can lead to crack formation in the refractory block. (Scudeller, Longo, and Varela 1990)

Spear and Allendorf (2002) used thermodynamic equilibrium calculations to investigate the corrosion of alumina refractories by sodium- and potassium hydroxide under oxidising conditions. The thermodynamic calculations suggest that alumina refractories are stable with respect to corrosion by the alkali hydroxides. Liquid phase products become stable only above 1584 °C in sodium-alumina systems (Figure 13) and 1912 °C in in potassium alumina systems (Figure 14).

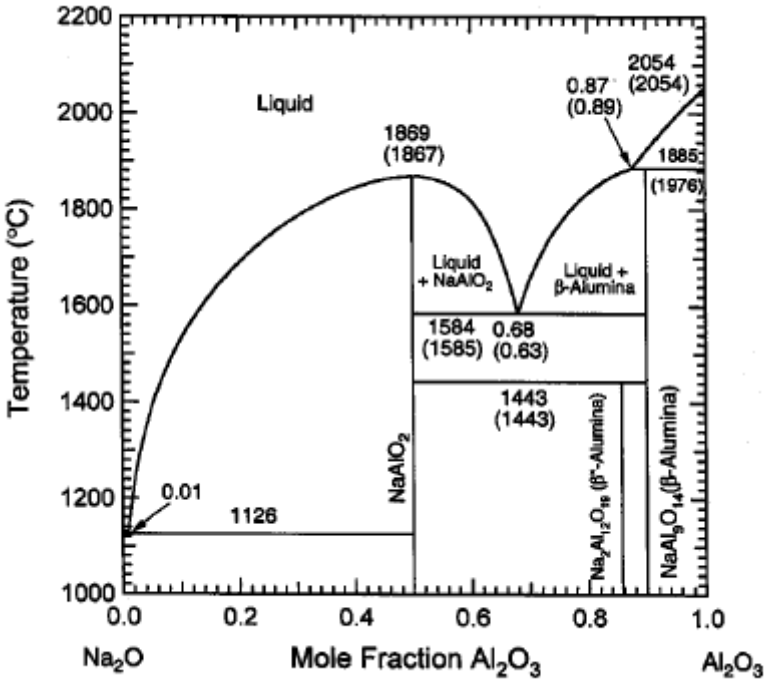

Figure 13: Calculated phase diagram for the $Na_2O-Al_2O_3$ system. (Spear and Allendorf 2002)

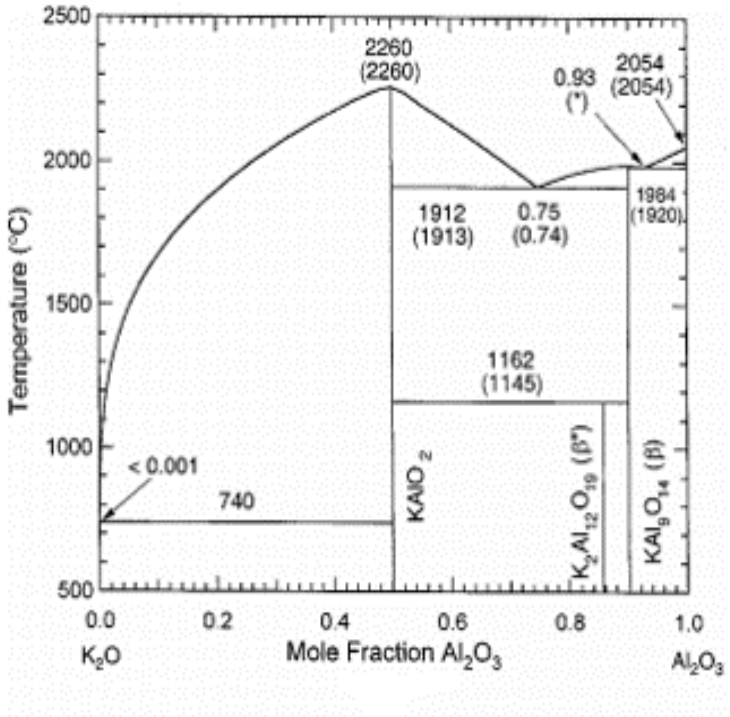

Figure 14: Calculated phase diagram for the $K_2O-Al_2O_3$ system. (Spear and Allendorf 2002)

In contrast, sodium oxide can form a liquid phase with silica (Na_2O-SiO_2) at 817 °C. The potassium can also react with the glassy matrix forming a low melting point liquid silicate phase. In high alumina refractories, potassium can react to form potassium aluminate at temperatures above 923 °C. (Hayashi, Nishio, and Ayuzawa 1983; Spear and Allendorf 2002)

Alumino-silicate refractories are sensitive to corrosion by sodium vapours, which can react with the refractory material to form a low melting sodium oxide rich glassy phase. (Spear and Allendorf 2002)

Mullite can also suffer from reactions with sodium. Sodium can react with free silica in the mullite refractory forming natrosilite phases (($Na_2Si_2O_5$). These natrosilite phases can further react with the mullite forming albite (($NaAlSi_3O_8$) and nepheline (($NaAlSiO_4$) phases. The formation of albite and nepheline are associated with approximately 3% volume expansion within the refractory brick. Above temperatures of 1100 °C beta alumina becomes the stable alumina structure, this structure change is associated with further volume expansion. (Mahapatra 2019)

Criado, Moya, and Aza (1981) conducted experiments on high alumina refractory bonded by calcium hexaluminate under oxidising conditions at 1200°C and 1400°C. Samples of 5 to 7 mm thick were cut from the refractory brick and set on top of a crucible containing 3.6 g of Na_2CO_3 or K_2CO_3 which was then heated. The XRD intensity graph of the reaction products formed when the refractory was attacked by Na_2CO_3 at 1200°C is shown in Figure 15. Here it can be seen that the attack by Na_2CO_3 formed sodium aluminate up to a depth of 0.5 mm, which is incompatible with the binding agent. Furthermore,$Na_2O\beta \cdot Al_2O_3$ formed up to a depth of 1.1 mm.

In the experiments conducted with potassium carbonate at 1200°C and 1400°C only potassium $\beta \cdot Al_2O_3$ was detected, at 1400°C it was the only phase detected throughout the sample. SEM observations of the samples gave evidence that the damage of the original microstructure was greater in the case of potassium carbonate attack over sodium carbonate. This sample also showed an expansion of about 20% and due to the change of structure a strong decrease in mechanical properties, both can have drastic effects on operational safety. (Criado, Moya, and Aza 1981)

Prigent, Bouchetou, and Poirier (2011) studied the chemical attack of sodium vapours on alumina refractories using laboratory tests developed to simulate industrial operating conditions. The setup consists of a carbon crucible containing either sodium hydroxide or sodium fluoride. The carbon crucible is used to trigger formation of carbon monoxide at high temperature, and the sodium compounds are used as the source of gaseous sodium. The carbon crucible is placed inside of a high-density alumina crucible to protect the carbon crucible from oxidising in the electric furnace. A schematic of the setup for use with aggregates and refractory bricks can be seen in Figure 16.

Different bricks composed of clay (binder), fine alumina and fireclay or andalusite (Al_2SiO_5) were used. After attack by gaseous sodium, the refractories made of fireclay and clay were found to form more glassy phases than in the refractories composed more of andalusite and clay. The amount of glassy phase in the fireclay brick was 49% after the corrosion test where the andalusite brick had 30% glassy phases. Corundum needles formed in both brick matrices. In the fireclay brick it formed in the liquid

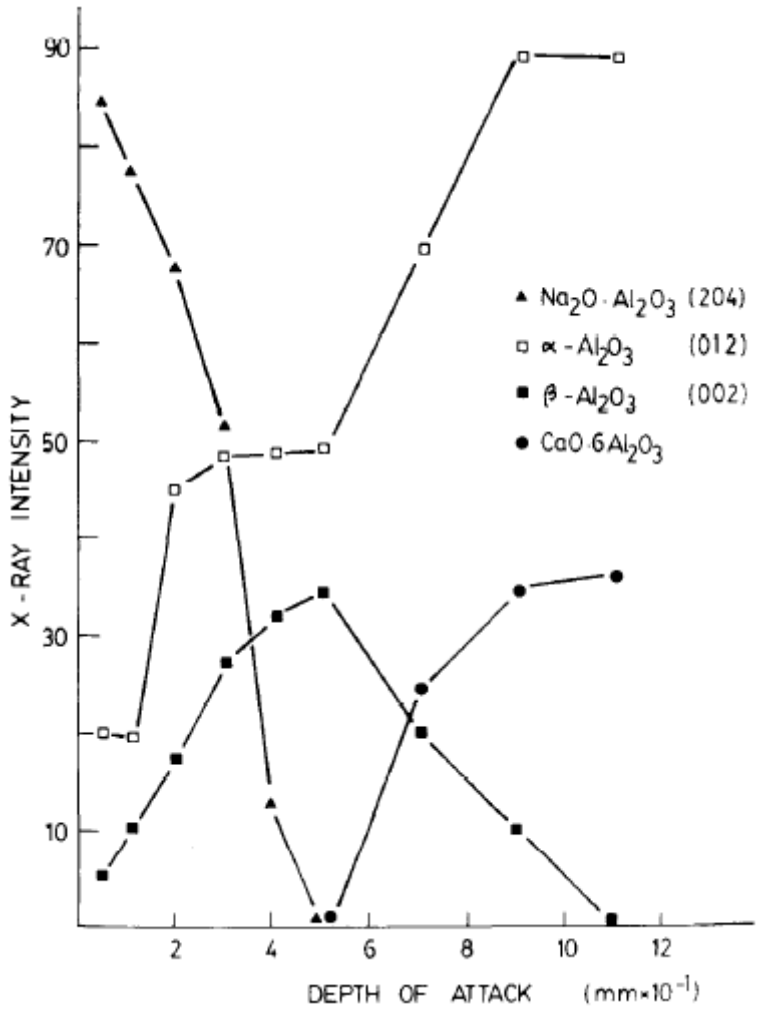

Figure 15: X-ray intensity vs. depth of attack by Na2CO3 vapour at 1200°C. (Criado, Moya, and Aza 1981)

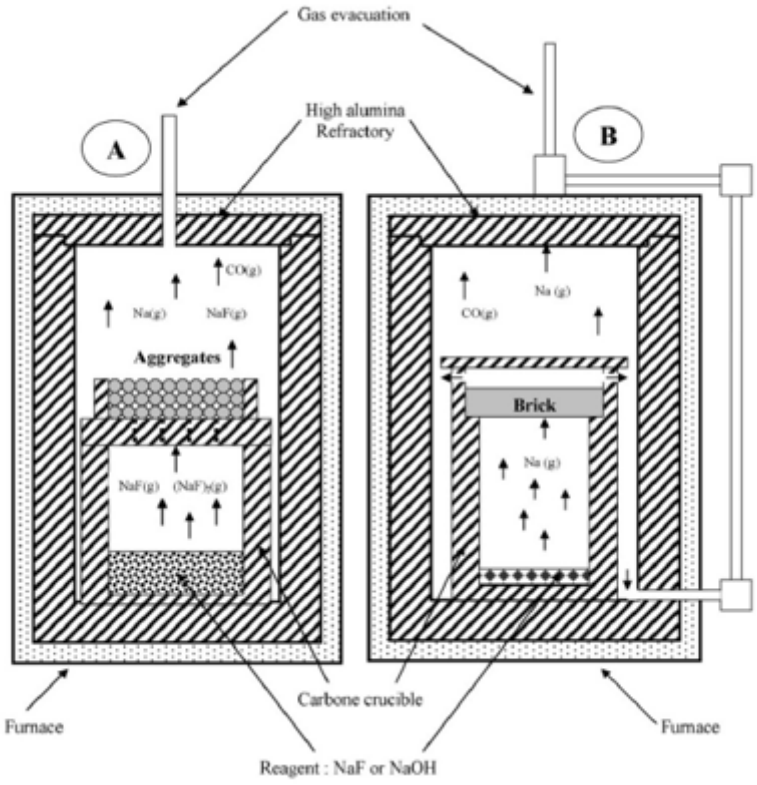

Figure 16: Schematic of the setup used to simulate corrosion of aggregates and refractory bricks under industrial conditions. (Prigent, Bouchetou, and Poirier 2011)

phase during cooling whereas in the andalusite the crystallization happened at high temperature.

Both fireclay and andalusite refractory raw materials reacted extensively with the sodium forming liquid phases. Andalusite suffers from corrosion by sodium in the same way as the fireclay, but in the andalusite refractory brick, the capillary network formed by the mullite crystal trapped the glassy phase. This causes mullitised andalusite bricks to have excellent corrosion resisting qualities. (Prigent, Bouchetou, and Poirier 2011)

Narita et al. (1981) investigated the refractories of a blast furnace after 102 months of operation. Here it was found that fireclay bricks used as refractory bricks at the upper part of the shaft hardly wore, lower into the furnace the wear increased. Between the tuyere the fireclay brick suffered significant wear with numerous cracks. Potassium concentrations inside the brick were high near the surface and reacted with the fireclay forming kalsilite ($K_2O \cdot Al_2O_3 \cdot 2\,SiO_2$) according to XRD. The penetration of sodium was far less severe than the penetration of potassium, the sodium concentration was less than one fifth of the potassium concentration. Zinc tended to penetrate deeper into the brick and was found in both zincite (ZnO) and willemite ($2\,ZnO \cdot SiO_2$) forms. It was also found that the thickness of fireclay brick installed in the tuyere zone swelled by 105-130% compared to its original thickness. (Narita et al. 1981)

2.4.2 Fluorine and chlorine

Fluorine is a highly reactive compound, therefore it will also react with most or all refractory types. Magnesia refractories provide protection against alkali attack due to the repulsion from the positively charged alkali particles and the positively charged magnesium. Fluorine has a strong negative charge, which readily combines with the magnesium in magnesia refractories to form magnesium fluoride. Magnesium fluoride has a melting point of 1263 °C, thus it is less stable at higher temperatures. Fluorine also reacts with silica to form highly volatile silicon tetrafluoride. Since silica is commonly used in the bonding phases of refractories, this has a strong degrading effect on the refractory. (DeLucia and Wolfe 2000) More resistant to fluorine are chromium oxide, alumina or calcium aluminate refractories. Chromium reacts with fluorine to form chromium fluoride at high temperatures, which becomes highly volatile between 1100 °C and 1200 °C. Aluminium can react with fluorine to form aluminium fluoride, which is a stable compound with decent refractory properties. Aluminium fluoride does sublimate at 1291 °C. In the calcium aluminate refractory, both the aluminium and the calcium oxides are subject to attack. The calcium also forms calcium fluoride similar to the aluminium, and like aluminium fluoride it has some refractory properties. The melting point of calcium fluoride is 1402 °C. (DeLucia and Wolfe 2000)

Caprio and Wolfe (1982) reviewed refractories for hazardous waste incineration. The effects of fluorine and chlorine are similar, though fluorine acts as a flux in glassy silicates whereas this is not the case for chlorine. We can thus conclude that chlorine is less reactive in these conditions. Chlorine gas will react with bonding

phases in refractories forming products as calcium chloride from calcium aluminate and sodium chloride from sodium silicate. Chlorides can also condense together with alkalis forming expansive alkali chloride phases. Two examples were presented where chlorine reacted with alumina and silica resulting in the formation of volatile chlorides. In the first case the effect of chlorine on a 99% alumina brick is shown. The results of this can be seen in Figure 17, showing the loss of the bonding phase due to the chlorine attack.

It was also found that chlorine disrupts the matrix in mullite and the fractions have become coarser. This is attributed to the removal of silica in the form of silicon tetrachloride. (Caprio and Wolfe 1982) The simultaneous presence of carbon monoxide gas and chlorine gas can cause corrosion to alumina-chromia refractories. Both gases have to be present for the reaction, shown in reaction (1), to proceed. The carbon monoxide and chlorine gas react with the chromia which results in the formation of chromium or aluminium chloride. (Mahapatra 2019)

$$\mathrm{Cr_2O_3}(s) + 3\,\mathrm{CO}(g) + 3\,\mathrm{Cl_2}(g) \rightleftharpoons 2\,\mathrm{CrCl_3}(s) + 3\,\mathrm{CO_2}(g) \tag{1}$$

2.4.3 Zinc

Zinc has a low boiling point of only 907 °C, therefore zinc will most likely be in gas phase in furnace conditions. Zinc is also a relatively ignoble metal, thus it is able to reduce iron and chrome in refractories. Furthermore, zinc oxide can react with alumina in non-basic refractories. (Gregurek et al. 2016) Zinc oxide is shown to react with magnesia chromia refractories due to its similar size and valence forming (Zn, Mg)O solid solutions and with the chromia forming $\mathrm{ZnCr_2O_4}$. These reactions cause cracks to form in the refractory bricks. (Gregurek et al. 2016; Oprea 2004)

2.4.4 Other gases

Davis, Aksay, and Pask (1972) conducted experiments to investigate the decomposition of fused $\mathrm{SiO_2}$ 2:1 mullite ($2\,\mathrm{Al_2O_3} \cdot \mathrm{SiO_2}$). The experiments were conducted in high temperature environments at temperatures between 1650 and 1800 °C under static helium atmosphere at a pressure of approximately 0.7 atmosphere. Here it was found that operating under these conditions resulted in decreasing amounts of mullite and increasing amounts of alumina with increasing temperature and duration of the experiment. The proposed reaction is then as follows.

$$3\,\mathrm{Al_2O_3} \cdot 2\,\mathrm{SiO_2}(s) \rightleftharpoons 3\,\mathrm{Al_2O_3}(s) + 2\,\mathrm{SiO_2}(g) \tag{2}$$

Bubbles were observed at the interfaces of the fused mullite, it was proposed that silica participates in gas forming reactions. The decomposition of mullite cannot cause the formation of the observed bubbles since the equilibrium pressure of the decomposition products is lower than the helium pressure. Formation of silicon monoxide from liquid silica and silicon does have the required equilibrium pressure to form gas bubbles. Furthermore, carbon and silicon carbide reactions with silica

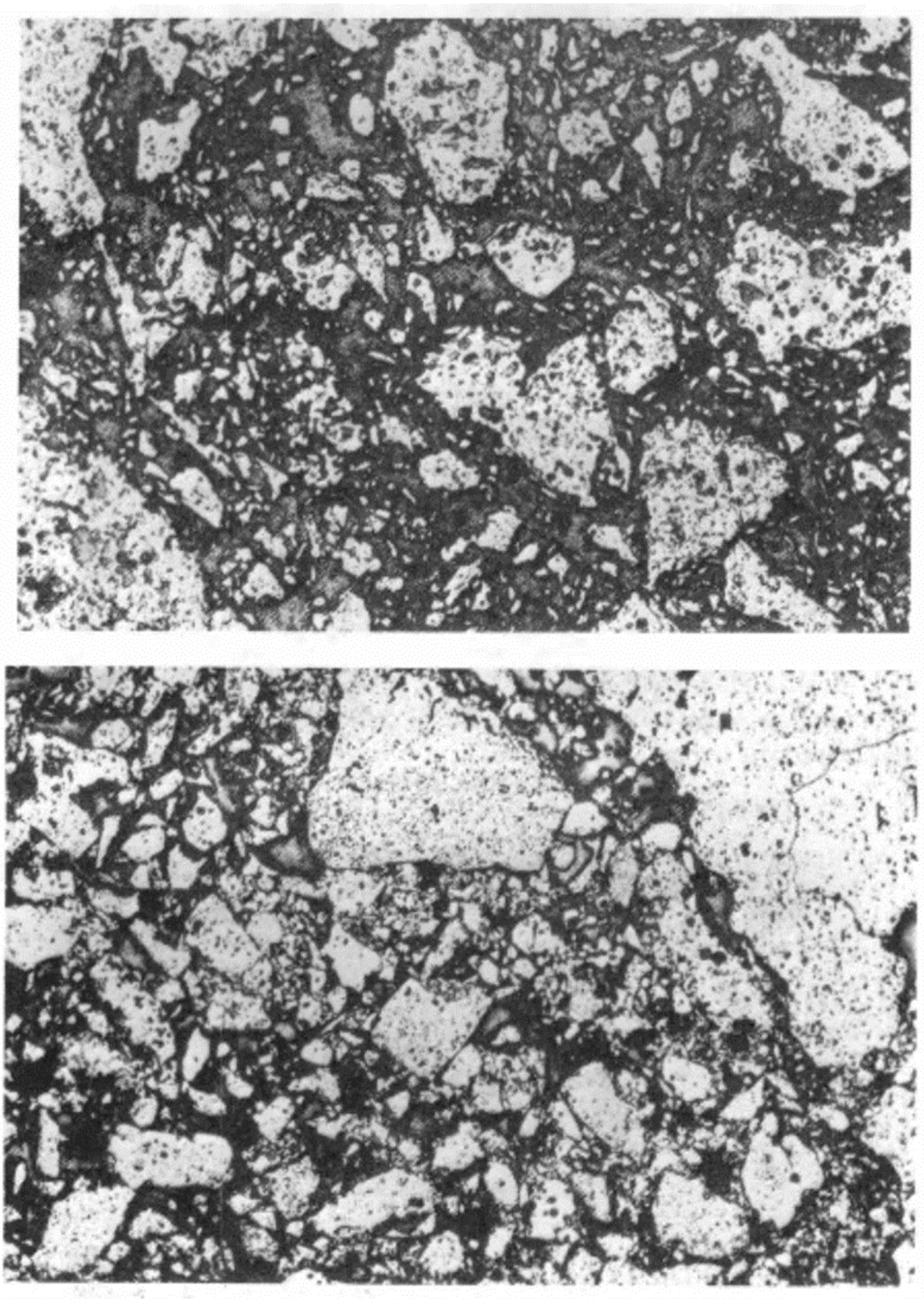

Figure 17: Ninety-nine percent alumina refractories before (top) and after (bottom) chlorine attack. (Caprio and Wolfe 1982)

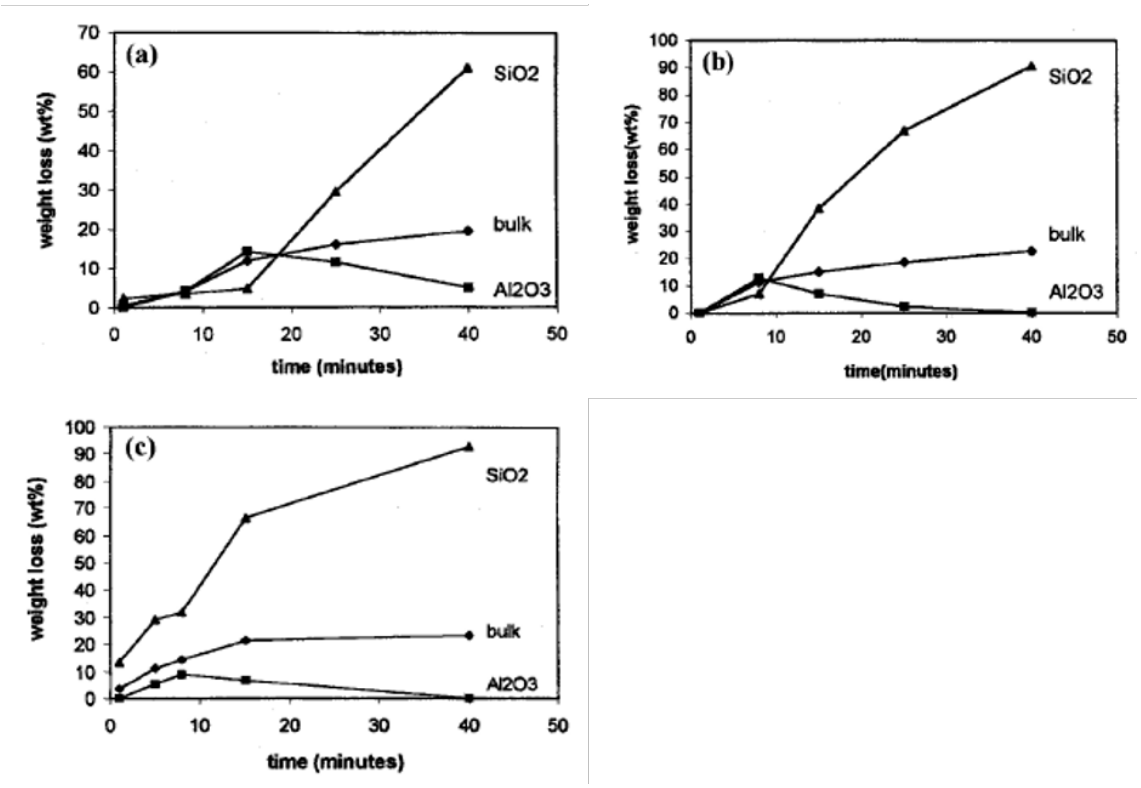

Figure 18: Mullite decomposition kinetic curves at (a) 1900 °C, (b) 1950 °C and (c) 2000 °C. (Xiao and Mitchell 2000)

also have the required equilibrium pressure to form gas bubbles. (Davis, Aksay, and Pask 1972)

Xiao and Mitchell (2000) conducted experiments on the stabilization of mullite refractories under carbon monoxide atmosphere. The decomposition of mullite has been reviewed previously by Davis, Aksay, and Pask (1972) under helium atmosphere. Kronert and Bahl (1978) investigated the decomposition of mullite under reducing atmosphere. Here it was found that under reducing conditions provided by a CO atmosphere in the temperature range of 1000-1600 °C, the silica in mullite forms silicon monoxide gas according to the following reaction. (Kronert and Bahl 1978)

$$3\,Al_2O_3 \cdot 2\,SiO_2(s) + 2\,CO(g) \rightleftharpoons 3\,Al_2O_3(s) + 2\,SiO(g) + 2\,CO_2(g) \qquad (3)$$

Xiao and Mitchell (2000) then conducted experiments on mullite decomposition in the 1900-2000 °C range under reducing conditions. About 1.6 g of mullite powder was used in these experiments. The results of this experiment can be found in Figure 18.

The weight loss of the individual components was determined using X-ray fluorescence spectrometry (XRF). In Figure 18, it can be seen that the weight loss of silica strongly increases with temperature and time. The weight loss kinetics in experiment C are similar to those of experiment B, except the silica loss before the beginning of experiment C which comes from evaporation of silica during the heating process.

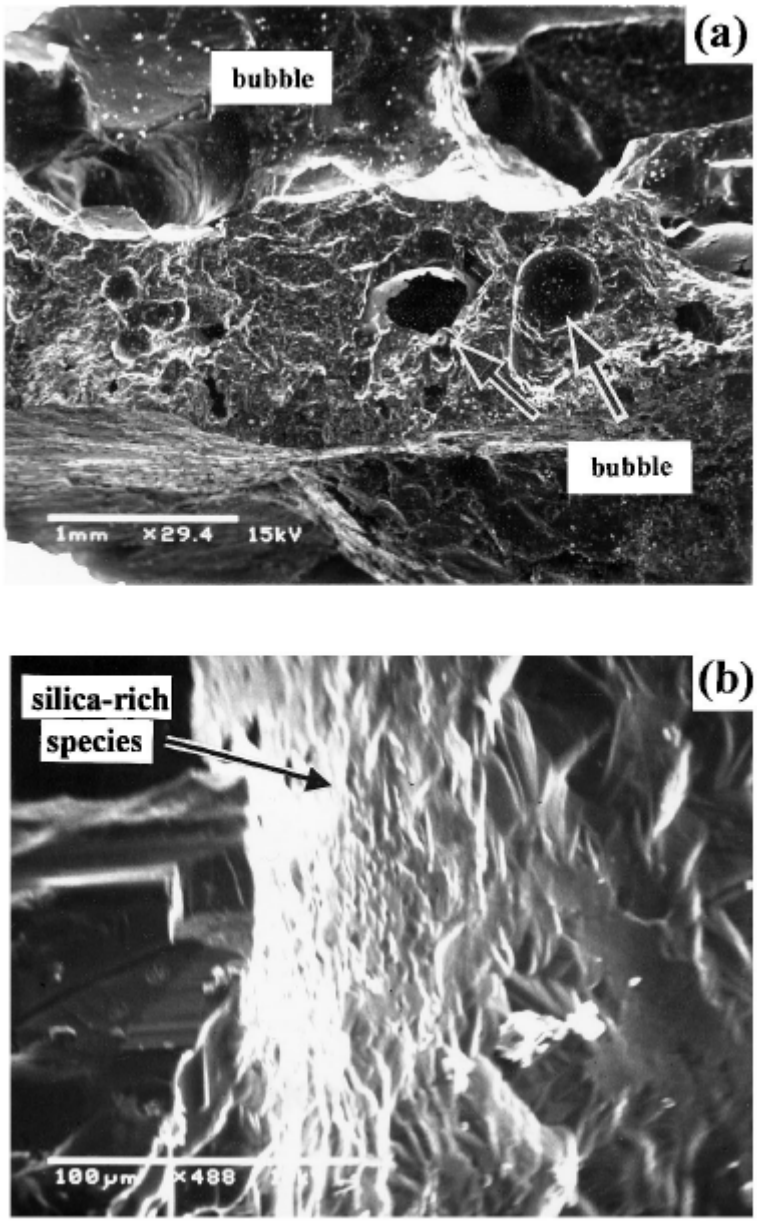

Figure 19: SEM images of (a) the cross-sectional area of the sample and (b) inside the surface of the bubble structure for the sample held at 1950 °C for 8 minutes. (Xiao and Mitchell 2000)

SEM images of the sample at 1950 °C for 8 minutes show a bubble structure on the bottom of the sample and bubbles trapped on the top of the melt. The SEM images can be found in Figure 19.

Xiao and Mitchell (2000) also investigated if adding excess silica to the mullite refractory could help stabilize the refractory. The result from this experiment can be found in Figure 20. About 0.36 g of excess silica was placed in a container above the mullite. In the Figure, the line with circle points is the weight loss of the excess

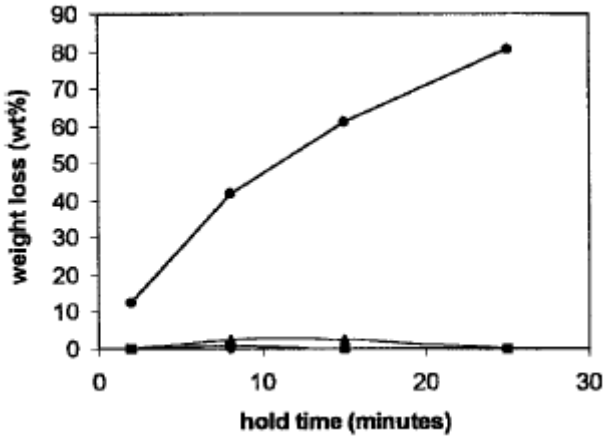

Figure 20: Effect of using excess silica (line with circle points) to supress silica evaporation from mullite. (Xiao and Mitchell 2000)

silica. It can be seen that adding excess silica supresses the weight loss of silica from the mullite since reactions with this free silica satisfy the reaction equilibrium. (Xiao and Mitchell 2000)

3 Materials and experimental methods

The purpose of this section is to describe the methods and experimental setup used in this work. Two sets of experiments were conducted. The first set of experiments was to study the melting behaviour of EAF and AOD dust. The second set of experiments was to study the interaction between four industrial refractories and a synthetic dust.

3.1 Material and sample preparation

The melting behaviour of three dusts was studied. The three different dusts were received from Outotec Research Center (ORC); two were EAF dusts (VKU1 & VKU2) and one was an AOD dust. The dust compositions can be found in Table 1. The dusts were pressed into briquettes of approximately 0.2 g by the application of 5 tons of force. This force was found to be necessary on the VKU2 dust since lower pressure did not achieve the formation of a briquette that would maintain its form and could be transported to the furnace.

The industrial refractories were received from ORC, and were cut to dimensions of 35x35x10 mm. The names of the refractory and their main constituent can be found in Table 2. They were then cut and ground into cylinders that cover the alumina crucible used to hold the dust. The synthetic dust was made by mixing 50 wt% K_2CO_3, 25 wt% KF and 25 wt% KCl.

3.2 Equipment

Melting behaviour experiments were conducted in a vertical 16/450 (maximum temperature: 1600 °C; heated length: 450 mm; Lenton, Parsons Lane, Hope, UK) laboratory furnace equipped with four silicon carbide heating elements, positioned near the alumina working tube (impervious pure alumina, 45/38 mm OD/ID). The inlet gases (Ar 99.999%, CO 99.97% & CO_2 99.9992% produced by AGA Linde) entered the furnace from the gas lance at the top of the furnace and outlet gases were guided out to the gas washing system at the bottom of the furnace. A vacuum ejector facilitated the gas outflow by creating an under pressure after the gas wash bottles. The inlet flow of Ar was controlled by rotameters (Kytola Instruments) and the inlet flow of CO and CO_2 was controlled digitally. A S-type (Pt/Pt-10 Rh Johnson-Matthey, London, UK, accuracy $\pm 3°C$, calibrated by the manufacturer according to ITS-90 standard, using the melting temperatures of palladium in air and gold as reference points) thermocouple connected to a Keithley type 2010 DMM multimeter (Keithley, solon, OH, USA; calibrated by the manufacturer) measured the temperature at the location where the samples were located during the experiments.

The wires used in the melting behaviour experiments were Kanthal A1 wires. In the refractory-dust interaction experiments a molybdenum crucible was mounted on an alumina rod. A magnesia crucible containing the dust could be placed inside the molybdenum crucible and the refractory lid could be placed on top of the magnesia crucible.

Table 1: Chemical compositions of the dust samples as measured by ORC.

	Weight percentage		
	VKU2	VKU1	AOD
Na	0.81	0.94	0.14
Mg	2.69	1.01	1.46
Al	0.54	0.36	0.2
P	< 0.05	< 0.05	< 0.05
K	1.07	0.97	0.14
Ca	16.3	7.9	16.3
Ti	0.13	0.052	0.041
Cr	7.38	2.84	8.65
Mn	2.82	2.14	3.03
Fe	16.3	23	31.8
Ni	1.94	0.89	3.23
Cu	0.45	0.29	0.32
Zn	5.59	25.4	2.56
Mo	0.3	0.025	1.26
Hg	< 0.005	< 0.005	< 0.005
Pb	0.63	0.73	0.24
C	2.55	0.34	0.36
S	0.38	0.3	0.06
SiO_2	10.2	4.78	7.76
Cl	0.38	1.86	< 0.1
F	0.51	0.21	1.32

Table 2: Received refractories and their main constituents and porosity of the material

	Constituent (wt%)					
	MgO	Al_2O_3	Cr_2O_3	SiO_2	Fe_2O_3	Porosity (vol%)
Radex OX6	59.5	6.0	19.0	0.5	13.5	17.0
Radex S	97.0	0.1	0.0	0.6	0.2	15.0
Resistal RK30	0.0	64.0	28.0	2.1	0.0	15.0
Duritel E90	0.0	89.0	0.0	10.0	0.1	15.5

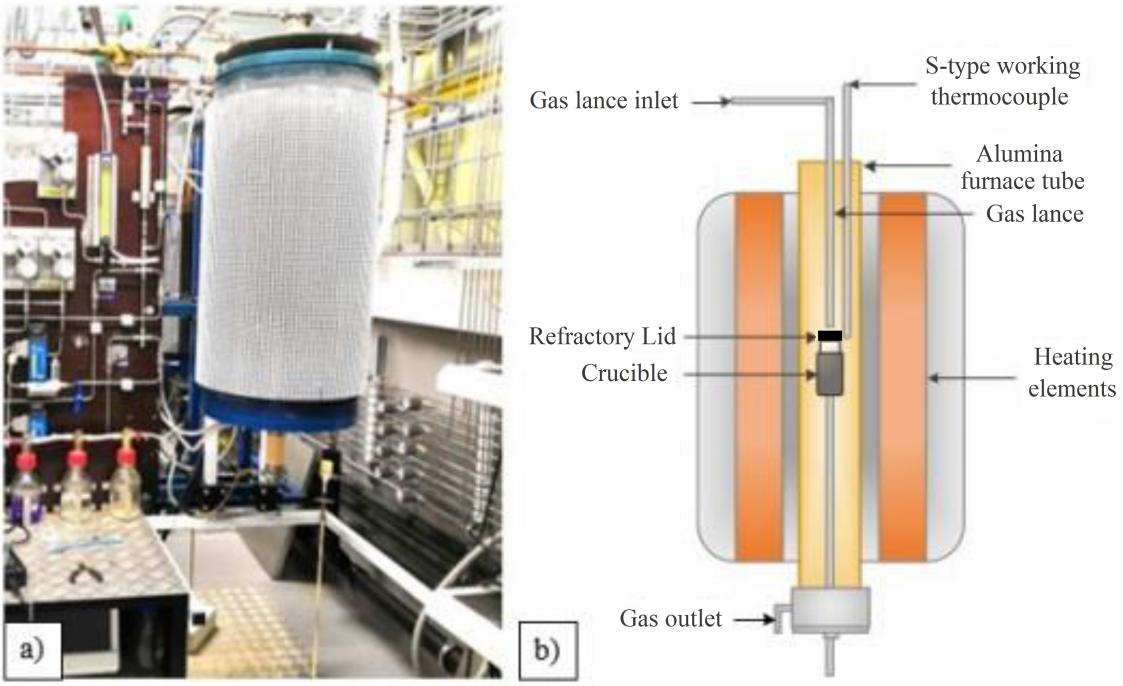

Figure 21: Picture of the furnace used in the experiments (A) and a schematic cross sectional image of the furnace during refractory - dust interaction experiments (B). (Rinne 2019)

3.3 Experimental procedure

The melting behaviour experiments were conducted with one sample per experiment under argon atmosphere. In addition, two experiments were conducted under reducing atmosphere (90 vol-% CO + 10 vol-% CO_2) used to simulate real process conditions. The gas flows used in the experiments were 300 ml/min. For experiments under inert atmosphere this was 300 ml/min of argon and for experiments under reducing atmosphere this was 270 ml/min CO and 30 ml/min CO_2.

When starting an experiment, first the sample was secured in a platinum crucible hanging below the furnace. The sample was then lifted to the cold zone of the furnace. With the sample hanging inside, the furnace was sealed and purged for 20 minutes with the gas flow corresponding to the gas flow used during the experiment. The sample was then lifted to the hot zone of the furnace and held there for the duration of the experiment.

The first experimental set consisted of experiments at 800 °C and 1200 °C for 1, 2, 4 and 8 hours to determine the effect of the holding time and was conducted using VKU2 dust. In the first experimental set it was determined that the melting behaviour experiments could be conducted with a two hour holding time. It was also found that to achieve melt formation the temperature should be increased and, thus, melting behaviour experiments were conducted from 1200 °C to 1300 °C. After the experimental time, the sample was quenched in ice water to capture the state of the sample at the end of the heating time.

The refractory - dust interaction experiments were conducted by loading the alumina crucible with 2.5 g of synthetic dust and placing the crucible in the molybdenum crucible. The refractory lid was then placed on top of the alumina crucible. The molybdenum crucible was then inserted into the furnace tube and lifted to the hot zone. The furnace tube was then placed under a reducing atmosphere (90 vol-% CO + 10 vol-% CO_2) and a heating program was started that would heat the furnace to 1300 °C, keep it there for 6 hours and then cool the furnace back to room temperature. The heating and cooling rate of the furnace was 4 °C/minute. After the furnace had cooled down the gas flow to the furnace was stopped and the sample was removed.

3.4 Sample characterization

The microstructures of the samples were analyzed using a Mira3 SEM (Scanning Electron Microscope, Tescan, Brno, Czech Republic) and the elemental compositions of the samples were determined with an UltraDry Silicon Drift Energy Dispersive Spectrometer (EDS, Thermo Fisher Scientific, USA). The analysis parameters used by the SEM-EDS can be found in Table 3.

3.4.1 Sample preparation

In the melting behaviour experiments, the quenched sample was first dried using ethanol, the ethanol was then evaporated using warm dry air. After drying the sample was left overnight in a desiccator for further drying. The dried sample was then cast

Table 3: SEM-EDS analysis parameters

Parameter	Value
SEM	
Acceleration voltage	15 kV
Spot size	470
Electron emission current	80 µA
Analysis time	15 s ± 30%
EDS standards	
Oxygen	K peak, quartz
Fluorine	K peak, flourite
Sodium	K peak, tugtupite
Magnesium	K peak, magnesium
Aluminium	K peak, aluminium
Silicon	K peak, quartz
Phosphorus	K peak, apatite
Sulphur	K peak, marcasite
Chlorine	K peak, tugtupite
Potassium	K peak, sanidine
Calcium	K peak, anhydrite
Chromium	K peak, chromite
Manganese	K peak, manganese
Iron	K peak, hematite
Nickel	K peak, nickel
Copper	L peak, copper
Zinc	L peak, zinc
Titanium	K peak rutite

into an epoxy resin, and the air bubbles were removed by vacuum degassing using a vacuum pump. The samples were then prepared for the SEM-EDS by grinding and polishing the cast pellet until a flat surface within the pellet was achieved. This flat surface was then carbon coated. The goal of this preparation sequence is to produce a flat, electrically conductive surface for the SEM-EDS analysis.

In the refractory-dust experiments, the refractory lid was broken into smaller parts of which a suitable part was chosen to be mounted in epoxy resin. The refractory, mounted in epoxy resin, was then ground without the use of water and not polished as a protective measurement against dissolving compounds from the refractory. After the experiments dust was collected at the bottom of the crucible and at the bottom of the furnace tube. Both dusts were mounted in their own respective epoxy resin and subsequently ground in similar fashion as the refractory.

3.4.2 SEM-EDS analysis and image analysis

The microstructure and phase compositions were studied by SEM-EDS. The EDS analyses were done by using standards, which are listed in Table 3. For each sample, fifteen pictures were taken of different areas of the sample to get a representative depiction of the sample surface. These pictures were taken with the same brightness, contrast, magnification and distance from the sample in an attempt to keep them comparable. The visible parts of the sample that were situated on a different height level were cut out. An example of this can be seen in Figure 22. The reason for this was that the image analyses were done according to the grey scales of the phases. Parts situated lower than the rest of the surface could have a slightly distorted grey tint and could therefore be measured as a different phase. These pictures were subsequently analysed using the Image Pro Plus 6.0 software to determine the surface areas of the different phases. This was averaged over fifteen pictures and used as the amount of a phase in the sample after the experiment. With the EDS the compositions of the different phases were measured on a few different points, these results were then averaged to estimate a true composition of each phase.

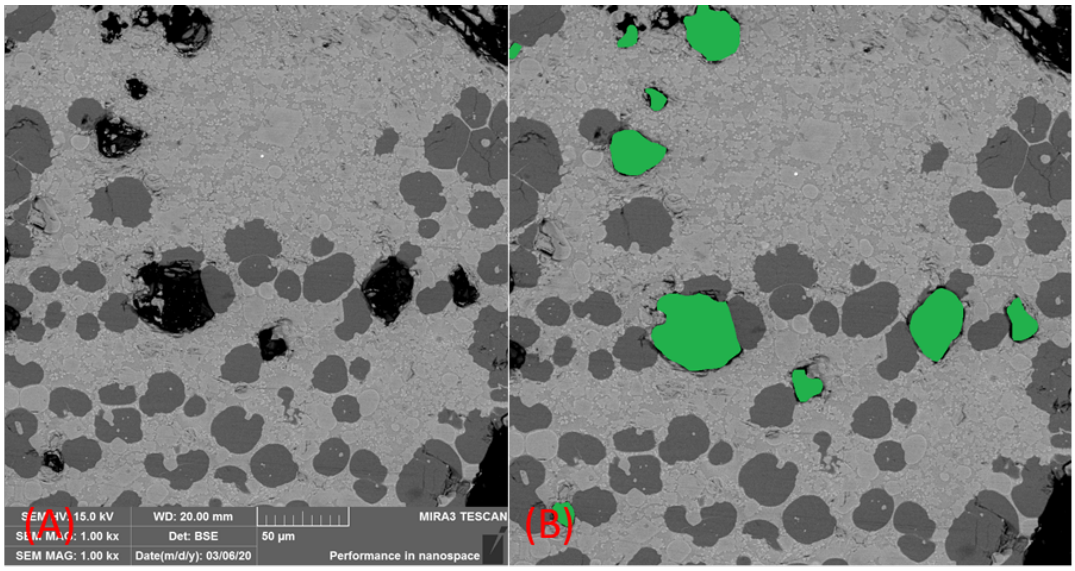

Figure 22: SEM image before (A) and after (B) cutting away parts on a different plane.

4 Results and discussion

4.1 Melting behaviour

The goal of the melting behaviour experiments was to study how the different types of dusts would react during heating and to determine how much molten phase is formed at certain temperatures and the behaviour of alkalis and halogens at these temperatures. ORC supplied the chemical compositions of the dusts as well as the dilatometer curves of the dusts. The chemical compositions of the dusts can be seen in Table 1 and the curves can be seen in Figures 23, 24 and 25.

4.1.1 800 °C to 1200 °C region

From the dilatometer curves it was estimated that some melting action occurred in the 800 °C to 1200 °C region. Therefore, experiments were conducted at 800 °C and 1200 °C to determine how much of a molten phase would form when increasing the temperature to 1200 °C. These experiments were also conducted for 1, 2, 4 and 8 hours to determine the effect of time on the experiments. The series of SEM pictures can be seen in Figures 26 and 27. Here it can be seen that no melting happens at 1200 °C and that there is only some sintering. Furthermore, it can be seen that due to the small sample size the heating time did not impact the melting or sintering.

From these results it was decided to conduct further melting behaviour experiments in the 1200 °C to 1400 °C region.

4.1.2 1200 °C to 1400 °C region

These experiments were conducted with an experimental time of two hours since it was found that longer experimental times had not influenced previous experiments. These experiments were also only conducted up to a temperature of 1400 °C for the VKU2 dust, since it was the first dust used. The reason for this was that experiments conducted at 1350 °C and 1400 °C had such a high fraction of the molten phase that the pellets fused to the crucible and reusing the crucible was therefore not possible. Therefore, experiments with VKU1 and AOD were only conducted up to 1300 °C. In the experiments involving AOD dust, the pellet had fused with the platinum crucible in several locations through thin strands of material. Removal of the pellet after these experiments was still possible.

The SEM pictures of these samples can be seen in Figures 28, 29 and 30. As can be seen in these images that for the VKU2 dust at 1250 °C the dust starts to form a molten phase and at 1400 °C a large fraction of the dust was in a molten phase. The VKU1 and AOD dust both start forming a liquid phase at a lower temperature than the VKU2 dust. A molten metal fraction was identified for the AOD dust at 1200 °C.

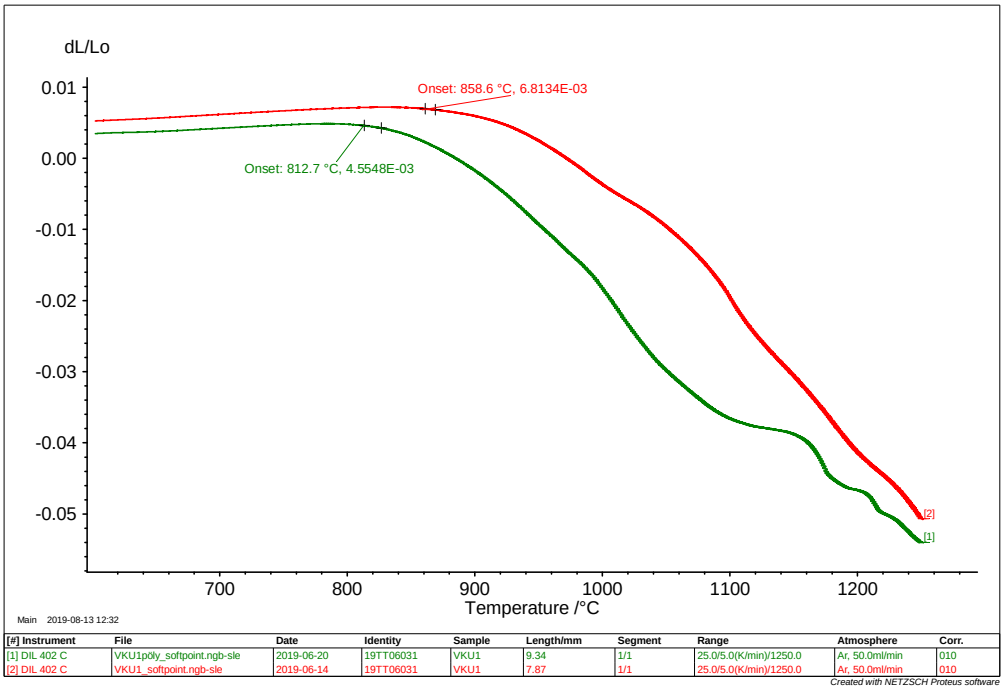

[#] Instrument	File	Date	Identity	Sample	Length/mm	Segment	Range	Atmosphere	Corr.
[1] DIL 402 C	VKU1póly_softpoint.ngb-sle	2019-06-20	19TT06031	VKU1	9.34	1/1	25.0/5.0(K/min)/1250.0	Ar, 50.0ml/min	010
[2] DIL 402 C	VKU1_softpoint.ngb-sle	2019-06-14	19TT06031	VKU1	7.87	1/1	25.0/5.0(K/min)/1250.0	Ar, 50.0ml/min	010

Created with NETZSCH Proteus software

Figure 23: Dilatometer curve of VKU1 dust as measured by ORC.

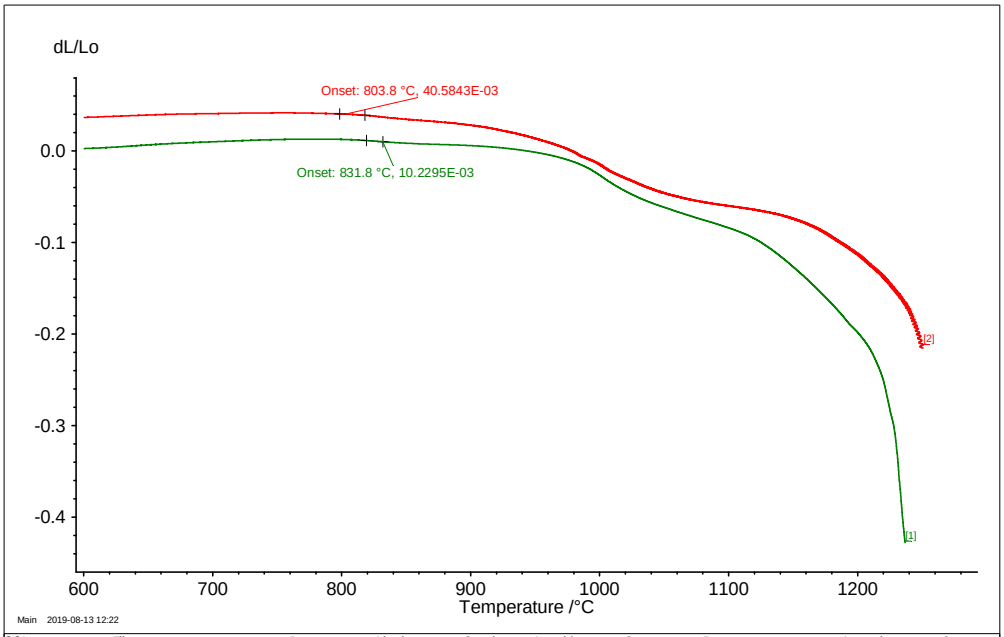

[#] Instrument	File	Date	Identity	Sample	Length/mm	Segment	Range	Atmosphere	Corr.
[1] DIL 402 C	VKU2póly_softpoint___.ngb-sle	2019-08-07	19TT06032	VKU2	4.06	1/1	25.0/5.0(K/min)/1250.0	Ar, 50.0ml/min	010
[2] DIL 402 C	VKU2póly_softpoint_.ngb-sle	2019-06-27	19TT06032	VKU2	6.46	1/1	25.0/5.0(K/min)/1250.0	Ar, 50.0ml/min	010

Created with NETZSCH Proteus software

Figure 24: Dilatometer curve of VKU2 dust as measured by ORC.

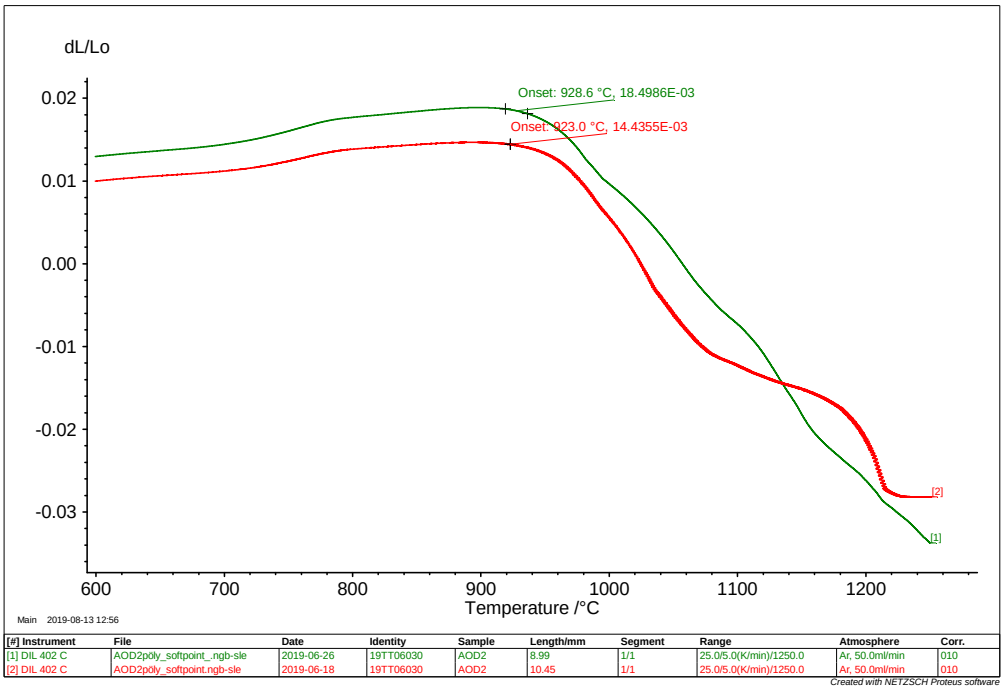

Figure 25: Dilatometer curve of AOD dust as measured by ORC.

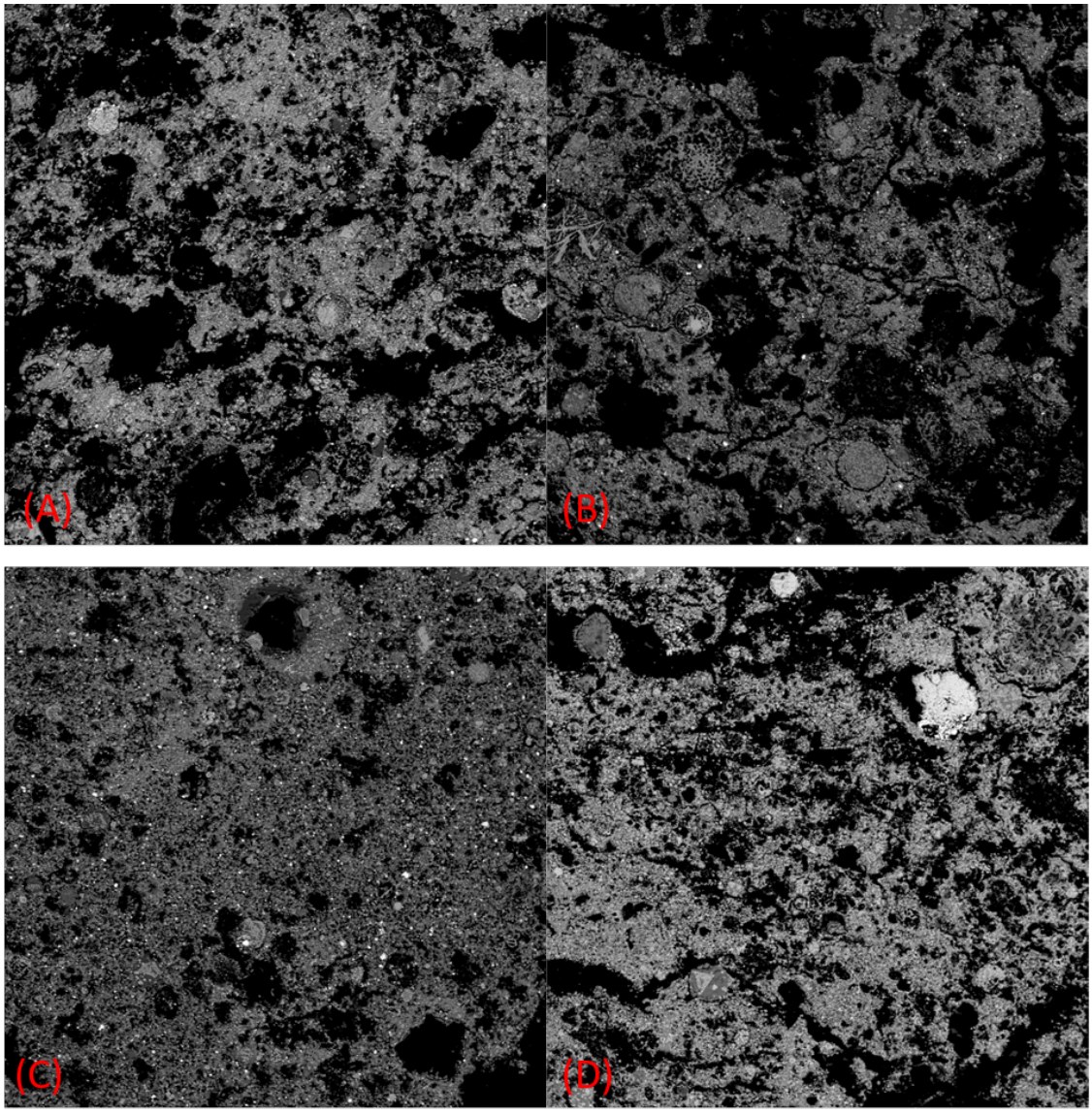

Figure 26: SEM image of VKU2 dust after heating at 800 °C for (A) 1 hour, (B) 2 hours, (C) 4 hours and (D) 8 hours.

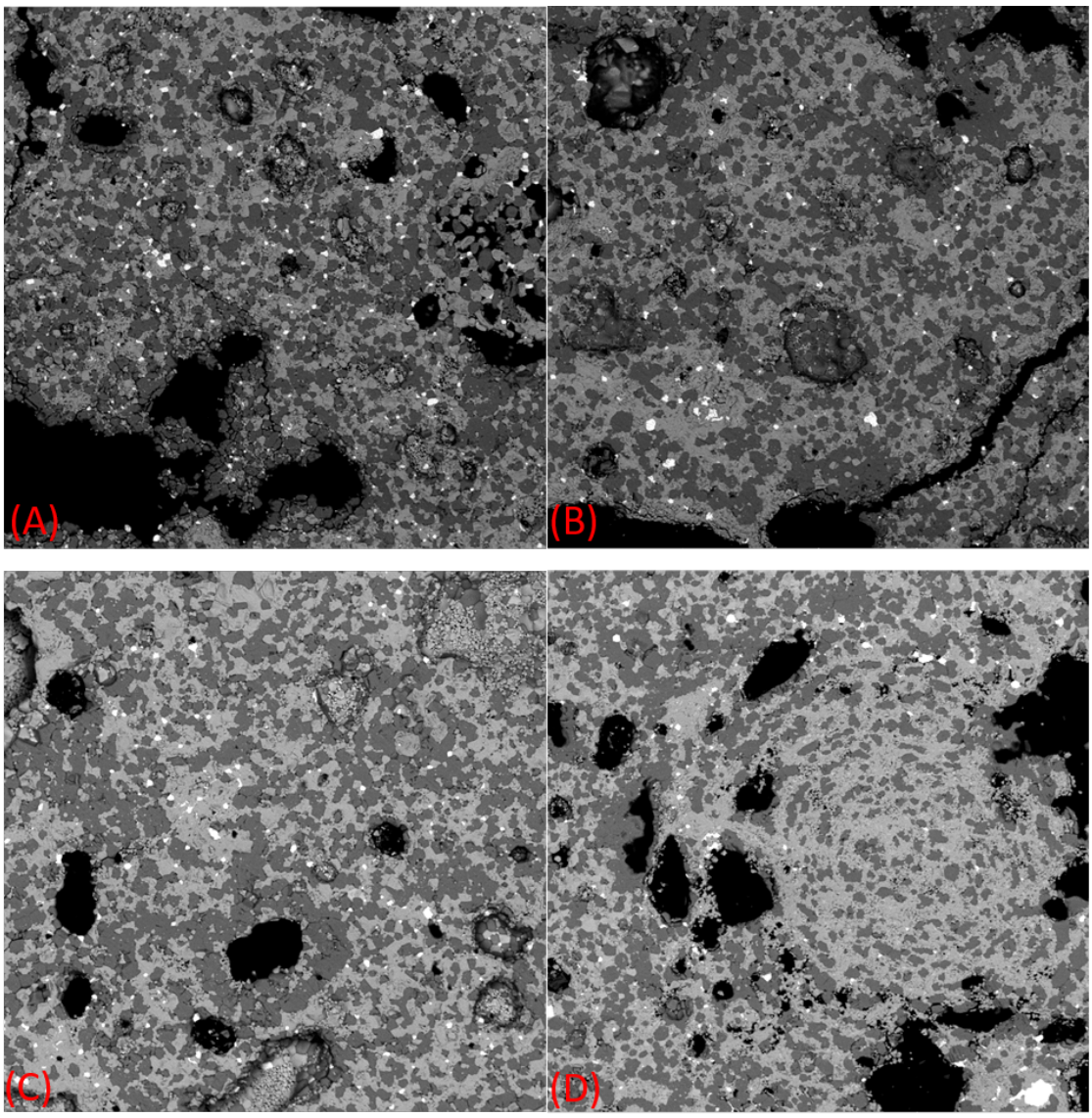

Figure 27: SEM image of VKU2 dust after heating at 1200 °C for (A) 1 hour, (B) 2 hours, (C) 4 hours and (D) 8 hours.

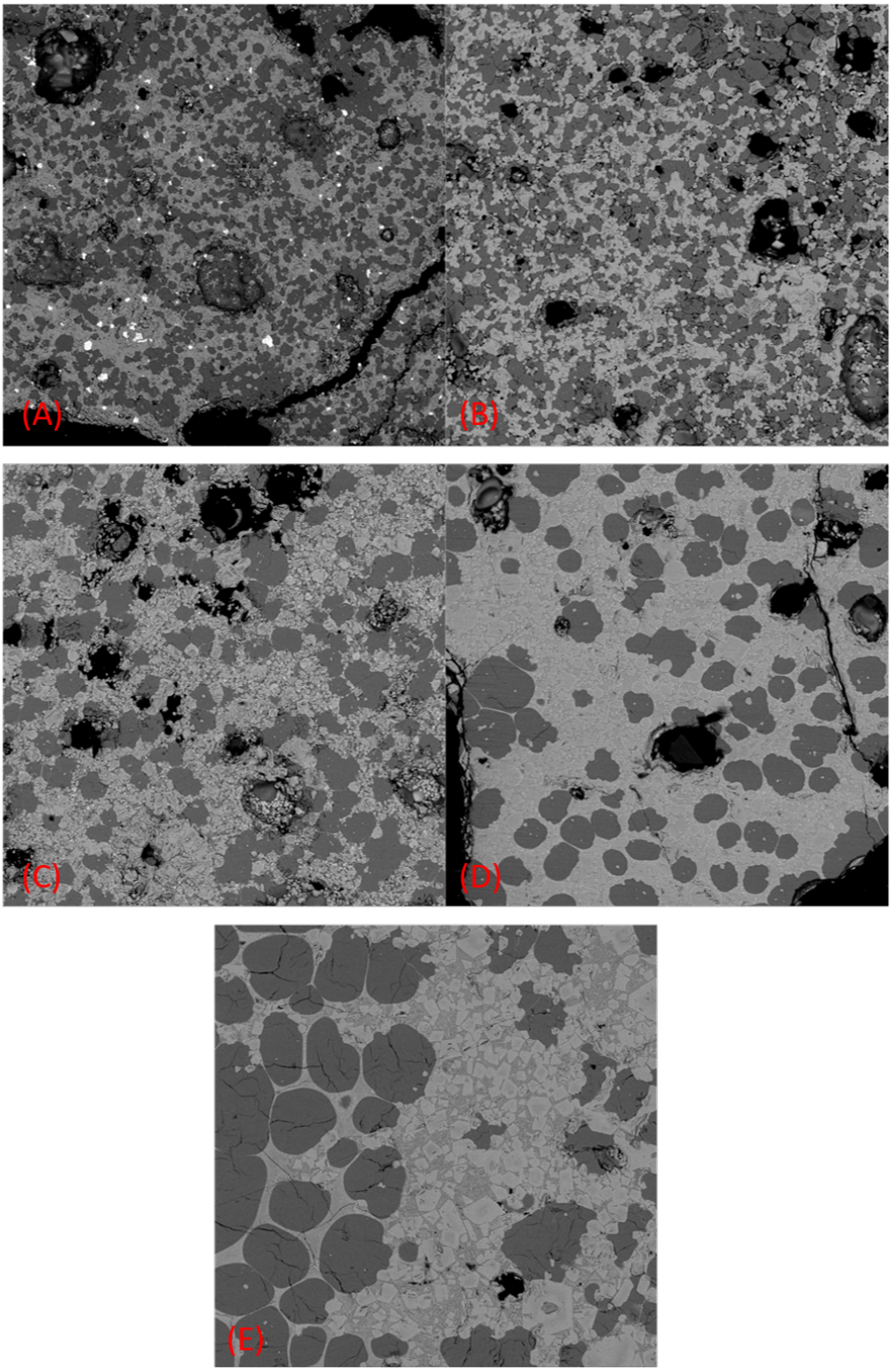

Figure 28: SEM image of VKU2 dust after heating for 2 hours at (A) 1200 °C, (B) 1250 °C, (C) 1300 °C, (D) 1350 °C and (E) 1400 °C.

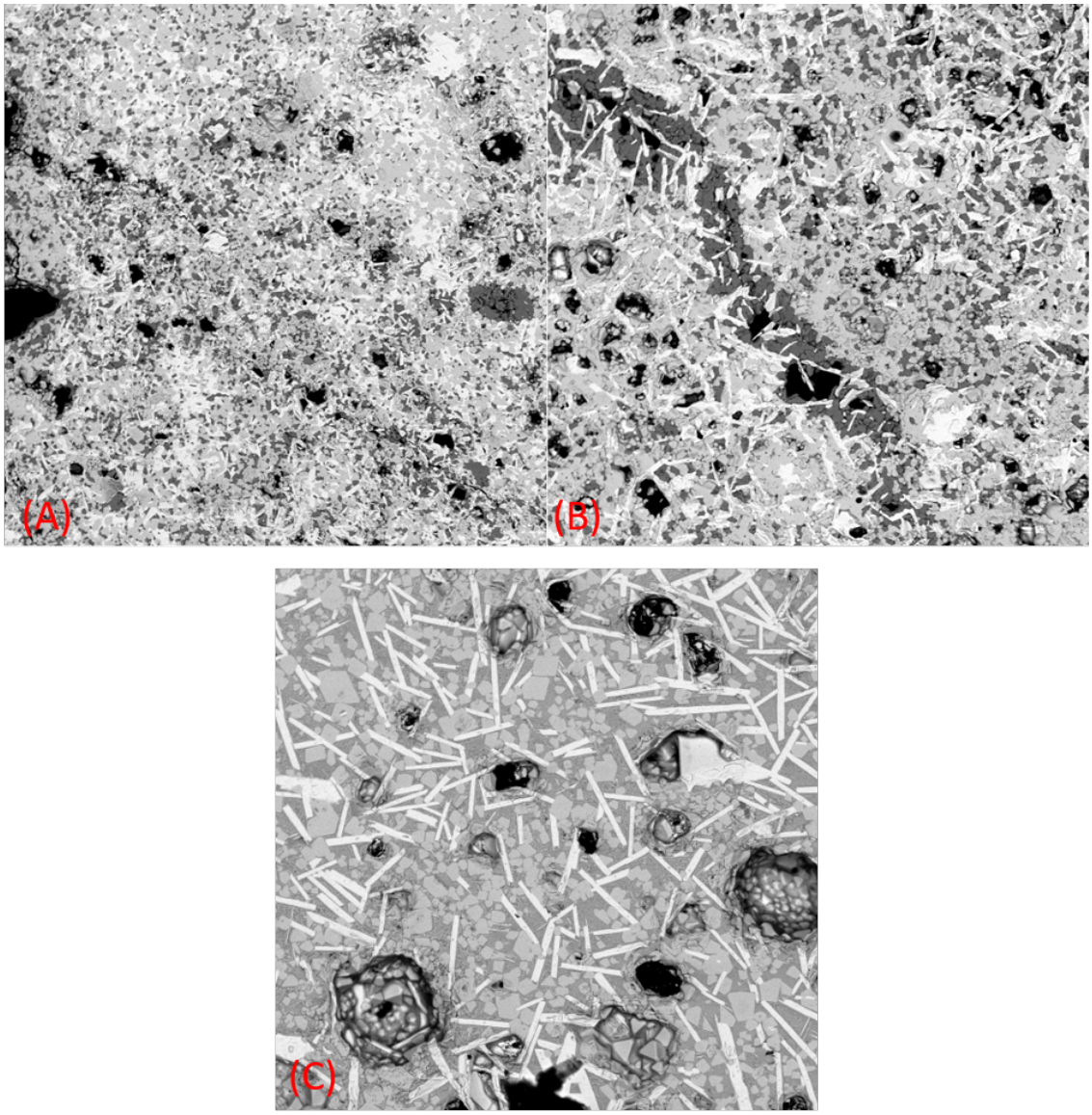

Figure 29: SEM image of VKU1 dust after heating for 2 hours at (A) 1200 °C, (B) 1250 °C and (C) 1300 °C.

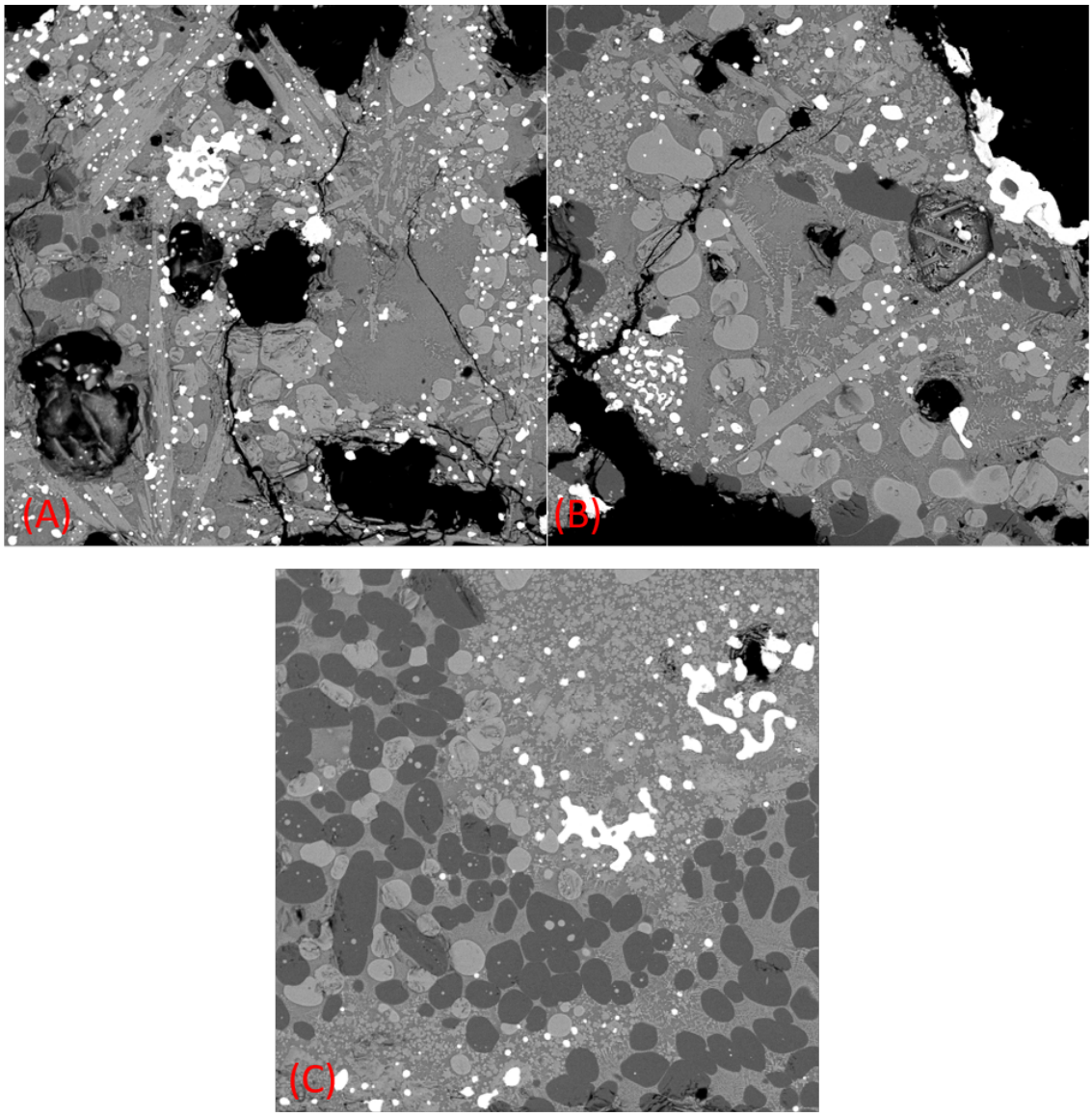

Figure 30: SEM image of AOD dust after heating for 2 hours at (A) 1200 °C, (B) 1250 °C and (C) 1300 °C.

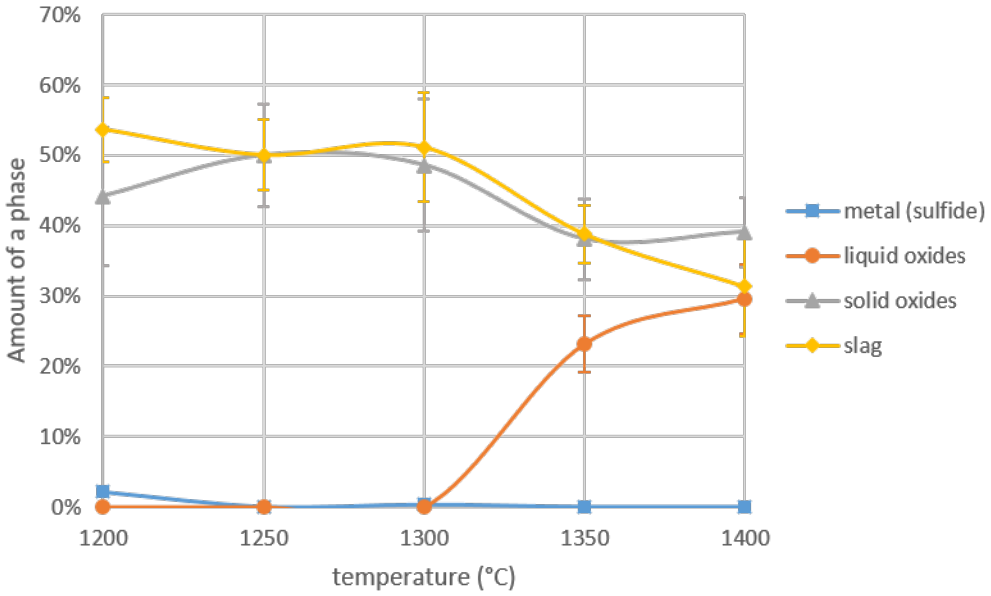

Figure 31: The amount of a metal-sulfide, liquid metal oxide, solid metal oxide and slag phase in the VKU2 dust in the experimental temperature range

4.1.3 Image analysis

In Figure 31 can be seen that four different phases formed during the heating of the VKU2 dust. The first phase is a reflective metallic layer with at lower temperatures a sulfur content of 20 mol%, at higher temperatures this phase is either non existing or existing in such small amounts that it was not possible to get an accurate measurement. The second and third phases are metal oxide phases. At lower temperatures the metal oxide phase solely exist as a solid phase, at higher temperatures also a liquid phase starts to form. The liquid metal oxide phase already exists at 1300 °C but was too mixed with, and similar in colour to, the solid metal oxide phase that determining the amount was impossible and is included in the solid phase. The largest components of the solid and liquid metal oxide phases are presented in Table 4. The last phase is the slag phase. The slag kept a 2:1 calcium to silicon mole ratio over the whole temperature range.

In Figure 32 a phase with similar reflective properties as the metallic phase in VKU2 was also found in the VKU1 dust. After analyses with the SEM-EDS it was found that this phase contains almost 50% oxygen. Thus, it was not a metallic phase and had similar oxygen content as the light grey metal oxide phases observed in both VKU2 and VKU1 dusts. Further, the solid and liquid metal oxide phases and the slag phase compositions were similar to those in the VKU2 dust. One thing of note is that at 1300 °C there was no more dark slag phase. The main constituents of the metal phases can be seen in Table 5.

In Figure 33 the fractions of the four phases in the AOD dust can be seen, the

Table 4: Mole fraction of elements in the solid and liquid metal oxide phases in VKU2 dust after heating

	Temperature						
	Solid					Liquid	
	1200 °C	1250 °C	1300 °C	1350 °C	1400 °C	1350 °C	1400 °C
Fe	0.199	0.124	0.159	0.127	0.143	0.166	0.117
Cr	0.121	0.131	0.075	0.173	0.141	—	—
Mg	0.100	0.075	0.134	0.080	0.097	—	—
Mn	0.035	0.029	0.040	0.033	0.032	0.023	0.020
Ni	0.020	0.015	0.034	0.014	0.016	—	—
Ca	—	—	—	—	—	0.220	0.196
Si	—	—	—	—	—	0.065	0.070

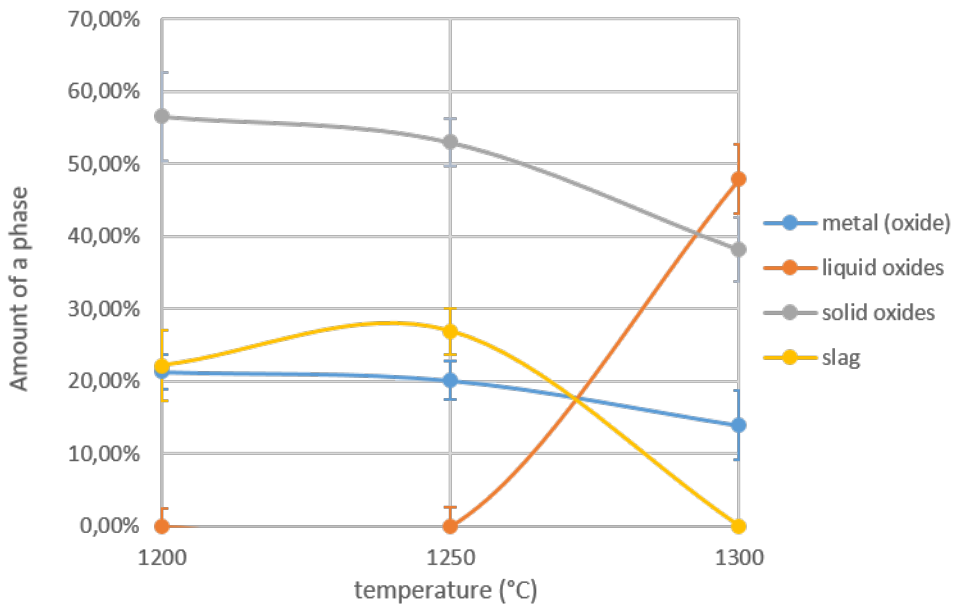

Figure 32: The amount of a metal, liquid metal oxide, solid metal oxide and slag phase in the VKU1 dust in the experimental temperature range

Table 5: Mole fractions of elements in the solid, liquid and reflective metal oxide phases in VKU1 dust after heating.

	Temperature						
	Solid			Liquid	Reflective		
	1200 °C	1250 °C	1300 °C	1300 °C	1200 °C	1250 °C	1300 °C
Fe	0.242	0.250	0.223	0.099	0.092	0.095	0.104
Cr	0.032	0.044	0.053	—	0.003	0.003	0.003
Mg	0.020	0.020	0.024	0.005	0.018	0.017	0.028
Mn	0.023	0.023	0.022	0.010	0.014	0.014	0.017
Zn	0.102	0.133	0.100	0.073	0.310	0.348	0.305
Ni	0.010	0.010	0.009	—	—	—	—
Ca	0.015	0.007	0.007	0.163	0.030	0.020	0.016
Si	—	—	—	0.074	—	—	—

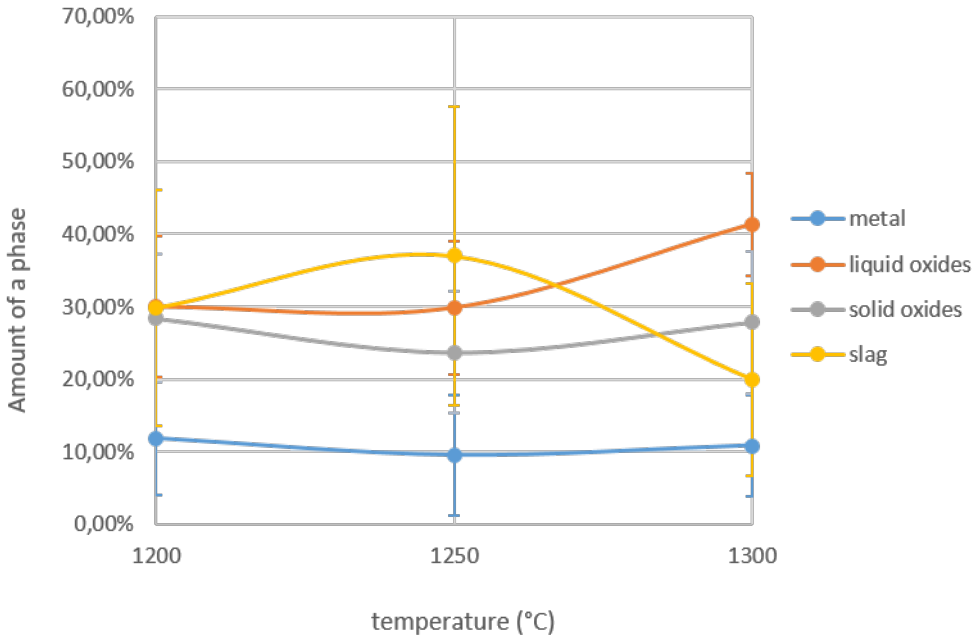

Figure 33: The amount of a metal, liquid metal oxide, solid metal oxide and slag phase in the AOD dust in the experimental temperature range.

Table 6: Mole fraction of elements in the solid, liquid and reflective metal oxide phases in AOD dust after heating.

	Temperature								
	Solid			Liquid			Reflective		
	1200 °C	1250 °C	1300 °C	1200 °C	1250 °C	1300 °C	1200 °C	1250 °C	1300 °C
Fe	0.118	0.180	0.082	0.040	0.052	0.078	0.681	0.731	0.638
Cr	0.153	0.065	0.245	—	—	—	0.009	0.005	0.006
Mg	0.125	0.119	0.072	—	—	—	—	—	—
Mn	0.049	0.096	0.040	0.002	0.010	0.014	—	—	—
Al	0.003	0.002	0.038	0.009	0.002	0.062	—	—	—
Ca	—	—	—	0.290	0.299	0.209	0.004	0.003	0.003
Si	—	—	—	0.068	0.057	0.058	—	—	—
Ni	—	—	—	—	—	—	0.283	0.230	0.298

first thing to note here is that at 1200 °C a liquid phase could be distinguished. Furthermore, also in these samples a reflective metal phase existed. This phase was a metallic phase which contained in contrast to the other dusts basically no sulfur or oxygen. The main constituents of the metal phases can be seen in Table 6.

4.2 Alkali and halogen behaviour

In this section, the phases in which the alkali metals and halogens were observed will be discussed.

4.2.1 Fluorine

Fluorine has been located in the VKU2 dust in the phase consisting of solid $(Mg,Ni)(Cr,Fe,Mn)_2O_4$ spinel crystals over the whole temperature range of 1200 °C through 1400 °C. Further, fluorine has been located in a phase high in calcium, sulfur and oxygen at 1250 °C.

In the VKU1 dust, fluorine was found in a solid spinel phase consisting of $(Zn,Ni,Mg)(Cr,Fe,Mn)_2O_4$ over the temperature range of 1200 °C up to 1300 °C. The amount of fluorine at 1300 °C had decreased and was almost completely absent from the sample.

In the AOD dust fluorine was found throughout the sample at 1200 °C. In a part of the Fe, Ni metallic phase, which had been contaminated by the platinum crucible, 7 mol% of fluorine was found. Fluorine was also found in a solid spinel phase consisting mainly of $(Mg,Ca)(Cr,Fe)_2O_4$. Finally, it was also found in a liquid phase mainly consisting of calcium, silicon and iron oxides, where the concentrations were up to 20 mol%.

The liquid phase with high concentrations of fluorine existed also at 1250 °C and at 1300 °C. However, the concentrations of fluorine in the liquid phase had decreased to less than 5 mol% at 1300 °C. Low concentrations of fluorine maintained in the metallic phase at the higher temperatures. The solid spinel had decreased concentrations of fluorine at 1250 °C and was free of fluorine at 1300 °C.

4.2.2 Sodium

Sodium was only found in trace amounts in the sample of the VKU2 dust. Sodium was identified in the slag phase in the whole temperature range from 1200 °C to 1400 °C. At 1250 °C sodium was found in the phase consisting of calcium, sulfur and oxygen where fluorine was detected. At 1350 °C sodium was found in the metallic and the liquid metal oxide phase.

In the VKU1 dust sodium was found in low concentrations throughout all temperatures in the slag phase. Some of the investigated points of the solid oxide phase show concentrations of 2-3 mol% sodium. At 1300 °C the liquid oxide phase shows sodium throughout the whole liquid phase. The concentration in the liquid phase is about half the concentration than what was found in the solid oxide phase.

Sodium was not found in sufficient quantities in the AOD dust to make any meaningful observations about the behaviour of sodium. This can be explained by the starting concentration of sodium, which was approximately one sixth of the concentrations in the VKU dusts.

4.2.3 Potassium

Potassium was only found in trace amounts in VKU2 slag phase and some spot analyses in the VKU1 slag phase. Other phases in the VKU dusts showed no potassium. The AOD dust showed no potassium in any phase, which is expected with the very low concentration of potassium in the original sample.

4.2.4 Chlorine

Chlorine was not found in the samples after heating, this is in accordance with expectations about chlorine behaviour at high temperatures.

4.3 Refractory - Dust interaction

The goal of the refractory - dust interaction experiments was to study the effect of a synthetic dust on four types of refractories. In this section the resulting dust fractions and the refractory will be examined.

4.3.1 Dust fractions

After the experiments, dust was found in the crucible and on the bottom of the furnace tube. For two of the experiments the dust found at the bottom of the furnace and the crucible were mounted in epoxy resin. The dusts were then prepared for analysis using traditional grinding methods without the use of water in an attempt to prevent dissolution of the salts from the dust. The resulting dust compositions can be found in Table 7 next to the composition of the original dust. In this table it can be seen that the dust compositions vary quite a bit. The most expected changes are an increased chloride concentration in the bottom dust, since the chlorine will be in the gas phase at the high temperatures and then solidify around the water cooled bottom.

Table 7: Compositions of the dusts found at the bottom of the furnace (BD) and the dusts found in the crucible (CD) after the experiments compared to the original dust (OD).

	Weight percentage				
	OD	BD1	BD2	CD1	CD2
K	0.402	0.431	0.374	0.374	0.416
Cl	0.091	0.305	0.142	0.106	0.054
F	0.116	0.061	0.231	0.139	0.072

4.4 Effects on the refractory composition and structure

4.4.1 Visual analyses

The interaction between refractory and dust under reducing atmosphere was investigated for four refractories. These refractories were the Radex OX6, Radex S, Resistal RK30 and the Durital E90.

A first observation can be made by visually comparing the tested refractories with the original refractories. These comparison images can be seen in Figures 34, 35, 37 and 38. In the pictures of the *Radex OX6* refractory (Figure 34) can be seen that not much has changed visually to the refractory. The main observations to be made for this refractory post experiment, that it has a slight swollen form and that towards the middle and bottom there is a slight change in colour. Further, towards the right side of the refractory post experiment, it can be seen that the structure is rougher, whereas the middle is smoother. This points towards a reduction in porosity in the sample in the areas affected by the exhaust gas.

In the pictures of the *Radex S* refractory (Figure 35) can be seen that the outer edge has a lighter colour compared to the rest of the sample which is also more similar to the original refractory. This can be more clearly seen in Figure 36, here can be seen that the outer edge has a lighter colour, whereas the inside has a darker discoloration. The shape of the sample seems to be equal or at least very similar to the original shape. The microstructure in the center of the refractory seems to be similar to the microstructure on the edge of the refractory.

In the pictures of the *Resistal RK30* refractory (Figure 37) can be seen that the bottom of the sample has changed from a black to green colour, furthermore it can be seen that the original white grains have been affected and a purple coloured material has formed. The shape and microstructure seem to be similar after the experiments to what it was before the experiments.

In the pictures of the *Durital E90* refractory (Figure 38) can be seen that the sample has expanded in the center of the refractory and that its colour has changed. Three layers can be distinguished. The first layer, starting from the bottom, is a layer with a darker grey layer. This layer is followed by a matte white layer up to about half way through the refractory. The third layer seems like a more glassy white layer in the top half of the refractory. The red colour at the top is unrelated to the experiments and are from a marker. The top was marked with a red marker, so that the top could clearly be distinguished after breaking the sample and mounting it in epoxy resin. The porosity seems less in the bottom half of the sample than in the top half of the sample.

4.4.2 BSE and EDS analyses

Radex OX6 was the first tested refractory, with as main components magnesia and chromite. A picture of the full cross section from the mounted refractory part can be seen in Figure 39. A more detailed panoramic picture of the cross section of this refractory can be found in Figure 40. In the pictures the bottom of the refractory was in contact with the synthetic exhaust gas and the reducing atmosphere came in

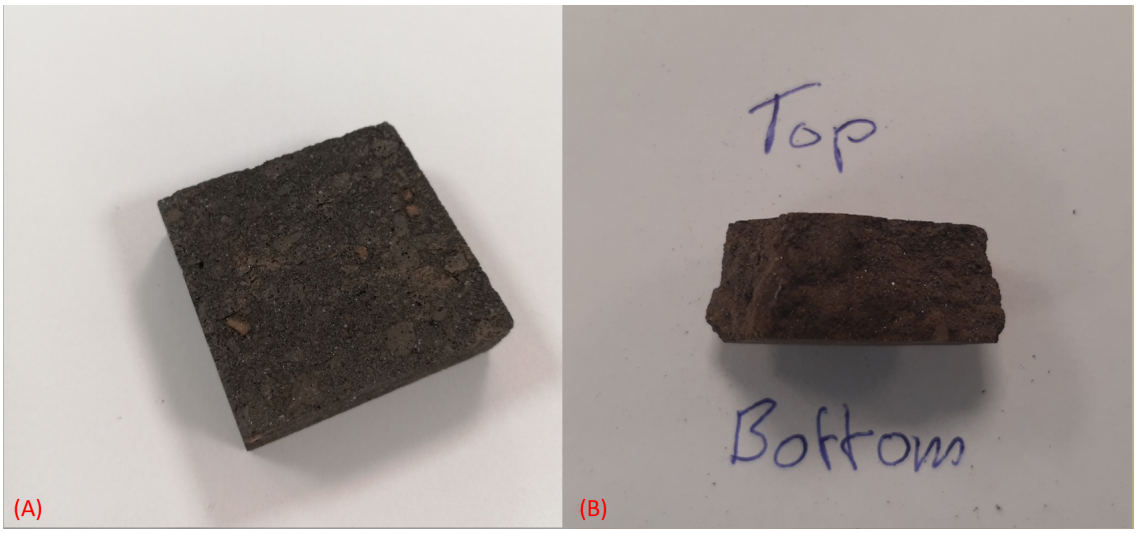

Figure 34: Visual comparison between original Radex OX6 refractory (A) and the Radex OX6 refractory after refractory-dust interaction experiment (B).

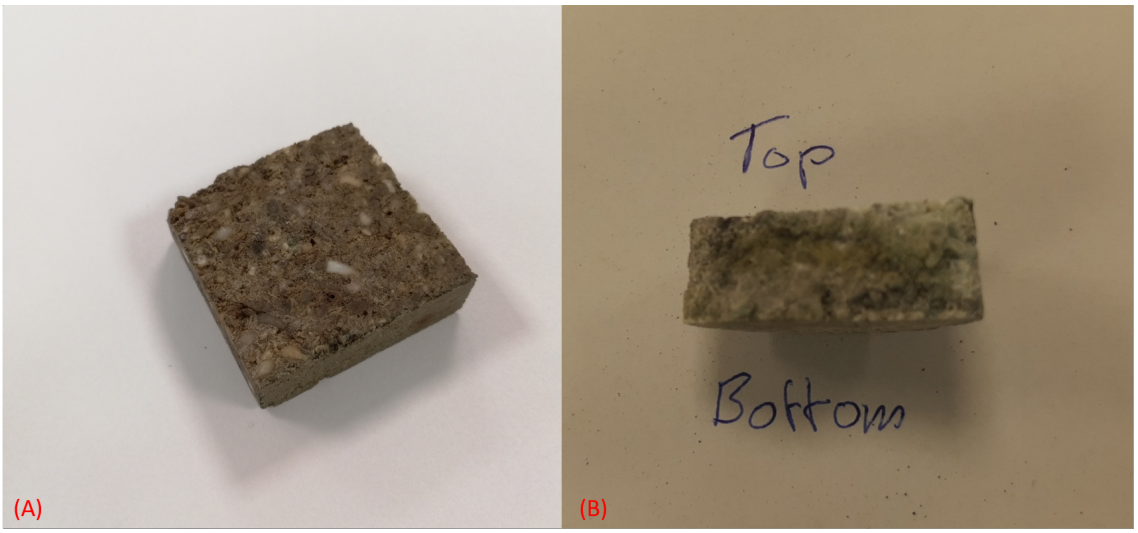

Figure 35: Visual comparison between original Radex S refractory (A) and the Radex S refractory after refractory-dust interaction experiment (B).

Figure 36: Top down view of the Radex S refractory after refractory-dust interaction experiment.

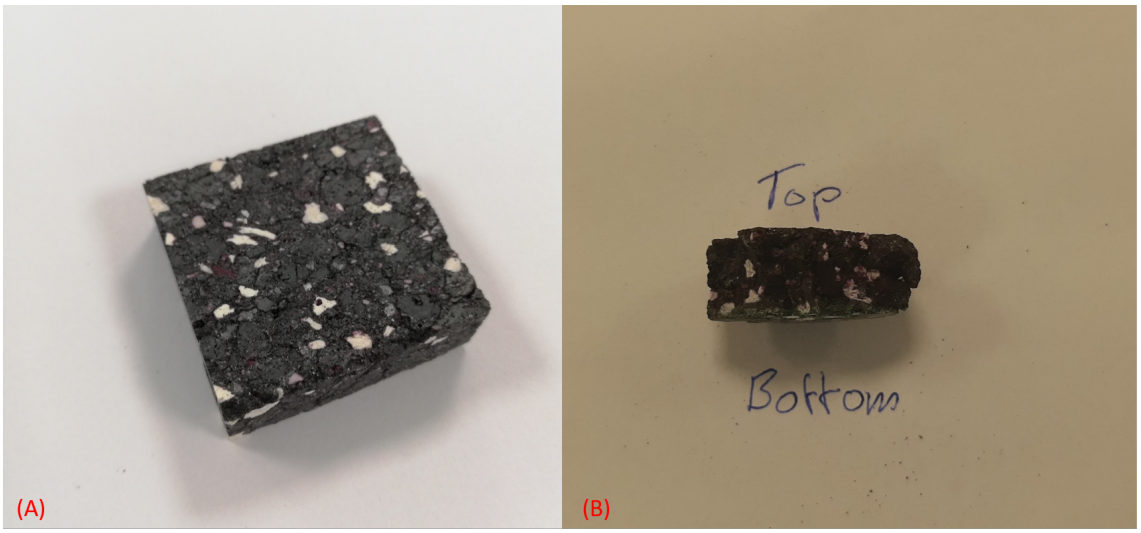

Figure 37: Visual comparison between original Resistal RK30 refractory (A) and the Resistal RK30 refractory after refractory-dust interaction experiment (B).

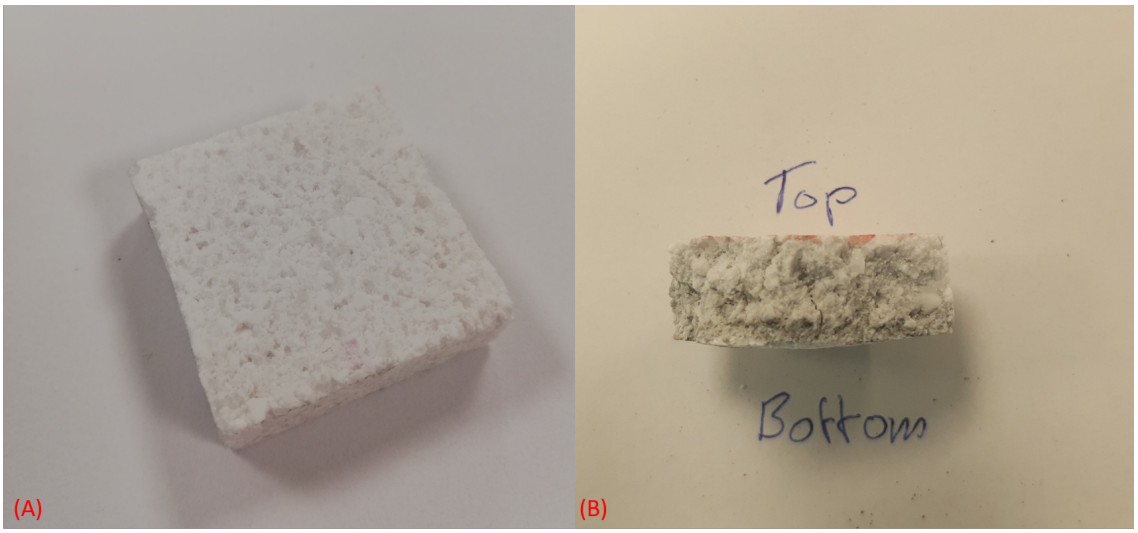

Figure 38: Visual comparison between original Durital E90 refractory (A) and the Durital E90 refractory after refractory-dust interaction experiment (B).

flowing from the top. In the full picture it can also be seen that the bottom left was situated near the center of the crucible and the bottom right part was supporting on the alumina crucible or positioned slightly outside of the alumina crucible. In the panoramic picture can be seen that the refractory has expanded to roughly 105% of the original thickness.

In the structure of the refractory it can be seen that the outer side (right side) and top are more porous than the part of the lid in contact with the synthetic dust gas. The refractory contains large magnesia particles which contain small amounts of iron and chrome in solid solution. A light grey phase can be distinguished within the magnesia grains and also on grain boundaries. This spinel phase has a general composition of $Mg(Cr,Fe,Al)_2O_4$. Potassium can be found in high concentrations in a alumina silica phase containing up to 20 mol% potassium near the bottom up to 3 mm into the sample. At a penetration depth of 5 mm only low concentrations of potassium can be found. Higher penetration depths only show trace amounts of potassium.

Resistal RK30 was the second tested refractory, with as main components chromia and alumina. A picture of the full cross section from the mounted refractory part can be seen in Figure 41. A more detailed panoramic picture of this cross section can be found in Figure 42. The bottom of the pictures was in contact with the synthetic exhaust gas and the reducing atmosphere came in flowing from the top. In the picture of the whole cross section it can be seen that the bottom right corner was positioned in the middle of the crucible and the bottom left corner was positioned on the outside. In the panoramic picture can be seen that the refractory has expanded to roughly 110% of the original thickness.

In the structure it can be seen that the dust - refractory interactions have reduced the porosity up to a depth of 7 mm. The refractory itself consists of alumina grains (darker areas on the SEM image) and alumina - chromia grains (lighter areas on the SEM image). Some small white areas can be distinguished all over the refractory, this is the zirconia with which the refractory is doped to increase its corrosion resistance. The bottom right of the refractory cross section is invested with a heavy element, which formed bubbles in the refractory. This heavy element has been determined to be molybdenum. The only source for the molybdenum can be the molybdenum holding crucible. This does however not explain that the highest amounts of molybdenum were measured in the bottom center of the refractory. This is the furthest location from the holding crucible. The molybdenum bubbles at the interface contain around 23-25 mol% potassium, whereas the alumina phase directly above the molybdenum bubles contain only around 5 mol% potassium. At a penetration depth of approximately 1 mm the large alumina grain has not been affected by potassium but the alumina chromia phase contains around 5 mol% potassium. At a penetration depth of 2 mm, in the area with a high concentration of zirconia flakes, an area with high potassium concentrations was found. The alumina phase situated between the zirconia flakes has a potassium concentration between 9 and 10 mol%. At a depth of 4.5 mm the alumina chromia phase contained around 2 mol% potassium. This was the highest depth at which potassium was ascertained.

Radex S was the third tested refractory, with as main component magnesia. A

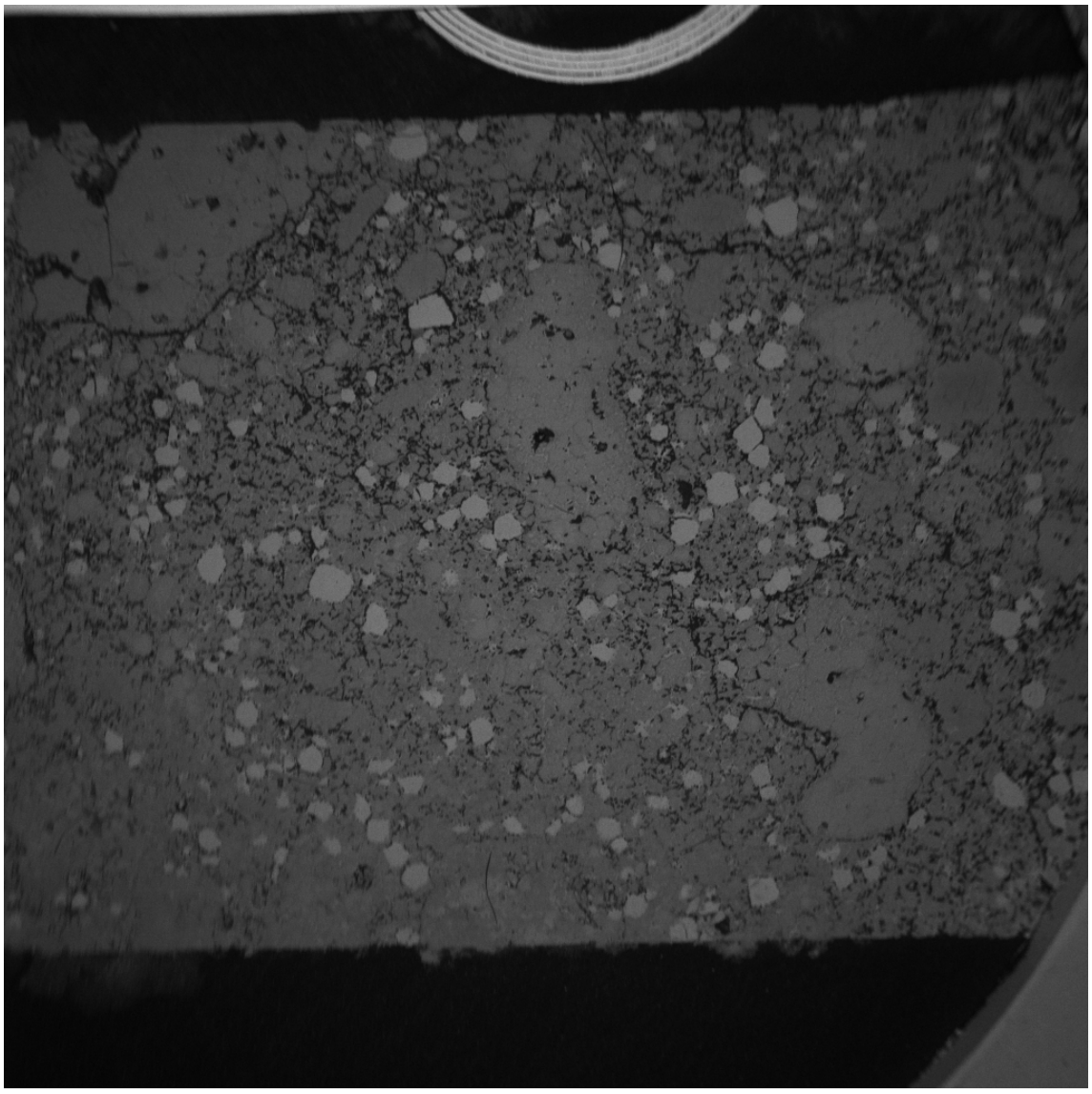

Figure 39: BSE image of cross section of the Radex OX6 refractory

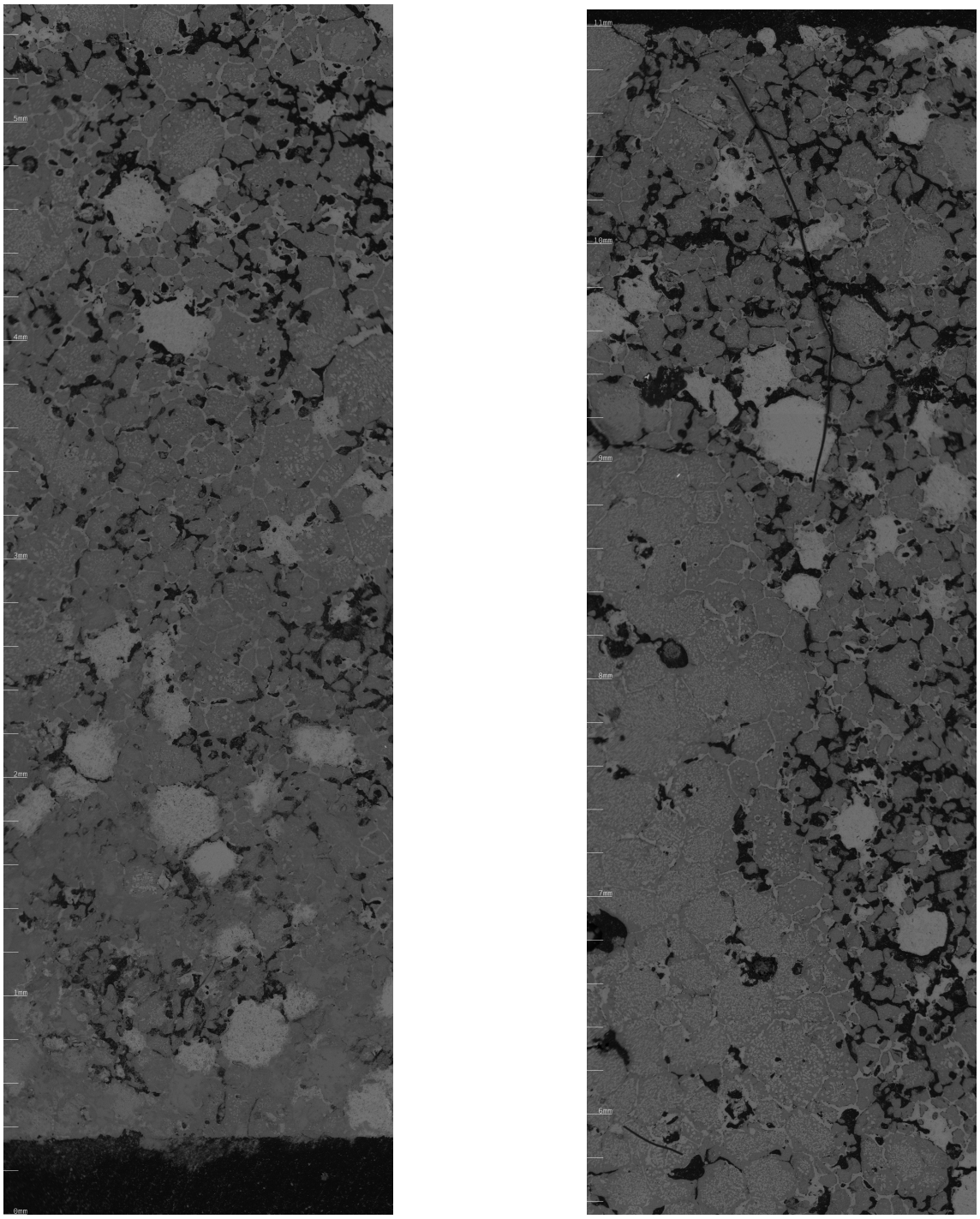

Figure 40: Panoramic BSE image of a part of the cross section of the Radex OX6 refractory. The bottom of the refractory was in contact with the synthetic exhaust gas and the top with the reducing atmosphere.

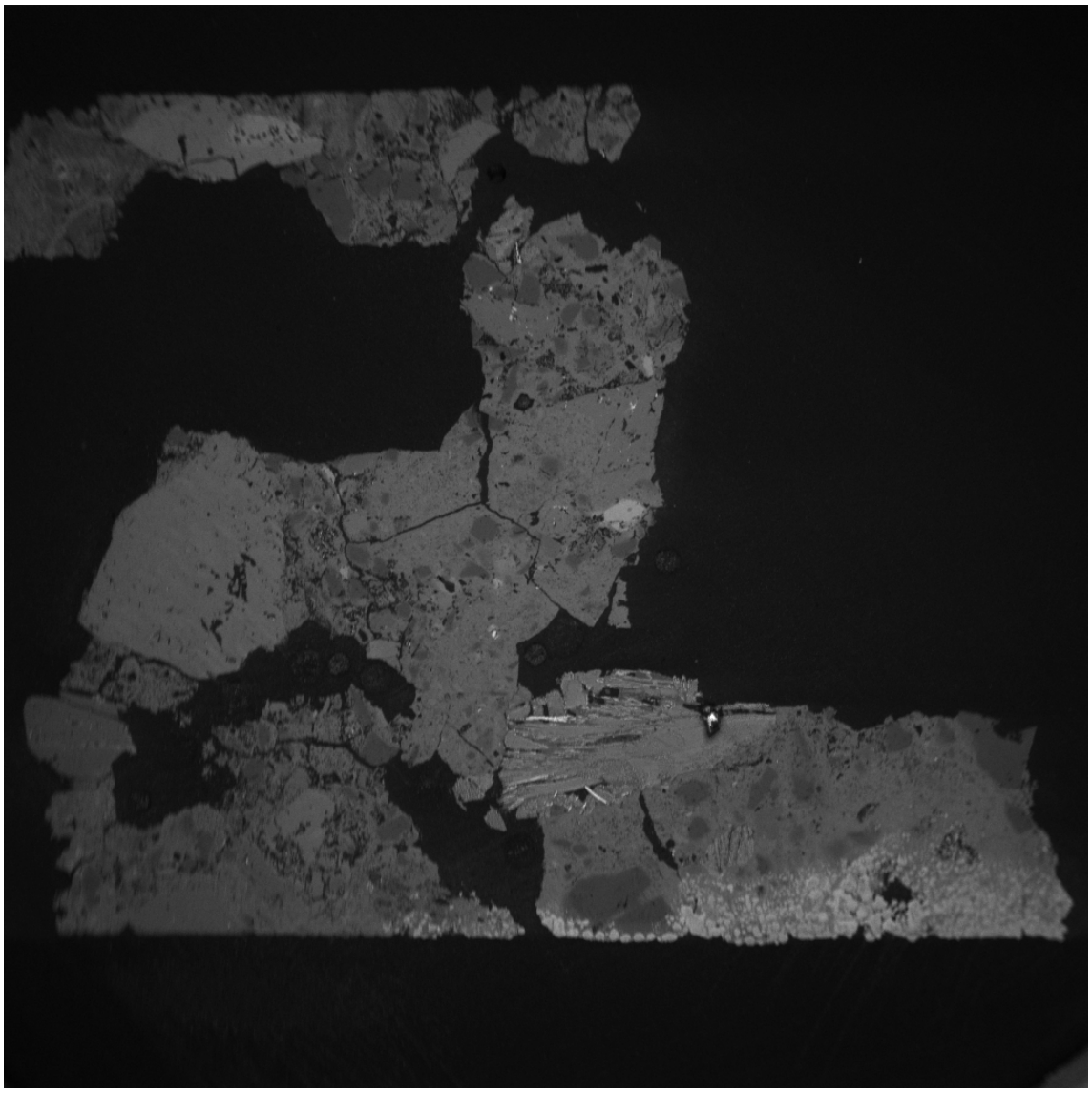

Figure 41: BSE image of cross section of the Resistal RK30 refractory.

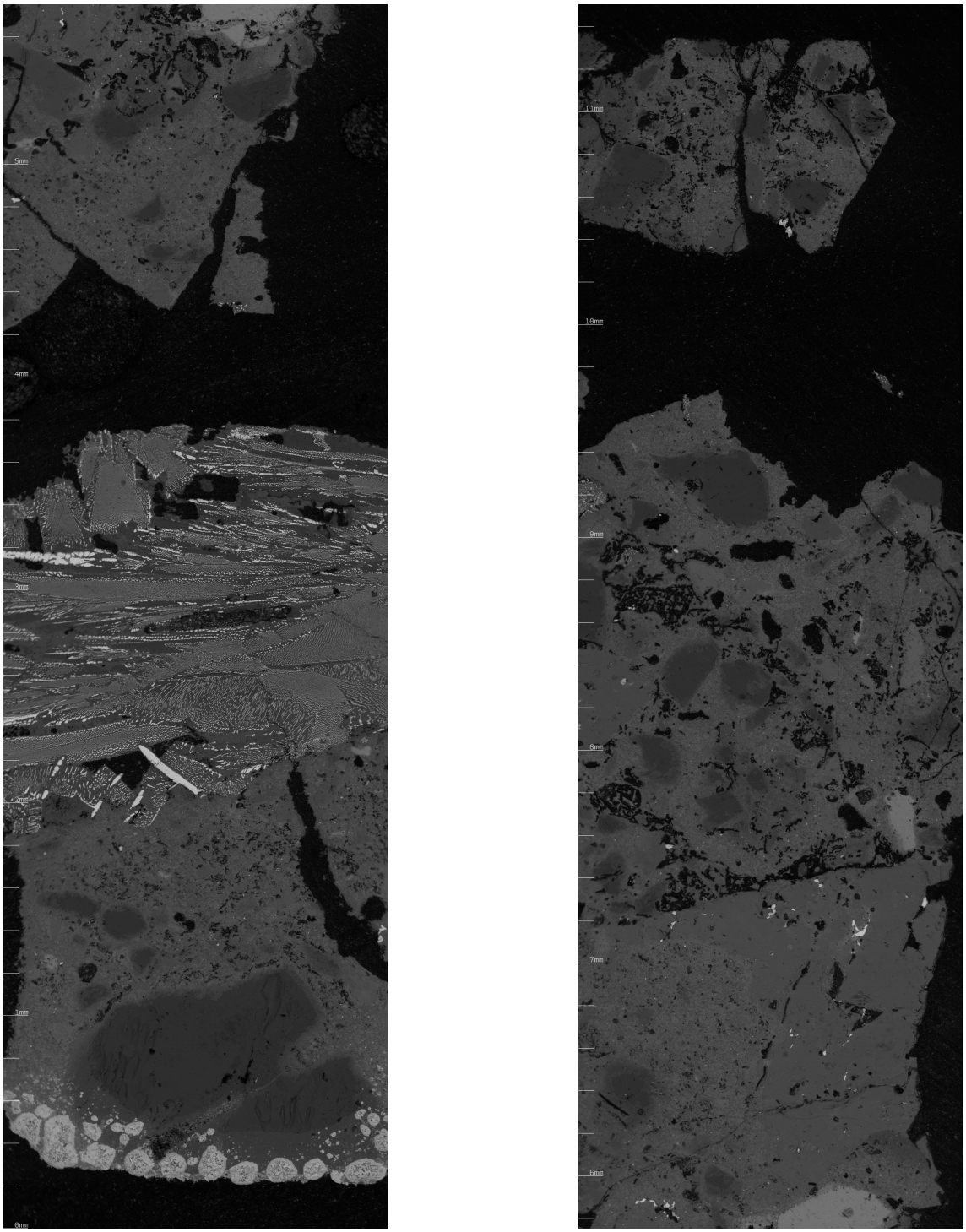

Figure 42: Panoramic BSE image of a part of the cross section of the Resistal RK30 refractory. The bottom of the refractory was in contact with the synthetic exhaust gas and the top with the reducing atmosphere.

picture of the full cross section from the mounted refractory part can be seen in Figure 43. A more detailed panoramic picture of the cross section of this refractory can be found in Figure 44. In the pictures the bottom of the refractory was in contact with the synthetic exhaust gas and the top with the reducing atmosphere. The left side was situated near the center of the crucible, and the right side on the outside of the crucible. In the panoramic picture can be seen that the refractory has expanded to roughly 18% of the original thickness.

In the structure of the refractory it can be seen that the refractory consists of large coarse magnesia grains held together by a porous magnesia binder. Spread within the coarse grains and the binder are small amounts of calcium oxide and silica. It can also be seen that the refractory has been penetrated in a cone like shape starting from the center of the crucible by a heavy element. This element seems to have mainly affected certain parts of the coarse grains and be distributed more evenly through the binder. Deeper within the coarse grains no potassium was measured but in the parts affected by the heavy element, potassium concentrations ranged between 20 and 25 mol% near the interface. The heavy element that has been found to have penetrated the refractory is molybdenum just as with the second refractory. In this case the molybdenum has penetrated the whole depth of the refractory. The form of the molybdenum in this refractory was shaped as a molten material that has filled up a hole in another material in contrast to the previous refractory where it formed bubbles near the interface.

At a penetration depth of approximately 1 mm, the calcium oxide and silica phase has been found to be in contact with the phase consisting mainly of potassium and molybdenum. However, the calcium oxide and silica phase itself has been found not to be affected by the potassium or molybdenum. By the by molybdenum affected parts throughout the whole refractory potassium concentrations around 20 and 25 mol% were found, meaning that the whole refractory was penetrated by the synthetic exhaust gas. Also, the exhaust gas could affect the coarse grains but not the calcium silica phase within the refractory.

Durital E90 was the fourth tested refractory, with as main components alumina and silica. A Picture of the full cross section from the refractory can be seen in Figure 45. A more detailed panoramic picture of the cross section of this refractory can be found in Figure 46. In the pictures the bottom of the refractory was in contact with the synthetic exhaust gas and the reducing atmosphere came in flowing from the top. In the full picture it can be seen that the bottom right was situated near the center of the crucible, whereas the left was situated on the outside of the crucible. In the panoramic picture it can be seen that the refractory consists of grains of alumina (darker) held together by a binder consisting of alumina and silica (lighter). In the panoramic picture can be seen that the refractory has expanded to roughly 25% of the original thickness.

In the structure of the refractory it can be seen that in the bottom right corner the porosity has decreased compared to the rest of the refractory. A light grey phase can be distinguished in the area with decreased porosity, thus that area has filled up with heavier elements. Using the EDS it has been identified that the bottom of the sample has been penetrated by molybdenum and potassium. light areas, as

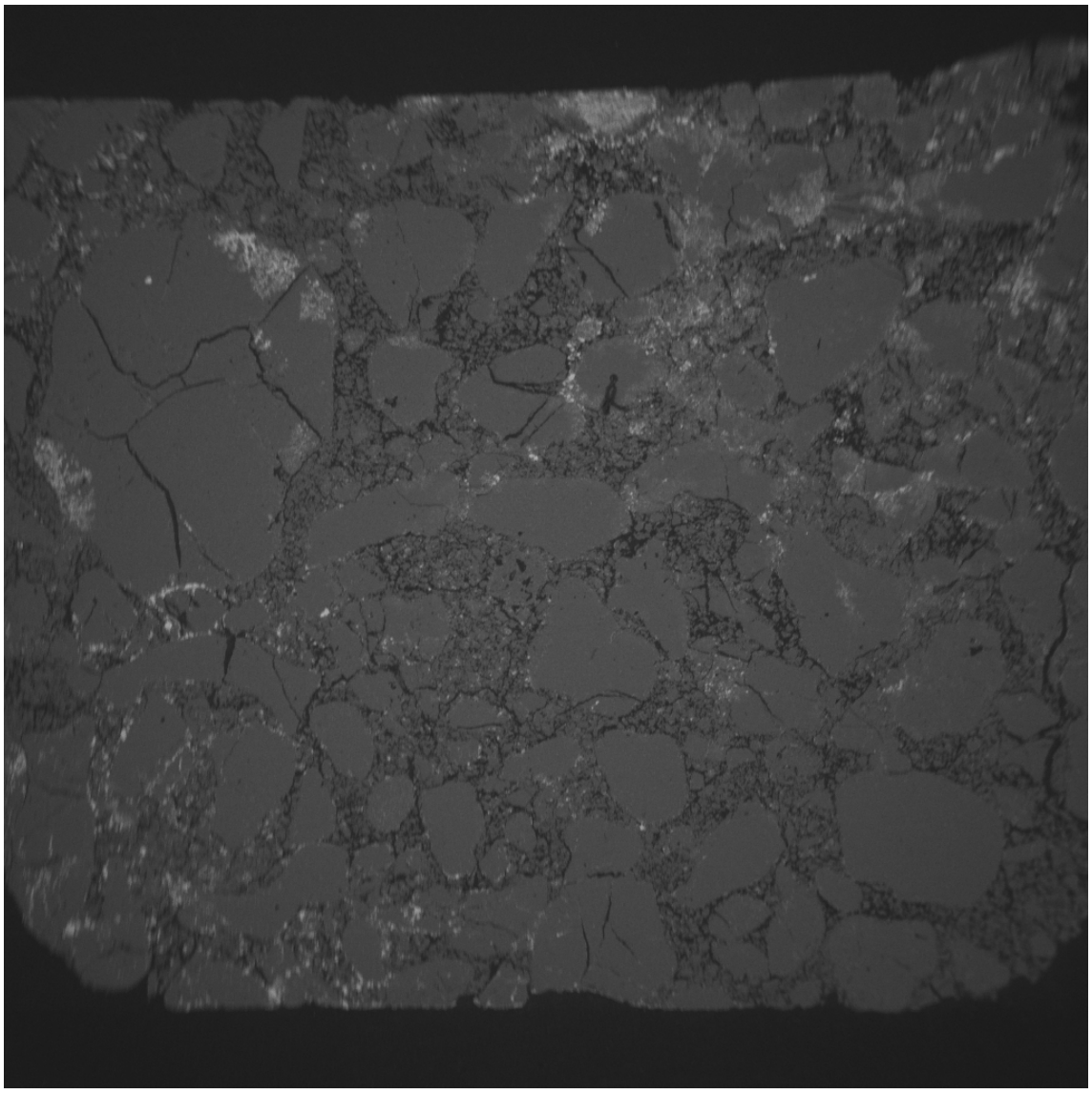

Figure 43: BSE image of cross section of the Radex S refractory.

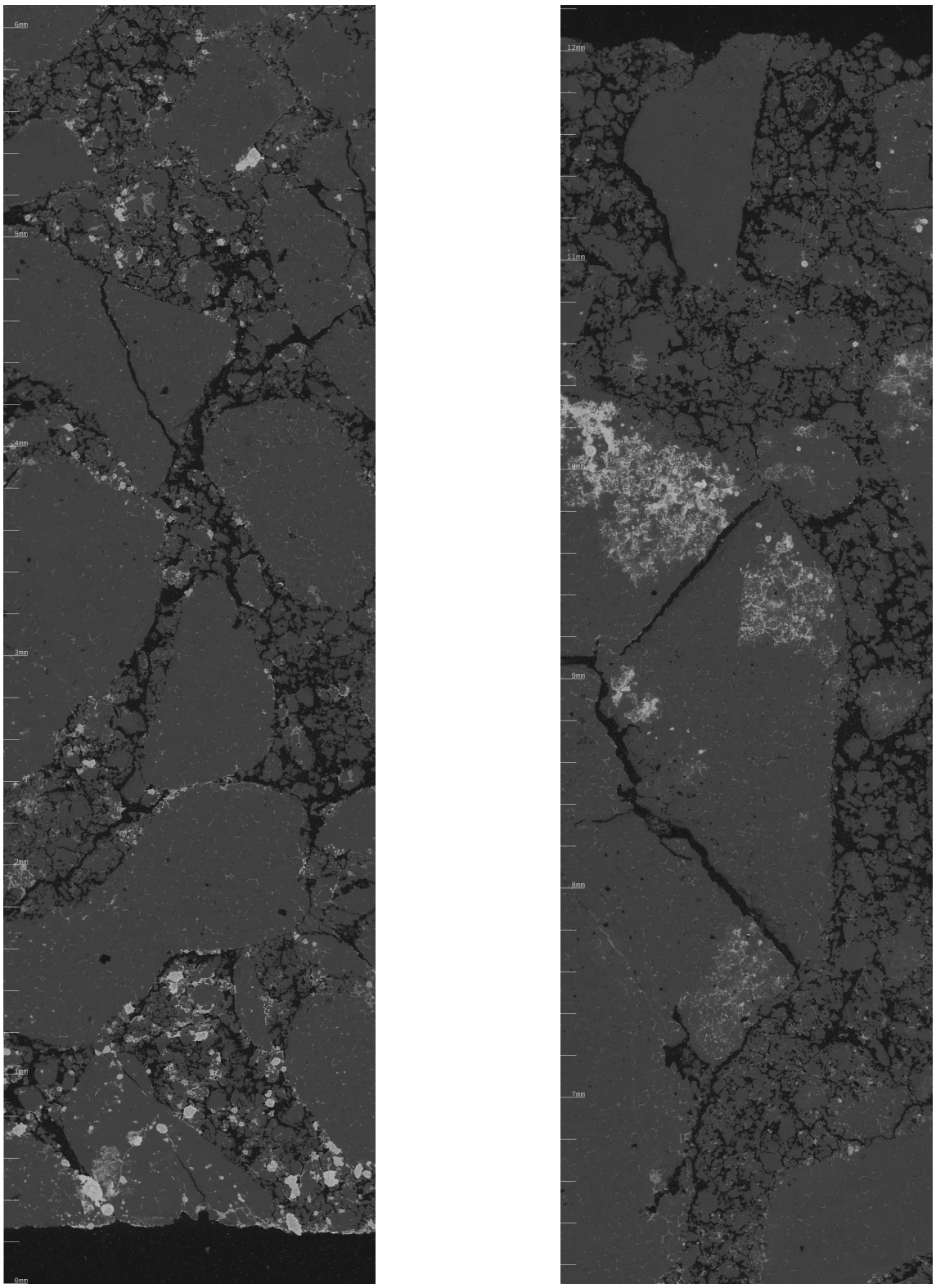

Figure 44: Panoramic BSE image of a part of the cross section of the Radex S refractory. The bottom of the refractory was in contact with the synthetic exhaust gas and the top with the reducing atmosphere.

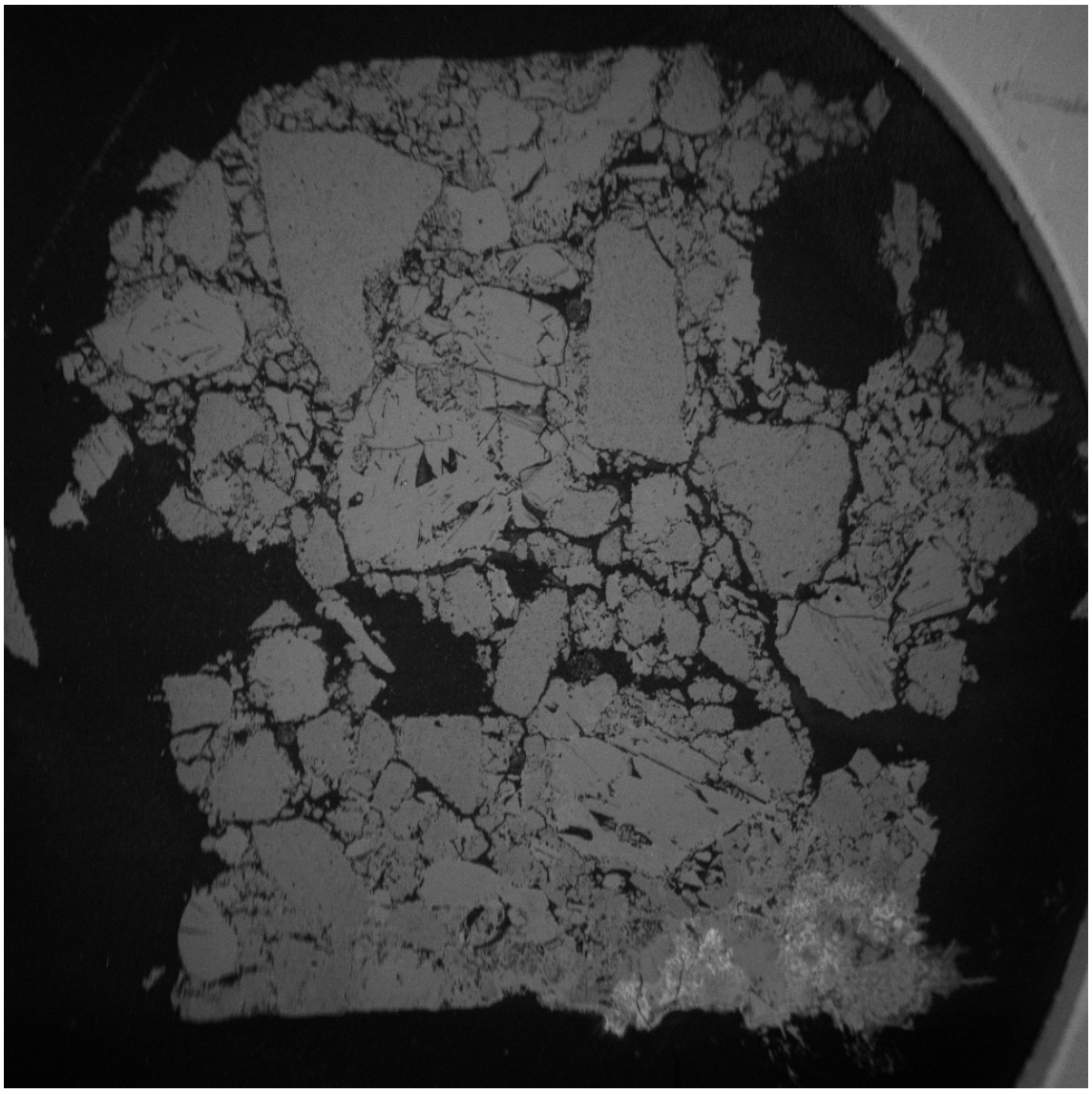

Figure 45: BSE image of cross section of the Durital E90 refractory.

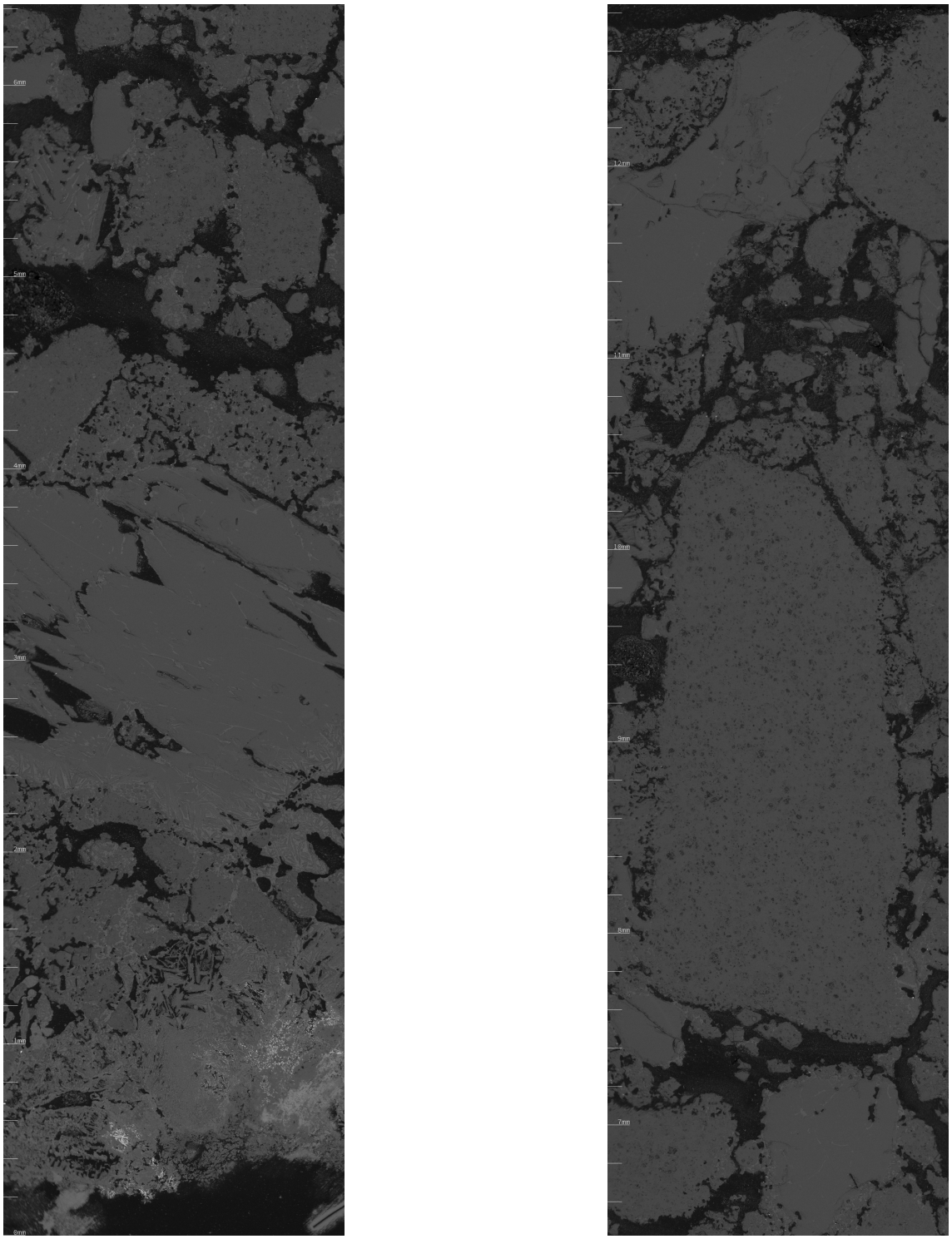

Figure 46: Panoramic BSE image of a part of the cross section of the Durital E90 refractory. The bottom of the refractory was in contact with the synthetic exhaust gas and the top with the reducing atmosphere.

can be more clearly seen in the panoramic picture, contain approximately 13 mol% molybdenum and 20 mol% potassium.

The potassium concentration in the alumina grains near the surface was around 5 mol% and within the binder it was around 14 mol%. At a penetration depth of 2 mm no potassium was found in the alumina grains, whereas the potassium concentration in the binder phase was still similar to the concentration at the surface. At a penetration depth of 2.5 mm the potassium concentration in the binder phase decreased to around 10 mol%. This concentration further decreased to around 7.5 mol% at 7 mm and finally 5 mol% at the top of the refractory. At a penetration depth of 10.5-11 mm some areas with high concentrations of molybdenum were found. These small areas with high molybdenum concentrations did, however, contain only low concentrations of potassium of approximately 2 mol%.

Criado, Moya, and Aza (1981) found that the interaction between high alumina refractories and potassium caused 20% expansion due to the formation of potassium $\beta \cdot Al_2O_3$. Further, it was found by Narita et al. (1981) that fireclay bricks installed in the tuyere zone of a blast furnace had swelled by 5-30%. The Durital E90 refractory, which is an alumina-silica refractory, had expanded 25%, this is comparable to what was found by Criado, Moya, and Aza (1981). The alumina content of the Durital E90 is higher than in the fireclay bricks examined by Narita et al. (1981), even so the expansion found in this research falls within the same range. The Resistal RK30, which is an alumina-chrome refractory, exhibited an expansion of roughly 10%. The lower expansion could be caused by the added resistance to corrosion due to the chrome content. A similar trend was seen with the Radex OX6 and Radex S refractories, where the Radex S is a magnesia refractory and the Radex OX6 a magnesia-chrome refractory. The expansion suffered by these refractories was 18% and 6%, respectively.

The cracking of refractories caused by expansion was discussed by Oprea (2004) and Scudeller, Longo, and Varela (1990), amongst others. However, no crack formation could be identified in the BSE pictures and visual analyses. This difference might have several causes, such as the small size of the bricks tested or the duration of the experiments.

It was found by Park et al. (2010) that magnesia grains were dissolved by fluorine containing slags. The BSE pictures from this work gave no evidence of the dissolution of the magnesia grains in the Radex OX6 or Radex S refractories by the fluorine in the gas phase.

Prigent, Bouchetou, and Poirier (2011) had found that the interaction between sodium and alumina refractories caused the formation of corundum needles in the brick matrix. No evidence could be found of corundum needles in the Durital E90 and the Resistal RK30. Consequently, these two refractories are more resistant to the formation of a glassy phase than the fireclay brick and andalusite based brick used by Prigent, Bouchetou, and Poirier (2011), or potassium does not cause the formation of corundum needles.

The apparent porosity of the unused refractories was similar for all four refractories, between 15 and 17 vol%. In the BSE pictures (see Figures **??**) of the refractories after exposure to the synthetic gas, it can be seen that the Radex S refractory is

more porous than the others. The porosity in the Radex OX6 had been mainly reduced in the first 4 mm of the refractory. In the same manner, the porosity in the Resistal RK30 was mainly reduced up to a depth of 7 mm. The porosity of the Durital E90 was reduced up to a depth of 1 mm, from a depth of 3-4 mm the porosity has increased.

Reduction of the porosity can be attributed to the deposition of materials from the synthetic dust and the formation of new compounds from the interaction between the gas and the refractory. The increased porosity in the Radex S refractory can possibly be attributed to the reaction of fluorine with magnesia, forming magnesium fluoride, which is liquid at the experimental temperatures used in this work. (DeLucia and Wolfe 2000) Some glassy phases had been found on the side of the alumina crucible, this was however disregarded as remnants of the synthetic dust. The increased porosity of the Durital E90 refractory can be attributed to two reactions. The interaction between silica and fluorine can form silicon tetrafluoride, which is highly volatile. (DeLucia and Wolfe 2000) Silica can also react with carbon monoxide, forming silicon monoxide gas in the temperature range 1000-1600 °C. (Kronert and Bahl 1978)

5 Summary and Conclusions

In this work, experiments were conducted to determine the effects of steel making dusts on four industrial refractory bricks. First, the behaviour of the components of steel making dusts was determined at operating temperatures. Second, experiments were conducted to investigate the effects of a synthetic dust on four commercial refractories. Additionally, the degradation of those refractories was compared.

In the experiments to determine the behaviour of steel making dusts, it was found that melt formation starts between 1300 and 1350 °C in the VKU2 dust and that at the higher end of this range about 30% of the sample is in a molten state. For the VKU1 dust, melt formation started between 1250 and 1300 °C and the molten phase constituted almost 50% of the sample. At temperature as low as 1200 °C, 30% of the AOD dust was in a molten state. Industrial operators can use this knowledge to estimate the possible adhesion locations in their operational setups, and thus where gas-solid and liquid-solid state corrosion can occur.

In the AOD dust, high levels of fluorine were found in the liquid phase, whereas fluorine was mainly detected in the EAF dusts in solid spinels. Sodium and potassium were only found in trace amounts, suggesting that the alkali metals evaporated from the sample and would be in the gas phase. Finally, chlorine was not found in the samples and would thus be in gas phase compounds in the furnace.

In the refractory - dust interaction experiments, it was found in the Radex OX6 refractory, that potassium penetration occurred to approximately 5 mm. Penetration of potassium in the Resistal RK30 occurred up to approximately 4.5 mm. Potassium was found throughout the whole depth of the Radex S refractory. In the Durital E90, molybdenum and potassium were found to have penetrated the whole refractory, but potassium concentrations had strongly decreased at the top of the refractory. This was not the case for the Radex S.

In general it was found that the chrome containing refractories were less affected by the synthetic dust under a strongly reducing atmosphere. Consequently, it can be concluded that the Radex OX6 and the Resistal RK30 performed best compared to the other refractories. These refractories suffered the least expansion, and they had the lowest potassium penetration values. The potassium penetration depth also appears to be similar to the depth at which the refractory has been affected.

6 For future work

For future work it could be worthwhile to investigate automatising the process of analysing the images. It is not known to the author of the thesis if there are techniques to quantify the amount of molten material in a sample other than using the image analyses performed in this work. Preparing the images and extracting the information from them involves a significant amount of labour. Automating this could benefit future research. Challenges in automating would arise from the differing grey scales in the phases in different dusts or temperatures.

Improvements could be made to the accuracy of the interpretation of the BSE images, if the images could be compared to BSE images from refractories heated without the presence of dust.

It was not possible to measure the weight changes in all the refractory lids and crucibles. Some interesting changes were found, although not reported since they were incomplete.

Finally, the molybdenum holding crucible was used under the assumption that it would be an inert crucible under reducing atmosphere at the used temperatures of 1300 °C and lower. However, since the concentrations of molybdenum found throughout multiple samples, this was apparently not the case. Of course, this can be influenced by the synthetic exhaust dust. Even so, the molybdenum was mainly found under the lid with the highest concentrations near the center of the refractory lid. This is almost the furthest part from the molybdenum holding crucible to the refractory lid. It is suggested for future work to determine how the molybdenum ends up in the sample.

References

Aslanoglu, Z., Baglan, Ç., and Soykan, H. Ş. (Oct. 2017). "Influence of SiC addition on the properties of andalusite brick used in EAF dust recovery kiln". In: *Journal of the Australian Ceramic Society* 53.2, pp. 517–522. DOI: 10.1007/s41779-017-0062-6.

Benson, S. A., Sondreal, E. A., and Hurley, J. P. (Sept. 1995). "Status of coal ash behavior research". In: *Fuel Processing Technology* 44.1, pp. 1–12. DOI: 10.1016/0378-3820(95)00020-8.

Bhatia, A. (2012). *Overview of refractory Materials online course*. Online course. URL: https://pdhonline.com/courses/m158/m158_new.htm.

Brosnan, D. A. (Aug. 2004). "Corrosion of Refractories". In: *Refractories Handbook*. Ed. by C. A. Schacht. Refractories Handbook. CRC Press, pp. 39–77. DOI: 10.1201/9780203026328.ch3.

Buzin, P. J. W. K. de, Heck, N. C., and Vilela, A. C. F. (Apr. 2017). "EAF dust: An overview on the influences of physical, chemical and mineral features in its recycling and waste incorporation routes". In: *Journal of Materials Research and Technology* 6.2, pp. 194–202. DOI: 10.1016/j.jmrt.2016.10.002.

Callister, W. D. and Rethwisch, D. G. (2013). *Materials Science and Engineering: An Introduction*. 9th ed. Wiley.

Caprio, J. A. and Wolfe, H. E. (May 1982). "Refractories for hazardous waste incineration - an overview". In: *Proceedings of the ASME National Solid Waste Processing Conference*.

Chen, J., Jiao, F., et al. (Oct. 2013). "Elucidating the mechanism of Cr(VI) formation upon the interaction with metal oxides during coal oxy-fuel combustion". In: *Journal of Hazardous Materials* 261, pp. 260–268. DOI: 10.1016/j.jhazmat.2013.07.023.

Chen, J., Chen, L., et al. (Oct. 2018). "Corrosion and penetration behaviors of slag/steel on the corroded interfaces of Al2O3-C refractories: Role of Ti3AlC2". In: *Corrosion Science* 143, pp. 166–176. DOI: 10.1016/j.corsci.2018.08.022.

Chen, L. et al. (June 2016). "Effect of ZnO level in secondary copper smelting slags on slag/magnesia-chromite refractory interactions". In: *Journal of the European Ceramic Society* 36.7, pp. 1821–1828. DOI: 10.1016/j.jeurceramsoc.2016.02.004.

Coda, B. et al. (Apr. 2001). "Behavior of chlorine and enrichment of risky elements in bubbling fluidized bed combustion of biomass and waste assisted by additives". English. In: *Energy & Fuels* 15.3, pp. 680–690. DOI: 10.1021/ef000213+.

Criado, E., Moya, J. S., and Aza, S. D. (Mar. 1981). "Alkalines vapour attack on a high alumina refractory". In: *Ceramics International* 7.1, pp. 19–21. DOI: 10.1016/0272-8842(81)90034-1.

Crivits, T. (July 2016). "Fundamental studies on the chemical aspects of freeze linings". PhD thesis. DOI: 10.14264/uql.2016.506.

Davis, R. F., Aksay, I. A., and Pask, J. A. (Feb. 1972). "Decomposition of mullite". In: *Journal of the American Ceramic Society* 55.2, pp. 98–101. DOI: 10.1111/j.1151-2916.1972.tb11218.x.

Dayton, D. C., Belle-Oudry, D., and Nordin, A. (Nov. 1999). "Effect of Coal Minerals on Chlorine and Alkali Metals Released during Biomass/Coal Cofiring". In: *Energy & Fuels* 13.6, pp. 1203–1211. DOI: 10.1021/ef9900841.

DeLucia, M. A. and Wolfe, H. E. (Oct. 2000). "Refractories to contain fluorinated waste streams". In: *Waste Management* 20.5, pp. 449–454. DOI: 10.1016/S0956-053X(00)00010-6.

Domínguez, M. I. et al. (Nov. 2010). "Physicochemical characterization and use of wastes from stainless steel mill". In: *Environmental Progress & Sustainable Energy* 29.4, pp. 471–480. DOI: 10.1002/ep.10435.

Gregurek, D. et al. (Feb. 2016). "Zinc and Refractories – A Nasty Relation". In: *7th International Symposium on High-Temperature Metallurgical Processing*. Springer International Publishing, pp. 149–156. DOI: 10.1007/978-3-319-48093-0_19.

Han, J. S. et al. (Aug. 2018). "Influence of CaF2 in calcium aluminate-based slag on the degradation of magnesia refractory". In: *Ceramics International* 44.11, pp. 13197–13204. DOI: 10.1016/j.ceramint.2018.04.145.

Hayashi, T., Nishio, H., and Ayuzawa, N. (Jan. 1983). "The Behaviour of Alkali to Alumina". In: *InterCeram* 32, pp. 68–71.

Hu, H., Luo, G., et al. (Jan. 2013). "Fate of chromium during thermal treatment of municipal solid waste incineration (MSWI) fly ash". In: *Proceedings of the Combustion Institute* 34.2, pp. 2795–2801. DOI: 10.1016/j.proci.2012.06.181.

Hu, H., Xu, Z., et al. (2015). "Mechanism of chromium oxidation by alkali and alkaline earth metals during municipal solid waste incineration". In: *Proceedings of the Combustion Institute* 35.2, pp. 2397–2403. DOI: 10.1016/j.proci.2014.08.029.

Kashiwaya, Y. et al. (Oct. 2004). "Thermodynamic Analysis on the Dust Generation from EAF for the Recycling of Dust". In: *ISIJ International* 44.10, pp. 1774–1779. DOI: 10.2355/isijinternational.44.1774.

Kazanbaev, L. et al. (July 2004). "Wear of Basic Refractories in the Lining of Waelz Kilns in the Production of Zinc". In: *Refractories and Industrial Ceramics* 45.4, pp. 225–227. DOI: 10.1023/B:REFR.0000046500.89787.2c.

Kekki, A., Aromaa, J., and Forsen, O. (2012). "Leaching characteristics of EAF and AOD stainless steel production dusts". In: *Physicochemical Problems of Mineral Processing* 48.2, pp. 599–606. DOI: 10.5277/ppmp120223.

Ko, Y. C. (1991). "Wear of refractories in the Iron and Steel industry". In: *SEASAI quarterly* 20.2, pp. 19–29.

Kronert, W. and Bahl, H. (1978). "The influence of various gas atmospheres on the melting behavior of mullite". In: *InterCeram* 1, pp. 72–75.

Luptáková, N., Anisimov, E., and Pešlová, F. (July 2014). "The degradation of lining of rotary furnaces in the production of zinc oxide". In: *Materials Engineering-Materiálové inžinierstvo (MEMI)* 21.3, pp. 116–121. URL: http://ojs.mateng.sk/index.php/Mateng/article/view/133.

Luz, A. et al. (June 2018). "High-alumina refractory castables bonded with novel alumina-silica-based powdered binders". In: *Ceramics International* 44.8, pp. 9159–9167. DOI: 10.1016/j.ceramint.2018.02.124.

Machado, J. G. M. S. et al. (Aug. 2006). "Chemical, physical, structural and morphological characterization of the electric arc furnace dust". In: *Journal of Hazardous Materials* 136.3, pp. 953–960. DOI: 10.1016/j.jhazmat.2006.01.044.

Mahapatra, M. K. (Nov. 2019). "Review of corrosion of refractory in gaseous environment". In: *International Journal of Applied Ceramic Technology* 17.2, pp. 606–615. DOI: 10.1111/ijac.13418.

Malfliet, A. et al. (Mar. 2014). "Degradation mechanisms and use of refractory linings in copper production processes: A critical review". In: *Journal of the European Ceramic Society* 34.3, pp. 849–876. DOI: 10.1016/j.jeurceramsoc.2013.10.005.

Mao, L., Deng, N., et al. (Nov. 2016). "Effects of Al2O3, Fe2O3, and SiO2 on Cr (VI) formation during heating of solid waste containing Cr (III)". In: *Chemical engineering journal* 304, pp. 216–222. DOI: 10.1016/j.cej.2016.06.086.

Mao, L., Gao, B., et al. (Feb. 2016). "Oxidation behavior of Cr(III) during thermal treatment of chromium hydroxide in the presence of alkali and alkaline earth metal chlorides". In: *Chemosphere* 145, pp. 1–9. DOI: 10.1016/j.chemosphere.2015.11.053.

Narita, K. et al. (1981). "Effects of Alkalis and Zinc on the Wear of Blast Furnace Refractories and the Tuyere Displacement". In: *Transactions of the Iron and Steel Institute of Japan* 21.12, pp. 839–845. DOI: 10.2355/isijinternational1966.21.839.

Omran, M. and Fabritius, T. (Feb. 2017). "Effect of steelmaking dust characteristics on suitable recycling process determining: Ferrochrome converter (CRC) and electric arc furnace (EAF) dusts". In: *Powder Technology* 308, pp. 47–60. DOI: 10.1016/j.powtec.2016.11.049.

Oprea, G. (2004). "Failure mechanisms of refractory linings for non-ferrous flash smelting furnaces". In: *Iranian Journal of Material Science and Engineering* 3.3, pp. 9–15.

Oustadakis, P. et al. (2010). "Hydrometallurgical process for zinc recovery from electric arc furnace dust (EAFD)". In: *Journal of Hazardous Materials* 179.1, pp. 1–7. DOI: 10.1016/j.jhazmat.2010.01.059.

Owens, W. D. J. (Jan. 1991). *Hazardous-waste incineration in a rotary kiln.* Tech. rep. Salt Lake City, UT (US); Univ. of Utah. URL: https://www.osti.gov/biblio/5016258.

Park, J. H. et al. (Oct. 2010). "Interfacial Reaction between Refractory Materials and Metallurgical Slags containing Fluoride". In: *steel research international* 81.10, pp. 860–868. DOI: 10.1002/srin.201000157.

Prigent, P., Bouchetou, M. L., and Poirier, J. (2011). *Andalusite: An amazing refractory raw material with excellent corrosion resistance to sodium vapours.*

Remus, R. et al. (2013). "Best available techniques (BAT) reference document for iron and steel production". In: *EUR (Luxembourg)* 25521. URL: http://dx.publications.europa.eu/10.2791/98516.

Rinne, M. (2019). "Pyrometallurgical Treatment of Jarosite Leach Residue by Non-fossil Reductant". PhD thesis.

Sarkar, D. (2019). *Ceramic processing: Industrial Practices*. 1st ed. New York: CRC Press, pp. 200–2001.

Satyendra (2020). *Refractories and Classification of Refractories*. URL: https://www.ispatguru.com/refractories-and-classification-of-refractories/.

Scudeller, L. A. M., Longo, E., and Varela, J. A. (May 1990). "Potassium Vapor Attack in Refractories of the Alumina–Silica System". In: *Journal of the American Ceramic Society* 73.5, pp. 1413–1416. DOI: 10.1111/j.1151-2916.1990.tb05214.x.

Selkregg, K. (2018). "Fusion cast refractories: roles of containment". In: *American Ceramic Society Bulletin* 97.2, pp. 21–28.

Simonyan, L. M., Alpatova, A. A., and Demidova, N. V. (Apr. 2019). "The EAF dust chemical and phase composition research techniques". In: *Journal of Materials Research and Technology* 8.2, pp. 1601–1607. DOI: 10.1016/j.jmrt.2018.11.005.

Snegirev, A. I., Perepelitsyn, V. A., and Kudryavtseva, T. N. (Mar. 1984). "Interaction of molten zinc with an aluminosilicate rammed mixture". In: *Refractories* 25.3-4, pp. 184–187. DOI: 10.1007/BF01398359.

Spear, K. E. and Allendorf, M. D. (2002). "Thermodynamic Analysis of Alumina Refractory Corrosion by Sodium or Potassium Hydroxide in Glass Melting Furnaces". In: *Journal of The Electrochemical Society* 149.12, B551. DOI: 10.1149/1.1516773.

Stjernberg (2008). *Degradation of mullite based materials by alkali containing slags*. Vol. 2008:41. Lulea: Division of Engineering Materials LuleåUniversity of Technology Lulea. URL: http://libris.kb.se/resource/bib/11236279.

Stjernberg, J. et al. (Jan. 2013). "Laboratory scale study of the degradation of mullite/corundum refractories by reaction with alkali-doped deposit materials". In: *Ceramics International* 39.1, pp. 791–800. DOI: 10.1016/j.ceramint.2012.06.094.

Suetens, T. et al. (2014). "Moving towards better recycling options for electric arc furnace dust." In: *Journal of Materials* 66.7.

Verbinnen, B. et al. (2013). "Heating Temperature Dependence of Cr (III) Oxidation in the Presence of Alkali and Alkaline Earth Salts and Subsequent Cr(VI) Leaching Behavior". In: *Environmental Science & Technology* 47.11. PMID: 23635007, pp. 5858–5863. DOI: 10.1021/es4001455.

Wegscheider, S. et al. (Aug. 2015). "The 2sDR process - Innovative treatment of electric arc furnace dust". In: *WASTES 2015 - Solutions, Treatments and Opportunities*. CRC Press, pp. 355–360. DOI: 10.1201/b18853-59.

Wei, X. et al. (Sept. 2002). "Assessment of Chlorine-Alkali-Mineral Interactions during Co-Combustion of Coal and Straw". In: *Energy & Fuels* 16.5, pp. 1095–1108. DOI: 10.1021/ef0102925.

Wu, Y. et al. (June 2018). "Formation and leachability of hexavalent chromium in the Al 2 O 3 -CaO-MgO-Cr 2 O 3 system". In: *Journal of the European Ceramic Society* 38.6, pp. 2649–2661. DOI: 10.1016/j.jeurceramsoc.2018.01.012.

Xiao, Z. and Mitchell, B. S. (Apr. 2000). "Mullite Decomposition Kinetics and Melt Stabilization in the Temperature Range 1900—2000°C". In: *Journal of*

the American Ceramic Society 83.4, pp. 761–767. DOI: 10.1111/j.1151-2916.2000.tb01271.x.

Xu, Y. et al. (May 2019). "Corrosion mechanisms of magnesia-chrome refractories in copper slag and concurrent formation of hexavalent chromium". In: *Journal of Alloys and Compounds* 786, pp. 306–313. DOI: 10.1016/j.jallcom.2019.01.314.

Yazhenskikh, E., Hack, K., and Müller, M. (Dec. 2006). "Critical thermodynamic evaluation of oxide systems relevant to fuel ashes and slags Part 2: Alkali oxide-alumina systems". In: *Calphad-computer Coupling of Phase Diagrams and Thermochemistry - CALPHAD-COMPUT COUP PHASE DIA* 30, pp. 397–404. DOI: 10.1016/j.calphad.2006.08.002.

Zhang, G. et al. (2015). "Ash melting behavior and slag infiltration into alumina refractory simulating co-gasification of coal and biomass". In: *Fuel* 139, pp. 457–465. DOI: 10.1016/j.fuel.2014.09.029.

A Selected analysis points from Radex OX6

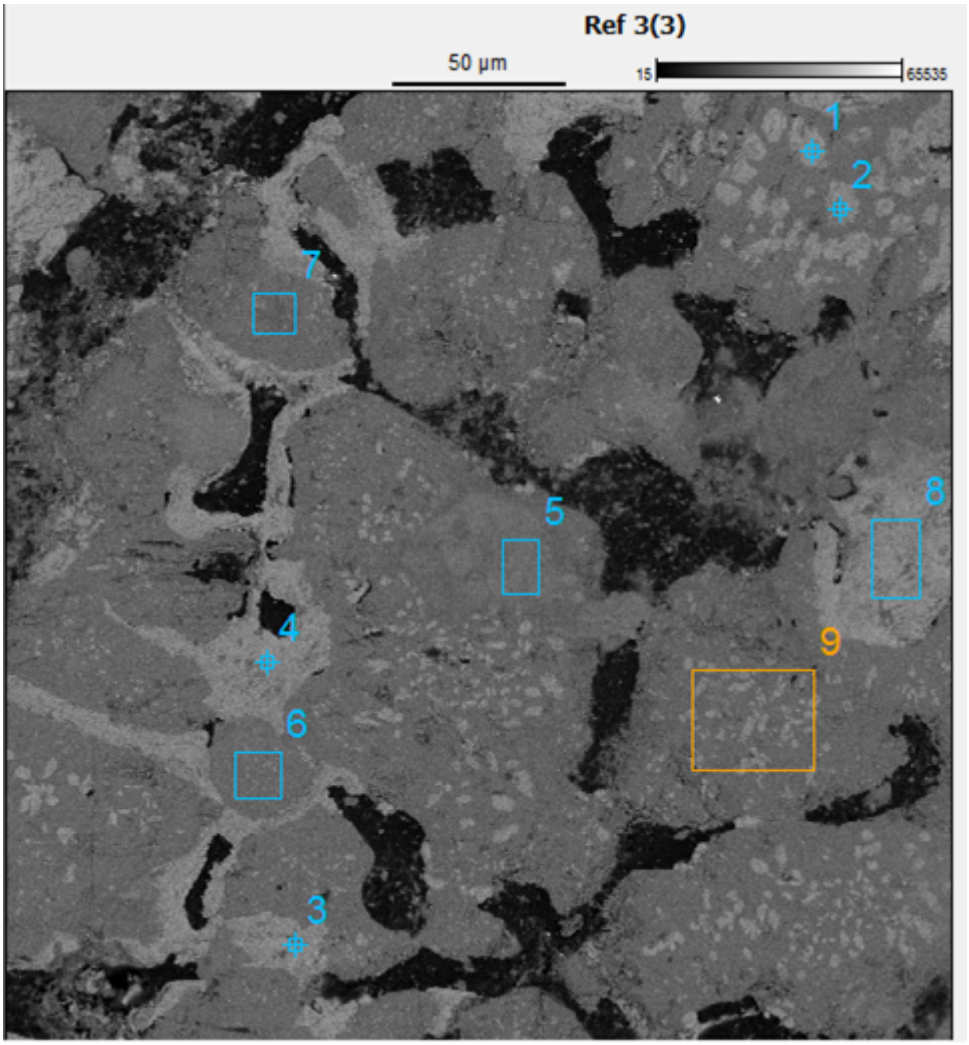

Figure 47: Analysed areas in section 3 on the Radex OX6 refractory.

Table 8: Measured composition values in area 1 from section 3 on the Radex OX6 refractory

Element Line	Element Wt.%	Norm. Wt.%	Atom %
O K	23,94	27,66	45,6
F K	0	0	0
Na K	0,26	0,3	0,34
Mg K	19,93	23,02	24,99
Al K	7,63	8,81	8,62
Si K	0,03	0,04	0,03
Cl K	0	0	0
K K	0,99	1,14	0,77
Ca K	0,35	0,4	0,27
Cr K	27,97	32,3	16,39
Fe K	5,47	6,32	2,99
Total	86,57	100	100

Table 9: Measured composition values in area 2 from section 3 on the Radex OX6 refractory

Element Line	Element Wt.%	Norm. Wt.%	Atom %
O K	20,25	25,19	42,61
F K	0	0	0
Na K	0,12	0,14	0,17
Mg K	16,66	20,73	23,08
Al K	9,12	11,35	11,38
Si K	0,33	0,41	0,39
Cl K	0,01	0,02	0,01
K K	2,6	3,23	2,23
Ca K	0,5	0,62	0,42
Cr K	25,43	31,64	16,47
Fe K	5,38	6,69	3,24
Total	80,39	100	100

Table 10: Measured composition values in area 3 from section 3 on the Radex OX6 refractory

Element Line	Element Wt.%	Norm. Wt.%	Atom %
O K	22,68	26,87	44,49
F K	0	0	0
Na K	0,21	0,25	0,29
Mg K	21,63	25,62	27,93
Al K	5,91	7	6,88
Si K	0,04	0,04	0,04
Cl K	0,01	0,01	0,01
K K	0,39	0,47	0,32
Ca K	0,34	0,4	0,26
Cr K	27,01	31,99	16,3
Fe K	6,2	7,35	3,49
Total	84,41	100	100

Table 11: Measured composition values in area 4 from section 3 on the Radex OX6 refractory

Element Line	Element Wt.%	Norm. Wt.%	Atom %
O K	22,92	27,59	45,59
F K	0	0	0
Na K	0,18	0,21	0,24
Mg K	17,64	21,23	23,09
Al K	7,6	9,14	8,96
Si K	0,11	0,14	0,13
Cl K	0,01	0,01	0,01
K K	3,83	4,61	3,12
Ca K	1,37	1,65	1,09
Cr K	23,85	28,7	14,59
Fe K	5,57	6,71	3,17
Total	83,08	100	100

Table 12: Measured composition values in area 5 from section 3 on the Radex OX6 refractory

Element Line	Element Wt.%	Norm. Wt.%	Atom %
O K	35,77	41,31	58,55
F K	0	0	0
Na K	0,28	0,33	0,32
Mg K	8,98	10,37	9,68
Al K	13,73	15,85	13,32
Si K	1,76	2,03	1,64
Cl K	0,02	0,03	0,02
K K	20,11	23,23	13,47
Ca K	1,35	1,56	0,88
Cr K	2,03	2,34	1,02
Fe K	2,03	2,35	0,95
Mo L*	0,53	0,61	0,14
Total	86,6	100	100

* Standard Unavailable

Table 13: Measured composition values in area 6 from section 3 on the Radex OX6 refractory

Element Line	Element Wt.%	Norm. Wt.%	Atom %
O K	26,16	28,69	41,44
F K	0	0	0
Na K	0,86	0,95	0,95
Mg K	45,64	50,06	47,59
Al K	2,24	2,46	2,1
Si K	0,02	0,02	0,02
Cl K	0,02	0,03	0,02
K K	1,74	1,91	1,13
Ca K	0,34	0,37	0,21
Cr K	3,59	3,94	1,75
Fe K	10,55	11,58	4,79
Total	91,17	100	100

Table 14: Measured composition values in area 7 from section 3 on the Radex OX6 refractory

Element Line	Element Wt.%	Norm. Wt.%	Atom %
O K	30,11	33,71	48,11
F K	0	0	0
Na K	0,53	0,59	0,58
Mg K	31,95	35,76	33,6
Al K	7,78	8,7	7,37
Si K	0	0	0
Cl K	0	0	0
K K	7,16	8,02	4,68
Ca K	0,75	0,84	0,48
Cr K	3,45	3,87	1,7
Fe K	7,6	8,51	3,48
Total	89,33	100	100

Table 15: Measured composition values in area 8 from section 3 on the Radex OX6 refractory

Element Line	Element Wt.%	Norm. Wt.%	Atom %
O K	23,75	28,29	46,16
F K	0	0	0
Na K	0,23	0,27	0,31
Mg K	17,16	20,44	21,95
Al K	9,97	11,87	11,49
Si K	0,15	0,18	0,17
Cl K	0	0	0
K K	2,53	3,01	2,01
Ca K	0,61	0,72	0,47
Cr K	24,07	28,68	14,4
Fe K	5,48	6,53	3,05
Total	83,95	100	100

Table 16: Measured composition values in area 9 from section 3 on the Radex OX6 refractory

Element Line	Element Wt.%	Norm. Wt.%	Atom %
O K	24,39	27,98	41,48
F K	0	0	0
Na K	0,6	0,69	0,71
Mg K	38,41	44,06	43
Al K	4,25	4,88	4,29
Si K	0,05	0,06	0,05
Cl K	0,01	0,01	0,01
K K	2,91	3,34	2,03
Ca K	0,61	0,7	0,41
Cr K	7,35	8,44	3,85
Fe K	8,57	9,83	4,18
Total	87,16	100	100

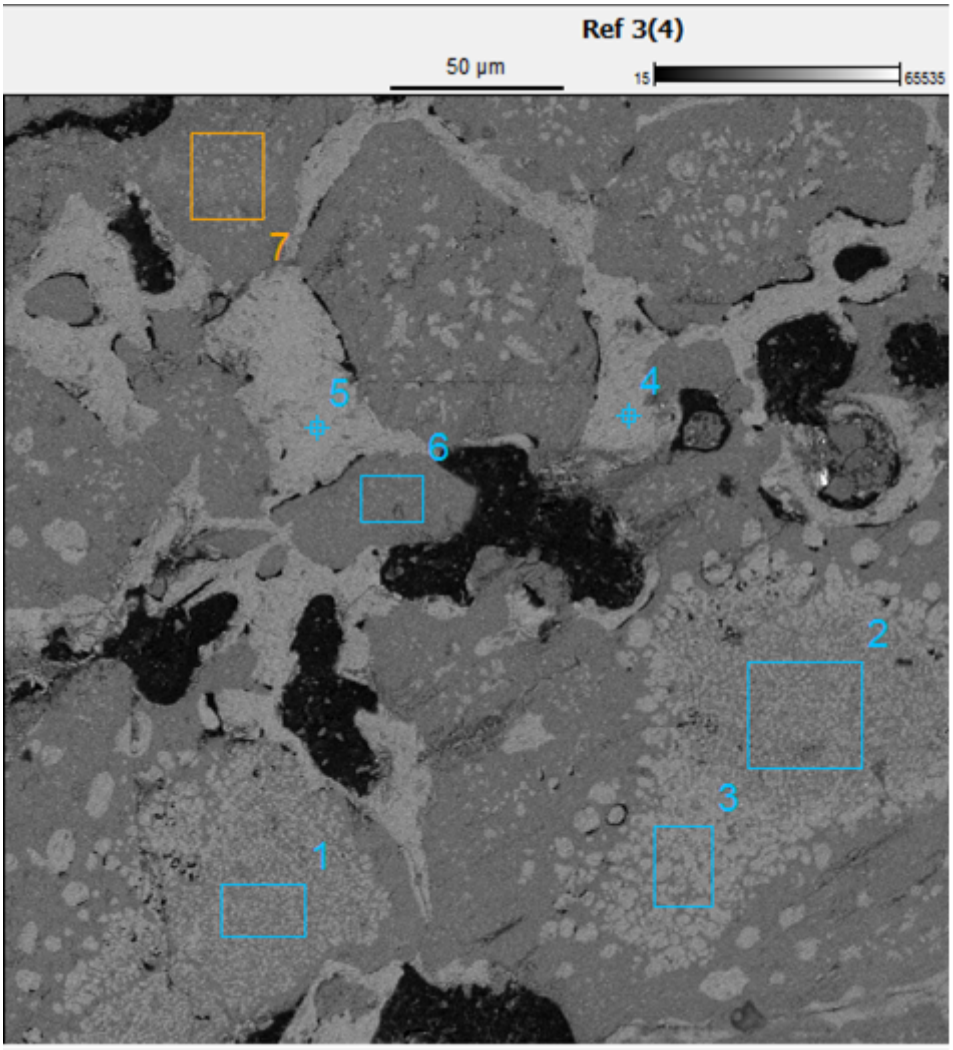

Figure 48: Analysed areas in section 4 on the Radex OX6 refractory.

Table 17: Measured composition values in area 1 from section 4 on the Radex OX6 refractory

Element Line	Element Wt.%	Norm. Wt.%	Atom %
O K	23,98	27,5	42,13
F K	0	0	0
Na K	0,19	0,22	0,23
Mg K	35,1	40,25	40,6
Al K	4,25	4,88	4,43
Si K	0,02	0,03	0,02
Cl K	0,01	0,01	0,01
K K	0,5	0,57	0,36
Ca K	0,3	0,34	0,21
Cr K	13,53	15,52	7,32
Fe K	9,31	10,68	4,69
Total	87,2	100	100

Table 18: Measured composition values in area 2 from section 4 on the Radex OX6 refractory

Element Line	Element Wt.%	Norm. Wt.%	Atom %
O K	28,61	30,22	45,14
F K	0	0	0
Na K	0,66	0,7	0,72
Mg K	37,44	39,54	38,89
Al K	4,21	4,45	3,94
Si K	0,03	0,03	0,03
Cl K	0,02	0,02	0,01
K K	0,25	0,27	0,16
Ca K	0,22	0,24	0,14
Cr K	13,74	14,51	6,67
Fe K	9,49	10,03	4,29
Total	94,67	100	100

Table 19: Measured composition values in area 3 from section 4 on the Radex OX6 refractory

Element Line	Element Wt.%	Norm. Wt.%	Atom %
O K	26,38	29,14	45,5
F K	0	0	0
Na K	0,15	0,17	0,18
Mg K	28,95	31,99	32,88
Al K	6,11	6,76	6,25
Si K	0,02	0,02	0,02
Cl K	0,02	0,02	0,01
K K	0,39	0,43	0,28
Ca K	0,27	0,3	0,19
Cr K	20,51	22,66	10,89
Fe K	7,7	8,51	3,81
Total	90,5	100	100

Table 20: Measured composition values in area 4 from section 4 on the Radex OX6 refractory

Element Line	Element Wt.%	Norm. Wt.%	Atom %
O K	24,04	28,14	45,75
F K	0	0	0
Na K	0,13	0,16	0,18
Mg K	20,44	23,92	25,61
Al K	8,51	9,97	9,61
Si K	0,12	0,15	0,13
Cl K	0	0	0
K K	0,26	0,31	0,21
Ca K	0,2	0,23	0,15
Cr K	26,54	31,07	15,54
Fe K	5,18	6,06	2,82
Total	85,44	100	100

Table 21: Measured composition values in area 5 from section 4 on the Radex OX6 refractory

Element Line	Element Wt.%	Norm. Wt.%	Atom %
O K	21,91	25,98	43,43
F K	0	0	0
Na K	0,3	0,36	0,42
Mg K	19,19	22,76	25,05
Al K	8,94	10,6	10,51
Si K	0,14	0,16	0,15
Cl K	0	0	0
K K	0,35	0,41	0,28
Ca K	0,22	0,26	0,17
Cr K	25,89	30,71	15,8
Fe K	7,38	8,75	4,19
Total	84,32	100	100

Table 22: Measured composition values in area 6 from section 4 on the Radex OX6 refractory

Element Line	Element Wt.%	Norm. Wt.%	Atom %
O K	27,44	29,98	42,91
F K	0	0	0
Na K	0,89	0,97	0,97
Mg K	46,66	50,97	48,03
Al K	0,7	0,76	0,65
Si K	0,04	0,04	0,03
Cl K	0	0	0
K K	0,47	0,51	0,3
Ca K	0,61	0,67	0,38
Cr K	3,67	4,01	1,77
Fe K	11,06	12,08	4,95
Total	91,55	100	100

Table 23: Measured composition values in area 7 from section 4 on the Radex OX6 refractory

Element Line	Element Wt.%	Norm. Wt.%	Atom %
O K	23,32	27,77	41,27
F K	0	0	0
Na K	0,67	0,8	0,83
Mg K	36,18	43,1	42,16
Al K	4,26	5,07	4,47
Si K	0,04	0,05	0,04
Cl K	0	0	0
K K	5	5,96	3,62
Ca K	0,52	0,62	0,37
Cr K	4,87	5,8	2,65
Fe K	8,98	10,69	4,55
Mo L*	0,12	0,14	0,04
Total	83,96	100	100

* Standard Unavailable

B Selected analysis points from Resistal RK30

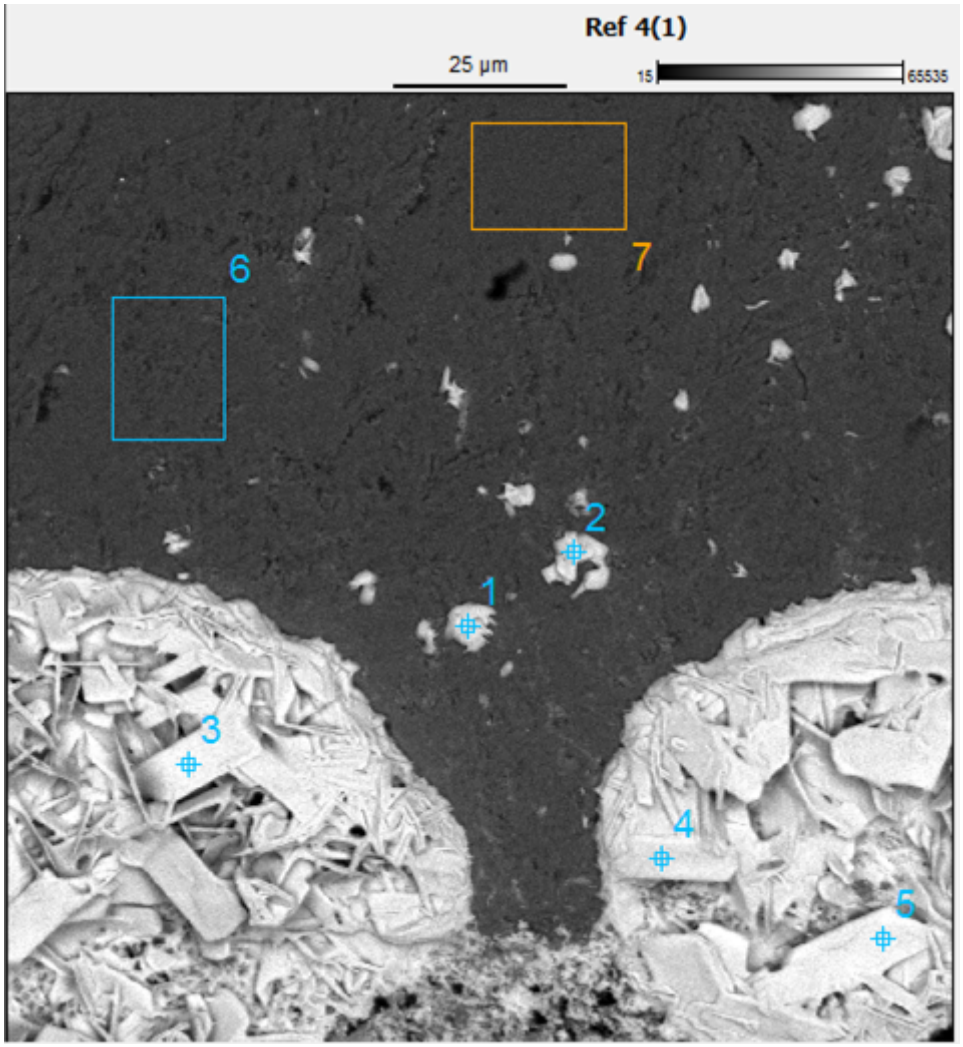

Figure 49: Analysed areas in section 1 on the Resistal RK30 refractory.

Table 24: Measured composition values in area 1 from section 1 on the Resistal RK30 refractory

Element Line	Element Wt.%	Norm. Wt.%	Atom %
O K	22,13	23,89	51,3
F K	0	0	0
Na K	0,96	1,04	1,55
Mg K	0,1	0,1	0,15
Al K	5,8	6,26	7,98
Si K	0,25	0,27	0,33
Cl K	0,26	0,28	0,27
K K	22,97	24,79	21,79
Ca K	2,03	2,19	1,88
Cr K	0	0	0
Fe K	0,03	0,03	0,02
Mo L*	38,11	41,14	14,73
Total	92,64	100	100

* Standard Unavailable

Table 25: Measured composition values in area 2 from section 1 on the Resistal RK30 refractory

Element Line	Element Wt.%	Norm. Wt.%	Atom %
O K	31,9	27,74	58,35
F K	0	0	0
Na K	1,06	0,92	1,34
Mg K	0,04	0,04	0,05
Al K	0,95	0,83	1,03
Si K	0	0	0
Cl K	0,32	0,27	0,26
K K	30,45	26,47	22,79
Ca K	1,86	1,62	1,36
Cr K	0,04	0,03	0,02
Fe K	0,17	0,14	0,09
Mo L*	48,23	41,93	14,71
Total	115,02	100	100

* Standard Unavailable

Table 26: Measured composition values in area 3 from section 1 on the Resistal RK30 refractory

Element Line	Element Wt.%	Norm. Wt.%	Atom %
O K	28,6	26,09	57,4
F K	0	0	0
Na K	0,29	0,26	0,4
Mg K	0,01	0,01	0,02
Al K	0,13	0,12	0,15
Si K	0	0	0
Cl K	0,3	0,27	0,27
K K	28,97	26,43	23,79
Ca K	1,7	1,55	1,36
Cr K	0	0	0
Fe K	0	0	0
Mo L*	49,63	45,27	16,61
Total	109,62	100	100

* Standard Unavailable

Table 27: Measured composition values in area 4 from section 1 on the Resistal RK30 refractory

Element Line	Element Wt.%	Norm. Wt.%	Atom %
O K	37,64	29,85	61,05
F K	0	0	0
Na K	0,32	0,25	0,36
Mg K	0,02	0,01	0,02
Al K	0,17	0,14	0,17
Si K	0	0	0
Cl K	0,49	0,39	0,36
K K	34,78	27,59	23,08
Ca K	1,91	1,52	1,24
Cr K	0	0	0
Fe K	0	0	0
Mo L*	50,74	40,25	13,73
Total	126,07	100	100

* Standard Unavailable

Table 28: Measured composition values in area 5 from section 1 on the Resistal RK30 refractory

Element Line	Element Wt.%	Norm. Wt.%	Atom %
O K	27,75	25,68	56,55
F K	0	0	0
Na K	0,26	0,24	0,37
Mg K	0,02	0,02	0,03
Al K	0,14	0,13	0,17
Si K	0	0	0
Cl K	0,31	0,29	0,29
K K	29,82	27,59	24,87
Ca K	1,7	1,57	1,38
Cr K	0	0	0
Fe K	0,04	0,04	0,03
Mo L*	48,02	44,43	16,32
Total	108,08	100	100

* Standard Unavailable

Table 29: Measured composition values in area 6 from section 1 on the Resistal RK30 refractory

Element Line	Element Wt.%	Norm. Wt.%	Atom %
O K	37,18	38,85	53,1
F K	0	0	0
Na K	0,18	0,19	0,18
Mg K	0,3	0,31	0,28
Al K	48,04	50,2	40,68
Si K	0,19	0,2	0,16
Cl K	0	0	0
K K	9,38	9,8	5,48
Ca K	0,01	0,01	0
Cr K	0,07	0,07	0,03
Fe K	0,01	0,01	0
Mo L*	0,34	0,36	0,08
Total	95,7	100	100

* Standard Unavailable

Table 30: Measured composition values in area 7 from section 1 on the Resistal RK30 refractory

Element Line	Element Wt.%	Norm. Wt.%	Atom %
O K	38,08	39,17	53,22
F K	0	0	0
Na K	0,17	0,17	0,16
Mg K	0,31	0,32	0,28
Al K	49,68	51,09	41,17
Si K	0,14	0,15	0,11
Cl K	0	0	0
K K	8,33	8,56	4,76
Ca K	0,52	0,53	0,29
Cr K	0,01	0,01	0
Fe K	0	0	0
Total	97,23	100	100

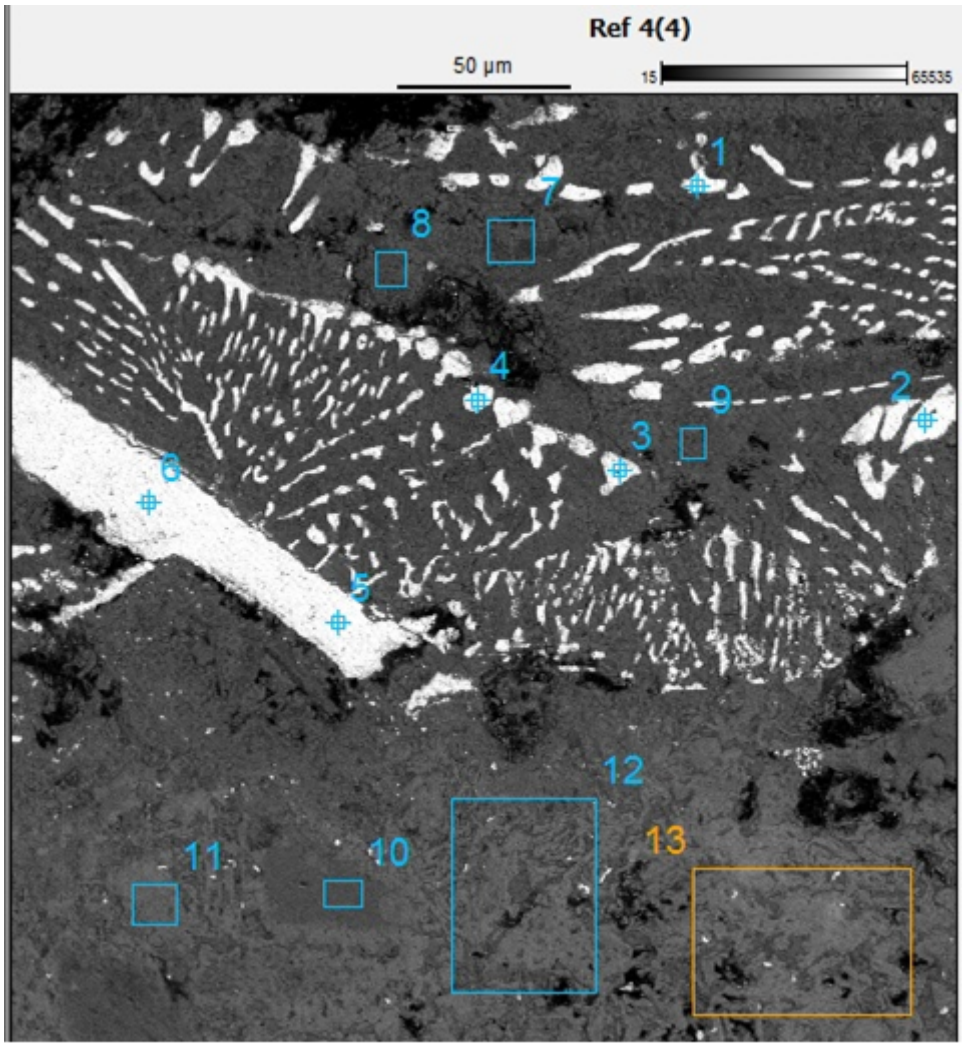

Figure 50: Analysed areas in section 4 on the Resistal RK30 refractory.

Table 31: Measured composition values in area 1 from section 4 on the Resistal RK30 refractory

Element Line	Element Wt.%	Norm. Wt.%	Atom %
O K	27,1	26,85	67,58
F K	0	0	0
Na K	0	0	0
Mg K	0,04	0,04	0,06
Al K	0	0	0
Si K	0	0	0
Cl K	0,03	0,03	0,03
K K	0,09	0,09	0,09
Ca K	0	0	0
Cr K	0,02	0,02	0,01
Zr L*	73,66	72,98	32,22
Total	100,94	100	100

* Standard Unavailable

Table 32: Measured composition values in area 2 from section 4 on the Resistal RK30 refractory

Element Line	Element Wt.%	Norm. Wt.%	Atom %
O K	24,41	24,94	65,38
F K	0	0	0
Na K	0,03	0,03	0,06
Mg K	0	0	0
Al K	0	0	0
Si K	0	0	0
Cl K	0	0	0
K K	0,03	0,03	0,03
Ca K	0	0	0
Cr K	0,11	0,11	0,09
Zr L*	73,28	74,88	34,43
Total	97,87	100	100

* Standard Unavailable

Table 33: Measured composition values in area 3 from section 4 on the resistal RK30 refractory

Element Line	Element Wt.%	Norm. Wt.%	Atom %
O K	23,98	25,87	66,47
F K	0	0	0
Na K	0	0	0
Mg K	0	0	0
Al K	0	0	0
Si K	0	0	0
Cl K	0,03	0,03	0,04
K K	0,13	0,14	0,15
Ca K	0	0	0
Cr K	0,06	0,06	0,05
Zr L*	68,48	73,89	33,29
Total	92,68	100	100

* Standard Unavailable

Table 34: Measured composition values in area 4 from section 4 on the Resistal RK30 refractory

Element Line	Element Wt.%	Norm. Wt.%	Atom %
O K	23,5	24,93	65,34
F K	0	0	0
Na K	0,04	0,04	0,08
Mg K	0	0	0
Al K	0	0	0
Si K	0	0	0
Cl K	0,01	0,01	0,01
K K	0,14	0,15	0,16
Ca K	0	0	0
Cr K	0,02	0,02	0,01
Zr L*	70,54	74,85	34,4
Total	94,24	100	100

* Standard Unavailable

Table 35: Measured composition values in area 5 from section 4 on the Resistal RK30 refractory

Element Line	Element Wt.%	Norm. Wt.%	Atom %
O K	19,12	21,5	60,88
F K	0	0	0
Na K	0,03	0,04	0,08
Mg K	0,04	0,05	0,09
Al K	0	0	0
Si K	0	0	0
Cl K	0	0	0
K K	0	0	0
Ca K	0	0	0
Cr K	0	0	0
Zr L*	69,72	78,41	38,94
Total	88,92	100	100

* Standard Unavailable

Table 36: Measured composition values in area 6 from section 4 on the Resistal RK30 refractory

Element Line	Element Wt.%	Norm. Wt.%	Atom %
O K	26,6	27,09	67,86
F K	0	0	0
Na K	0,04	0,04	0,08
Mg K	0	0	0
Al K	0	0	0
Si K	0	0	0
Cl K	0,03	0,03	0,04
K K	0,01	0,01	0,02
Ca K	0	0	0
Cr K	0,03	0,03	0,03
Zr L*	71,47	72,78	31,98
Total	98,19	100	100

* Standard Unavailable

Table 37: Measured composition values in area 7 from section 4 on the Resistal RK30 refractory

Element Line	Element Wt.%	Norm. Wt.%	Atom %
O K	38,73	41,22	56,69
F K	0	0	0
Na K	0,18	0,19	0,19
Mg K	0,1	0,11	0,1
Al K	27,75	29,53	24,08
Si K	11,4	12,14	9,51
Cl K	0,04	0,05	0,03
K K	14,68	15,63	8,79
Ca K	0,96	1,02	0,56
Cr K	0,11	0,12	0,05
Total	93,97	100	100

Table 38: Measured composition values in area 8 from section 4 on the Resistal RK30 refractory

Element Line	Element Wt.%	Norm. Wt.%	Atom %
O K	38,92	41,36	57,11
F K	0	0	0
Na K	0,05	0,06	0,06
Mg K	0,03	0,03	0,03
Al K	26,09	27,73	22,7
Si K	11,59	12,32	9,69
Cl K	0	0	0
K K	16,15	17,17	9,7
Ca K	1,1	1,16	0,64
Cr K	0,15	0,16	0,07
Total	94,08	100	100

Table 39: Measured composition values in area 9 from section 4 on the Resistal RK30 refractory

Element Line	Element Wt.%	Norm. Wt.%	Atom %
O K	33,96	36,83	52,5
F K	0	0	0
Na K	0,22	0,24	0,23
Mg K	0,79	0,86	0,8
Al K	29,47	31,96	27,02
Si K	8,78	9,52	7,73
Cl K	0	0	0
K K	16,14	17,51	10,21
Ca K	1,04	1,13	0,64
Cr K	1,8	1,95	0,86
Total	92,2	100	100

Table 40: Measured composition values in area 10 from section 4 on the Resistal RK30 refractory

Element Line	Element Wt.%	Norm. Wt.%	Atom %
O K	33,22	36,31	52,73
F K	0	0	0
Na K	0	0	0
Mg K	0,21	0,23	0,22
Al K	41,18	45	38,75
Si K	0,11	0,12	0,1
Cl K	0	0	0
K K	0,05	0,06	0,03
Ca K	0,01	0,01	0,01
Cr K	16,71	18,26	8,16
Total	91,5	100	100

Table 41: Measured composition values in area 11 from section 4 on the Resistal RK30 refractory

Element Line	Element Wt.%	Norm. Wt.%	Atom %
O K	28,16	32,48	51,69
F K	0	0	0
Na K	0	0	0
Mg K	0,26	0,3	0,32
Al K	28,46	32,82	30,97
Si K	0,23	0,27	0,24
Cl K	0,01	0,01	0,01
K K	0,32	0,37	0,24
Ca K	0,03	0,03	0,02
Cr K	29,24	33,72	16,51
Total	86,71	100	100

Table 42: Measured composition values in area 12 from section 4 on the Resistal RK30 refractory

Element Line	Element Wt.%	Norm. Wt.%	Atom %
O K	27,71	32,88	51,91
F K	0	0	0
Na K	0	0	0
Mg K	0,35	0,42	0,43
Al K	21,67	25,71	24,07
Si K	4,76	5,65	5,08
Cl K	0,03	0,04	0,03
K K	6,44	7,64	4,94
Ca K	0,62	0,73	0,46
Cr K	22,7	26,93	13,08
Total	84,29	100	100

Table 43: Measured composition values in area 13 from section 4 on the Resistal RK30 refractory

Element Line	Element Wt.%	Norm. Wt.%	Atom %
O K	27,4	32,83	52,97
F K	0	0	0
Na K	0	0	0
Mg K	0,27	0,32	0,34
Al K	19,18	22,98	21,99
Si K	3,8	4,55	4,19
Cl K	0	0	0
K K	5,1	6,11	4,04
Ca K	0	0	0
Cr K	27,7	33,19	16,48
Total	83,46	100	100

C Selected analysis points from Radex S

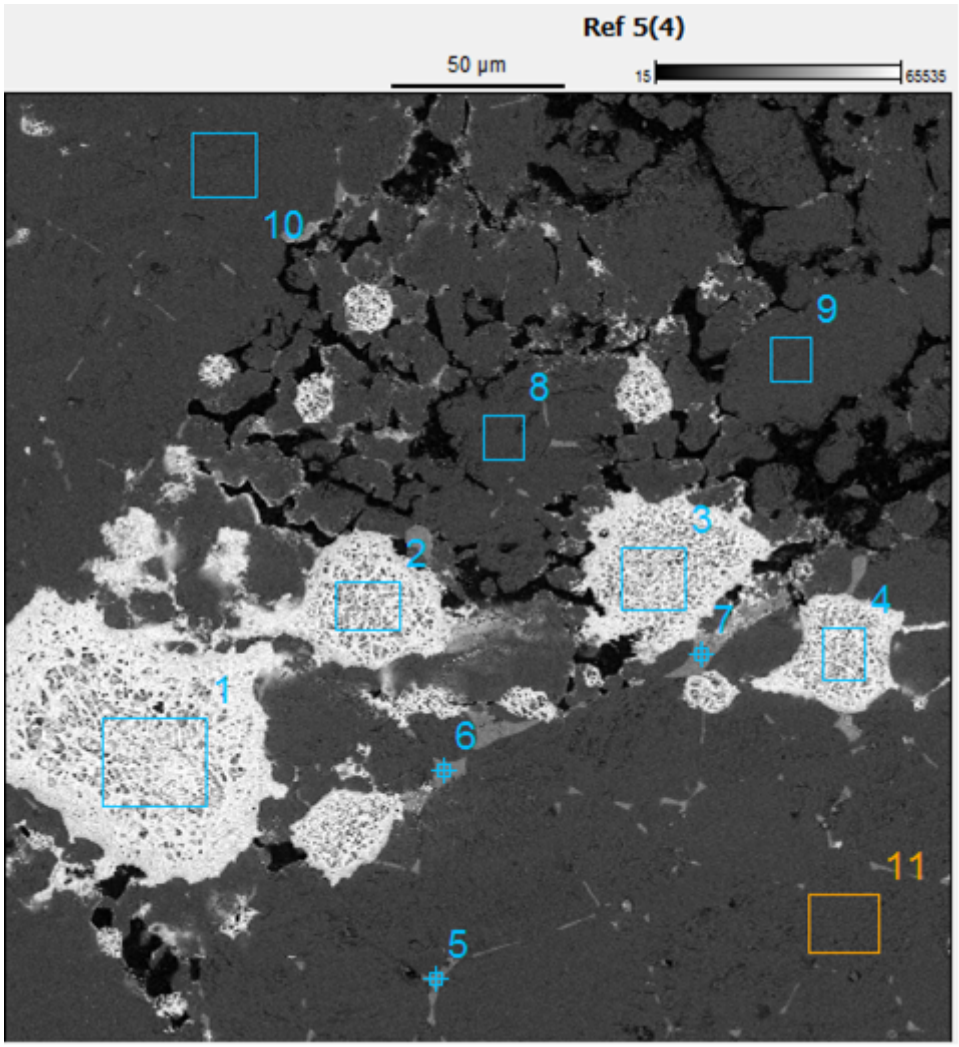

Figure 51: Analysed areas in section 3 on the Radex S refractory.

Table 44: Measured composition values in area 1 from section 3 on the Radex S refractory

Element Line	Element Wt.%	Norm. Wt.%	Atom %
O K	26,19	25,53	56,28
F K	0,13	0,13	0,24
Na K	0,1	0,09	0,15
Mg K	0,22	0,22	0,32
Al K	0,08	0,08	0,1
Si K	0	0	0
Cl K	0,26	0,25	0,25
K K	28,27	27,55	24,85
Ca K	1,65	1,61	1,42
Cr K	0,04	0,04	0,02
Mo L*	45,67	44,51	16,37
Total	102,61	100	100

* Standard Unavailable

Table 45: Measured composition values in area 2 from section 3 on the Radex S refractory

Element Line	Element Wt.%	Norm. Wt.%	Atom %
O K	24,47	24,58	54,87
F K	0,08	0,08	0,16
Na K	0,06	0,06	0,1
Mg K	0,78	0,79	1,16
Al K	0,09	0,09	0,12
Si K	0,01	0,01	0,02
Cl K	0,27	0,28	0,28
K K	27,26	27,4	25,02
Ca K	1,7	1,71	1,53
Cr K	0	0	0
Mo L*	44,77	44,99	16,75
Total	99,52	100	100

* Standard Unavailable

Table 46: Measured composition values in area 3 from section 3 on the Radex S refractory

Element Line	Element Wt.%	Norm. Wt.%	Atom %
O K	27,44	27,12	57,47
F K	0	0	0
Na K	0,08	0,08	0,11
Mg K	1,75	1,73	2,42
Al K	0,09	0,09	0,11
Si K	0,1	0,1	0,12
Cl K	0,35	0,34	0,33
K K	26,82	26,5	22,99
Ca K	1,78	1,76	1,49
Cr K	0,03	0,03	0,02
Mo L*	42,75	42,24	14,93
Total	101,2	100	100

* Standard Unavailable

Table 47: Measured composition values in area 4 from section 3 on the Radex S refractory

Element Line	Element Wt.%	Norm. Wt.%	Atom %
O K	28,14	26,31	56,67
F K	0,1	0,09	0,17
Na K	0,06	0,06	0,09
Mg K	1,54	1,44	2,05
Al K	0,06	0,06	0,08
Si K	0	0	0
Cl K	0,3	0,28	0,27
K K	28,9	27,02	23,82
Ca K	1,68	1,57	1,35
Cr K	0,04	0,04	0,02
Mo L*	46,13	43,13	15,49
Total	106,95	100	100

* Standard Unavailable

Table 48: Measured composition values in area 5 from section 3 on the Radex S refractory

Element Line	Element Wt.%	Norm. Wt.%	Atom %
O K	21,12	25,01	43,3
F K	0	0	0
Na K	0,01	0,01	0,01
Mg K	0,87	1,03	1,18
Al K	0,12	0,14	0,14
Si K	14,72	17,44	17,2
Cl K	0	0	0
K K	0,45	0,53	0,38
Ca K	45,48	53,87	37,23
Cr K	0,02	0,02	0,01
Mo L*	1,64	1,95	0,56
Total	84,43	100	100

* Standard Unavailable

Table 49: Measured composition values in area 6 from section 3 on the Radex S refractory

Element Line	Element Wt.%	Norm. Wt.%	Atom %
O K	35,72	35,95	55,91
F K	0	0	0
Na K	0,03	0,03	0,03
Mg K	0,26	0,26	0,27
Al K	0,1	0,1	0,09
Si K	15,65	15,75	13,95
Cl K	0	0	0
K K	0,01	0,01	0,01
Ca K	47,54	47,85	29,71
Cr K	0,05	0,05	0,02
Total	99,36	100	100

Table 50: Measured composition values in area 7 from section 3 on the Radex S refractory

Element Line	Element Wt.%	Norm. Wt.%	Atom %
O K	34,64	35,13	55,01
F K	0	0	0
Na K	0,04	0,04	0,04
Mg K	0,42	0,43	0,44
Al K	0,08	0,08	0,07
Si K	15,54	15,76	14,06
Cl K	0	0	0
K K	0,19	0,19	0,12
Ca K	47,71	48,38	30,25
Cr K	0	0	0
Total	98,62	100	100

Table 51: Measured composition values in area 8 from section 3 on the Radex S refractory

Element Line	Element Wt.%	Norm. Wt.%	Atom %
O K	26,55	31,4	41,06
F K	0	0	0
Na K	0,57	0,68	0,62
Mg K	56,99	67,39	58
Al K	0,13	0,15	0,12
Si K	0,05	0,06	0,04
Cl K	0	0	0
K K	0,01	0,01	0,01
Ca K	0,25	0,29	0,15
Cr K	0,02	0,02	0,01
Total	84,56	100	100

Table 52: Measured composition values in area 9 from section 3 on the Radex S refractory

Element Line	Element Wt.%	Norm. Wt.%	Atom %
O K	29,28	32,42	42,23
F K	0	0	0
Na K	0,54	0,6	0,54
Mg K	59,8	66,22	56,77
Al K	0,16	0,17	0,13
Si K	0,07	0,08	0,06
Cl K	0,02	0,02	0,01
K K	0	0	0
Ca K	0,4	0,44	0,23
Cr K	0,04	0,05	0,02
Total	90,3	100	100

Table 53: Measured composition values in area 10 from section 3 on the Radex S refractory

Element Line	Element Wt.%	Norm. Wt.%	Atom %
O K	27,03	31,61	41,31
F K	0	0	0
Na K	0,53	0,63	0,57
Mg K	57,34	67,06	57,69
Al K	0,14	0,17	0,13
Si K	0,05	0,06	0,04
Cl K	0,01	0,01	0
K K	0	0	0
Ca K	0,4	0,47	0,25
Cr K	0,01	0,01	0
Total	85,51	100	100

Table 54: Measured composition values in area 11 from section 3 on the Radex S refractory

Element Line	Element Wt.%	Norm. Wt.%	Atom %
O K	29,06	32,03	41,77
F K	0	0	0
Na K	0,58	0,64	0,58
Mg K	60,54	66,74	57,29
Al K	0,15	0,17	0,13
Si K	0,06	0,07	0,05
Cl K	0	0	0
K K	0,01	0,01	0,01
Ca K	0,3	0,33	0,17
Cr K	0	0	0
Total	90,7	100	100

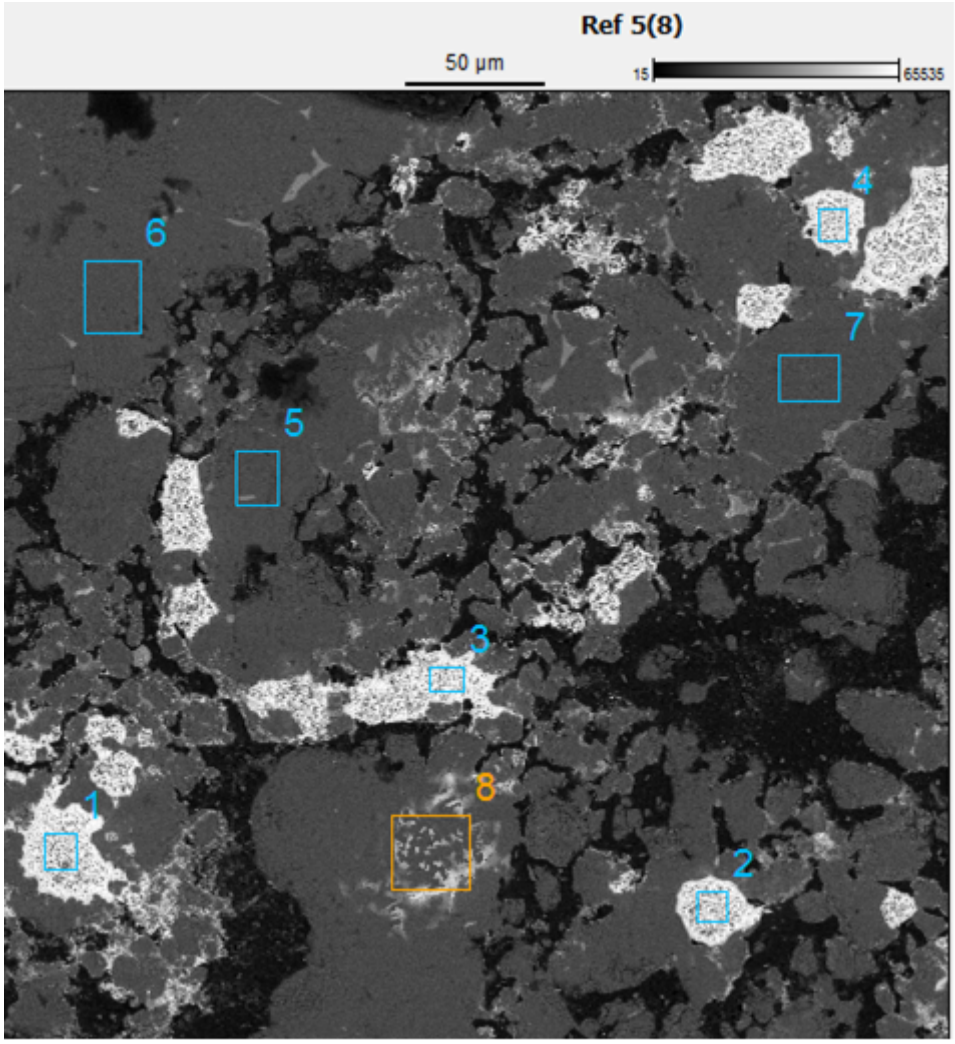

Figure 52: Analysed areas in section 7 on the Radex S refractory.

Table 55: Measured composition values in area 1 from section 7 on the Radex S refractory

Element Line	Element Wt.%	Norm. Wt.%	Atom %
O K	27,28	27,75	56,11
F K	0,24	0,24	0,42
Na K	0,1	0,1	0,14
Mg K	5,73	5,82	7,75
Al K	0,14	0,14	0,17
Si K	0,11	0,11	0,13
Cl K	0,25	0,25	0,23
K K	24,1	24,51	20,28
Ca K	1,92	1,95	1,58
Cr K	0	0	0
Mo L*	38,46	39,11	13,19
Total	98,33	100	100

* Standard Unavailable

Table 56: Measured composition values in area 2 from section 7 on the Radex S refractory

Element Line	Element Wt.%	Norm. Wt.%	Atom %
O K	24,14	24,05	52,59
F K	0	0	0
Na K	0,07	0,07	0,11
Mg K	3,9	3,88	5,59
Al K	0,14	0,14	0,18
Si K	0	0	0
Cl K	0,28	0,28	0,27
K K	27,17	27,07	24,22
Ca K	1,56	1,56	1,36
Cr K	0	0	0
Mo L*	43,13	42,96	15,67
Total	100,4	100	100

* Standard Unavailable

Table 57: Measured composition values in area 3 from section 7 on the Radex S refractory

Element Line	Element Wt.%	Norm. Wt.%	Atom %
O K	28,06	27,37	57,19
F K	0,06	0,06	0,1
Na K	0,09	0,09	0,12
Mg K	2,57	2,51	3,45
Al K	0,27	0,26	0,33
Si K	0,08	0,08	0,09
Cl K	0,25	0,25	0,23
K K	27,41	26,74	22,86
Ca K	1,6	1,56	1,3
Cr K	0	0	0
Mo L*	42,13	41,09	14,32
Total	102,52	100	100

* Standard Unavailable

Table 58: Measured composition values in area 4 from section 7 on the Radex S refractory

Element Line	Element Wt.%	Norm. Wt.%	Atom %
O K	29	26,58	57,38
F K	0,25	0,23	0,42
Na K	0,11	0,1	0,15
Mg K	0,6	0,55	0,78
Al K	0,2	0,18	0,24
Si K	0	0	0
Cl K	0,3	0,27	0,27
K K	29,24	26,79	23,67
Ca K	1,73	1,59	1,37
Cr K	0	0	0
Mo L*	47,69	43,7	15,73
Total	109,12	100	100

* Standard Unavailable

Table 59: Measured composition values in area 5 from section 7 on the Radex S refractory

Element Line	Element Wt.%	Norm. Wt.%	Atom %
O K	28,83	32,53	42,52
F K	0	0	0
Na K	0,54	0,61	0,56
Mg K	57,52	64,91	55,85
Al K	0,19	0,21	0,16
Si K	0,04	0,05	0,04
Cl K	0	0	0
K K	0	0	0
Ca K	1,45	1,64	0,86
Cr K	0,04	0,05	0,02
Total	88,62	100	100

Table 60: Measured composition values in area 6 from section 7 on the Radex S refractory

Element Line	Element Wt.%	Norm. Wt.%	Atom %
O K	28,58	32,58	42,39
F K	0	0	0
Na K	0,55	0,63	0,57
Mg K	58	66,12	56,62
Al K	0,18	0,21	0,16
Si K	0,08	0,09	0,06
Cl K	0	0	0
K K	0	0	0
Ca K	0,32	0,37	0,19
Cr K	0	0	0
Total	87,71	100	100

Table 61: Measured composition values in area 7 from section 7 on the Radex S refractory

Element Line	Element Wt.%	Norm. Wt.%	Atom %
O K	26,8	30,63	40,22
F K	0	0	0
Na K	0,59	0,67	0,61
Mg K	59,41	67,9	58,69
Al K	0,19	0,22	0,17
Si K	0,05	0,06	0,04
Cl K	0	0	0
K K	0	0	0
Ca K	0,4	0,45	0,24
Cr K	0,06	0,07	0,03
Total	87,5	100	100

Table 62: Measured composition values in area 8 from section 7 on the Radex S refractory

Element Line	Element Wt.%	Norm. Wt.%	Atom %
O K	28,17	32,69	44,14
F K	0	0	0
Na K	0,56	0,65	0,61
Mg K	49,79	57,78	51,36
Al K	0,18	0,21	0,16
Si K	0,06	0,08	0,06
Cl K	0,05	0,06	0,04
K K	3,86	4,48	2,47
Ca K	0,62	0,72	0,39
Cr K	0,05	0,06	0,03
Mo L*	2,82	3,27	0,74
Total	86,17	100	100

* Standard Unavailable

D Selected analysis points from Durital E90

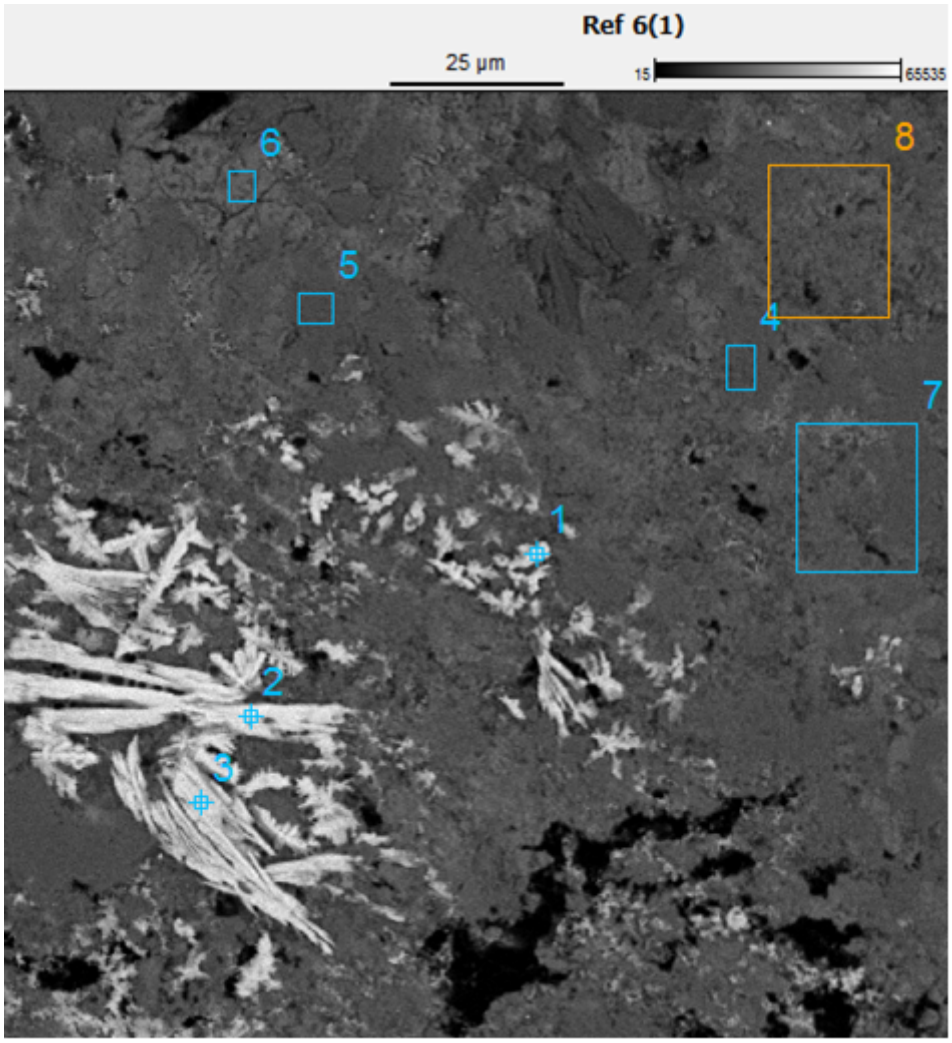

Figure 53: Analysed areas in section 1 on the Durital E90 refractory.

Table 63: Measured composition values in area 1 from section 1 on the Durital E90 refractory

Element Line	Element Wt.%	Norm. Wt.%	Atom %
O K	32,15	29,59	59,29
F K	0	0	0
Na K	1,68	1,54	2,15
Mg K	0,02	0,02	0,03
Al K	2,22	2,05	2,43
Si K	1,57	1,45	1,65
Cl K	0,31	0,28	0,26
K K	26,35	24,25	19,89
Ca K	1,54	1,42	1,13
Cr K	0	0	0
Mo L*	42,81	39,4	13,17
Total	108,66	100	100

* Standard Unavailable

Table 64: Measured composition values in area 2 from section 1 on the Durital E90 refractory

Element Line	Element Wt.%	Norm. Wt.%	Atom %
O K	30,17	28,39	57,74
F K	0	0	0
Na K	0,27	0,25	0,36
Mg K	0,04	0,04	0,06
Al K	4,9	4,61	5,56
Si K	0,78	0,73	0,85
Cl K	0,34	0,32	0,29
K K	26,34	24,78	20,63
Ca K	1,45	1,36	1,11
Cr K	0	0	0
Mo L*	41,99	39,51	13,4
Total	106,28	100	100

* Standard Unavailable

Table 65: Measured composition values in area 3 from section 1 on the Durital E90 refractory

Element Line	Element Wt.%	Norm. Wt.%	Atom %
O K	22,8	26,42	53,53
F K	0	0	0
Na K	0,29	0,33	0,47
Mg K	0,05	0,06	0,08
Al K	6,19	7,17	8,61
Si K	2,06	2,39	2,76
Cl K	0	0	0
K K	21,72	25,17	20,87
Ca K	1,27	1,47	1,19
Cr K	0	0	0
Mo L*	31,93	36,99	12,5
Total	86,31	100	100

* Standard Unavailable

Table 66: Measured composition values in area 4 from section 1 on the Durital E90 refractory

Element Line	Element Wt.%	Norm. Wt.%	Atom %
O K	37,97	38,5	52,84
F K	0	0	0
Na K	0,18	0,18	0,17
Mg K	0,34	0,34	0,31
Al K	48,85	49,53	40,31
Si K	0,41	0,41	0,32
Cl K	0	0	0
K K	9,83	9,97	5,6
Ca K	0,61	0,61	0,34
Cr K	0,02	0,02	0,01
Mo L*	0,42	0,43	0,1
Total	98,62	100	100

* Standard Unavailable

Table 67: Measured composition values in area 5 from section 1 on the Durital E90 refractory

Element Line	Element Wt.%	Norm. Wt.%	Atom %
O K	37,85	38,52	52,79
F K	0	0	0
Na K	0,15	0,15	0,15
Mg K	0,34	0,35	0,32
Al K	48,92	49,78	40,46
Si K	0,43	0,43	0,34
Cl K	0	0	0
K K	10,33	10,51	5,89
Ca K	0	0	0
Cr K	0,03	0,03	0,01
Mo L*	0,22	0,22	0,05
Total	98,26	100	100

* Standard Unavailable

Table 68: Measured composition values in area 6 from section 1 on the Durital E90 refractory

Element Line	Element Wt.%	Norm. Wt.%	Atom %
O K	39,09	40,58	57,32
F K	0	0	0
Na K	0	0	0
Mg K	0	0	0
Al K	16,84	17,47	14,64
Si K	16,24	16,85	13,56
Cl K	0	0	0
K K	22,73	23,6	13,64
Ca K	1,44	1,5	0,84
Cr K	0	0	0
Total	96,34	100	100

Table 69: Measured composition values in area 7 from section 1 on the Durital E90 refractory

Element Line	Element Wt.%	Norm. Wt.%	Atom %
O K	33,92	38,33	54,56
F K	0	0	0
Na K	0,11	0,12	0,12
Mg K	0,24	0,27	0,25
Al K	32,31	36,51	30,82
Si K	4,95	5,59	4,54
Cl K	0,02	0,02	0,01
K K	12,49	14,11	8,22
Ca K	0,76	0,86	0,49
Cr K	0,03	0,03	0,01
Mo L*	3,67	4,15	0,98
Total	88,5	100	100

* Standard Unavailable

Table 70: Measured composition values in area 8 from section 1 on the Durital E90 refractory

Element Line	Element Wt.%	Norm. Wt.%	Atom %
O K	33,15	38,23	55,07
F K	0	0	0
Na K	0,13	0,15	0,15
Mg K	0,28	0,32	0,31
Al K	28,36	32,7	27,93
Si K	5,61	6,47	5,3
Cl K	0,04	0,04	0,03
K K	13,8	15,91	9,38
Ca K	0,88	1,01	0,58
Cr K	0,07	0,08	0,04
Mo L*	4,41	5,09	1,22
Total	86,71	100	100

* Standard Unavailable

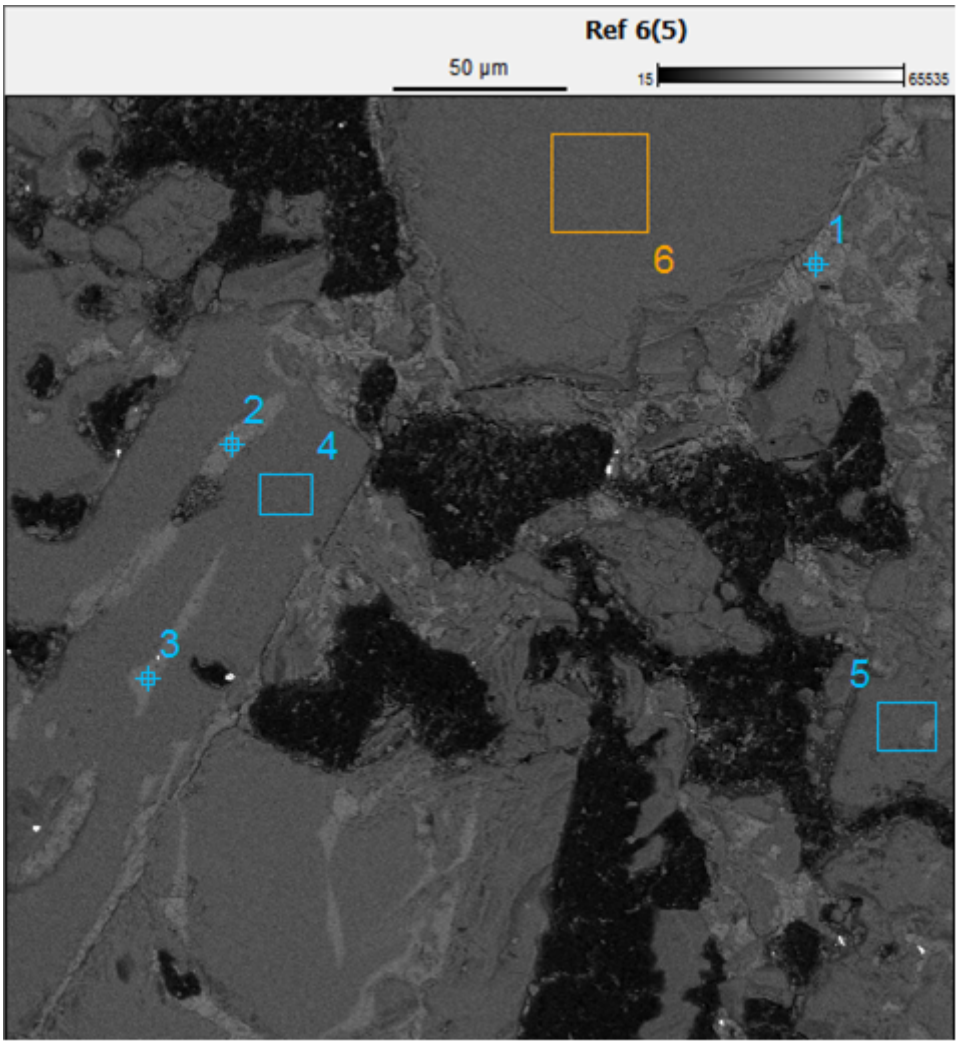

Figure 54: Analysed areas in section 5 on the Durital E90 refractory.

Table 71: Measured composition values in area 1 from section 5 on the Durital E90 refractory

Element Line	Element Wt.%	Norm. Wt.%	Atom %
O K	23,57	30,85	46,55
F K	0,38	0,5	0,64
Na K	0,11	0,15	0,16
Mg K	0,02	0,02	0,02
Al K	13,85	18,13	16,22
Si K	16,88	22,09	18,99
Cl K	0,01	0,02	0,01
K K	20,28	26,55	16,39
Ca K	1,29	1,69	1,02
Cr K	0	0	0
Total	76,4	100	100

Table 72: Measured composition values in area 2 from section 5 on the Durital E90 refractory

Element Line	Element Wt.%	Norm. Wt.%	Atom %
O K	28,32	34,29	49,03
F K	1,4	1,69	2,04
Na K	0,02	0,02	0,02
Mg K	0,28	0,34	0,32
Al K	14,44	17,48	14,82
Si K	24,47	29,62	24,13
Cl K	0	0	0
K K	12,3	14,89	8,71
Ca K	1,28	1,55	0,88
Cr K	0,09	0,1	0,05
Total	82,6	100	100

Table 73: Measured composition values in area 3 from section 5 on the Durital E90 refractory

Element Line	Element Wt.%	Norm. Wt.%	Atom %
O K	30,06	35,71	50,5
F K	1,81	2,15	2,56
Na K	0,18	0,21	0,21
Mg K	0,28	0,33	0,31
Al K	14,21	16,88	14,15
Si K	23,76	28,23	22,74
Cl K	0	0	0
K K	12,63	15	8,68
Ca K	1,24	1,47	0,83
Cr K	0,02	0,02	0,01
Total	84,19	100	100

Table 74: Measured composition values in area 4 from section 5 on the Durital E90 refractory

Element Line	Element Wt.%	Norm. Wt.%	Atom %
O K	38,17	40,81	53,74
F K	0	0	0
Na K	0,17	0,18	0,16
Mg K	0,38	0,41	0,35
Al K	54,66	58,44	45,63
Si K	0,1	0,11	0,08
Cl K	0	0	0
K K	0,02	0,02	0,01
Ca K	0,03	0,03	0,02
Cr K	0	0	0
Total	93,54	100	100

Table 75: Measured composition values in area 5 from section 5 on the Durital E90 refractory

Element Line	Element Wt.%	Norm. Wt.%	Atom %
O K	38,94	40,6	53,83
F K	0	0	0
Na K	0,29	0,3	0,27
Mg K	0,46	0,48	0,42
Al K	50,67	52,83	41,54
Si K	3,61	3,77	2,84
Cl K	0	0	0
K K	1,68	1,75	0,95
Ca K	0,24	0,25	0,13
Cr K	0,03	0,03	0,01
Total	95,91	100	100

Table 76: Measured composition values in area 6 from section 5 on the Durital E90 refractory

Element Line	Element Wt.%	Norm. Wt.%	Atom %
O K	40,72	43,33	56,48
F K	0	0	0
Na K	0,23	0,24	0,22
Mg K	0,31	0,33	0,28
Al K	42,1	44,8	34,63
Si K	10,59	11,27	8,37
Cl K	0	0	0
K K	0,02	0,03	0,01
Ca K	0	0	0
Cr K	0,01	0,01	0
Total	93,98	100	100